FRIEDRICH-SCHILLER-UNIVERSITÄT JENA

Design, Implementation and Application of Nanostructure-enhanced Optical Fibers

Dissertation

zur Erlangung des akademischen Grades
doctor rerum naturalium (Dr. rer. nat.)

vorgelegt dem Rat der Physikalisch-Astronomischen Fakultät
der Friedrich-Schiller-Universität Jena

von M.Eng Ning Wang
geboren am 18.08.1989 in Xintai, China

Gutachter:

1. Prof. Dr. Markus A. SCHMIDT, Friedrich Schiller University of Jena
2. Prof. Dr. Bert HECHT, Julius Maximilian University of Würzburg
3. Jun. Prof. Dr. Isabelle STAUDE, Friedrich Schiller University of Jena

Tag der Disputation: 24.09.2019

FRIEDRICH-SCHILLER-UNIVERSITÄT JENA

Abstract

This thesis covers the research topic of nano-plasmonics as well as fiber optics with a study focus on design and implementation of a functional optical fiber tip by integrating nanoscale resonance structure on its facet. Accordingly, the research background and state-of-the-art are generally discussed at the beginning. Since this work is highly related to two distinct optic areas, the fundamentals of both fields would be given in the following sections.

The subsequent chapters are concerned with design, characterization, and implementation of plasmonic nanostructure on fiber end-faces. In particular, we illustrate the diverse spectral evolution of the closely-packed nanotrimer array, which offers a new degree of freedom to design artificial nanocomponents and -devices. Furthermore, we employ electron beam lithography to fabricate nanostructures on fiber facet by planarizing fibers surface in a specially-designed can-like holder. This technique represents a significant step forward in the research field of fiber functionalization and opens up the field of nanoengineering for fiber optics.

At last, we demonstrate potential applications of nanostructure-enhanced fibers by examples of a high-precision refractive index sensor and a light signal detector. These fiber-substrated prototypes presented here provide one of the first investigations into how to employ nanostructure-modified optical fibers as short-cut tools for a number of important implications of future practice, including but limited to bioanalytics, telecommunications, and quantum technologies.

Overall, the studies contribute in several ways to understand complex optical response of nanostrucutures mediated by the geometrical distribution and provide a new degree to finely tailor plasmonic resonances of nanoantennas. The electron beam lithography-based fabrication approach also establishes a solid framework towards 'lab-on-fiber' enabled by functional nanostructures. We hope this thesis could offer valuable insights into design and prototyping of the nanoplasmonic-inspired optical devices.

Zusammenfassung

Diese Arbeit beschäftigt sich mit dem Forschungsthema Nanoplasmonik sowie Faseroptik mit einem Schwerpunkt auf dem Design und der Implementierung einer funktionalen Glasfaserspitze durch Integration der nanoskaligen Resonanzstruktur auf ihrer Facette. Dementsprechend werden der Forschungshintergrund und der Stand der Technik in der Regel zu Beginn diskutiert. Da diese Arbeit in hohem Maße mit zwei verschiedenen optischen Bereichen zusammenhängt, werden die Grundlagen beider Bereiche in den folgenden Abschnitten erläutert.

Die folgenden Kapitel befassen sich mit dem Design, der Charakterisierung und der Implementierung der plasmonischen Nanostruktur auf Faserenden. Insbesondere veranschaulichen wir die unterschiedliche spektrale Entwicklung des dicht gepackten Nanotrimer-Arrays, das ein neues Maß an Freiheit bei der Entwicklung künstlicher Nanokomponenten und -geräte bietet. Darüber hinaus verwenden wir Elektronenstrahllithographie, um Nanostrukturen auf Faserfacetten herzustellen, indem wir die Faseroberfläche in einem speziell entwickelten, dosenartigen Halter planarisieren. Diese Technik stellt einen bedeutenden Fortschritt auf dem Gebiet der Faserfunktionalisierung dar und eröffnet das Feld des Nanoengineerings für Glasfasern.

Schließlich zeigen wir die Einsatzmöglichkeiten von nanostrukturverstärkten Fasern am Beispiel eines hochpräzisen Brechungsindex-Sensors und eines Lichtsignaldetektors. Diese hier vorgestellten faserverstärkten Prototypen stellen eine der ersten Untersuchungen dar, wie man nanostrukturmodifizierte Glasfasern als Abkürzungswerkzeuge für eine Reihe wichtiger Implikationen der zukünftigen Praxis einsetzen kann, einschließlich, aber nicht beschränkt auf Bioanalytik, Telekommunikation und Quantentechnologien.

Insgesamt tragen die Studien in mehrfacher Hinsicht dazu bei, die komplexe optische Reaktion von Nanostrukturen zu verstehen, die durch die geometrische Verteilung vermittelt wird, und bieten einen neuen Grad, um plasmonische Resonanzen von Nanoantennen zu optimieren. Der auf Elektronenstrahl Lithographie basierende Fertigungsansatz etabliert auch ein solides Grundgerüst in Richtung "Lab-on-Fiber", das durch funktionale Nanostrukturen ermöglicht wird. Wir hoffen, dass diese Arbeit wertvolle Einblicke in das Design und Prototyping der nanoplasmonisch inspirierten optischen Geräte geben kann.

Contents

List of Abbreviations

ALD	Atomic layer deposition
EBL	Electron beam lithography
FEM	Finite element method
FDTD	Finite difference time domain
FIB	Focused ion beam
FWHM	Full width at half maximum
GIF	Graded index fiber
IR	Infrared
LSPR	Localized surface plasmon resonance
MLWA	Modified long wavelength approximation
MMF	Multi mode fiber
NA	Numerical aperture
NIR	Near infrared
OSA	Optical spectrum analyzer
PAMF	Pressure-assisted melt-filling
PCF	Photonic crystal fiber
PDMS	Polydimethylsiloxane
PMMA	Poly(methyl methacrylate)
RI	Refractive index
RIU	Refractive index unit
SEM	Scanning electron microscope
SIF	Step index fiber
SLR	Surface lattice resonance
SMF	Single mode fiber
SNOM	Scanning near field optical microscope
SPP	Surface plasmon polariton
TIR	Total internal reflection
TPIP	Two photon excited photoluminescence
TPL	Two photon induced luminescence
VIS	Visible

List of Symbols

α	Polarizability
β	Propagation constant
ϵ	Relative permittivity
η	Fiber light-coupling efficiency
θ	Incident angle
θ_c	Critical angle
λ	Wavelength
μ	Relative permeability
Λ	Periodical constant
a	Fiber core radius
c	Light speed constant
k	Wavenumber
n	Refractive index
n_{eff}	Effective index
n_{co}	Refractive index of fiber core
n_{cl}	Refractive index of fiber cladding
C_{sca}	Scattering cross-section
C_{abs}	Absorption cross-section
C_{ext}	Extinction cross-section
D	Nanodot diameter
G	Particle edge-to-edge distance (gap)
H	Nanodot height
Q_{sca}	Scattering coefficient
Q_{abs}	Absorption coefficient
Q_{ext}	Extinction coefficient
Q-factor	Resonance factor
R^2	Coefficient of determination
ΔT_c	Transmission contrast
T	Transmission

To my dearest grandpa . . .

Chapter 1

Introduction

1.1 Background and motivation

Owing to its extremely low signal loss [1, 2], optical fiber has revolutionized modern telecommunication technology and industry [3]. The pioneering work of Charles K. Kao won the Noble Prize in Physics in 2009 for "groundbreaking achievements concerning the transmission of light in fibers for optical communication" [4]. Today, optical fiber research still represents a major scientific field [5–7] within the optics/photonics community, with an application range not limited to communications. For example, fibers can also be employed as highly efficient sensor devices [8] or used in broad spectrum lasers [9].

However, the improvement of fiber optical properties relies on the modification of the fiber geometry (e.g., polarization-maintaining fibers obtained by adding stress rods along the core [10]) and/or the use of composite materials (e.g., a high NA fiber with core and cladding composed of high index-contrast materials [11]). The innovations in fabrications of specialty fibers challenge the drawing technology and improper process improvements could induce product problems such as deformations of fiber cross-section and structure collapse [12].

Meanwhile, nanophotonics has been regarded as one of the hottest research fields over the last two decades [13, 14]. Owing to advancements in nanofabrication technology (such as focused ion beam (FIB) and electron beam lithography (EBL)), nanoscale artificial metallic/dielectric structures can manipulate light propagation [15, 16], providing an innovative platform for studying light-matter interactions. Based on surface plasmons, novel concepts such as metasurfaces [15, 17] have been developed for a wide range of applications, including, but not limited to, beam shaping [18], molecular detection [19] and quantum communication [20].

Hence, these functional nanostructures provide an alternative way to control light on demand and inspire novel design approaches to modify fiber properties. Here, we propose and demonstrate the concept of nanostructure-enhanced fibers, in which plasmonic nanostructures are integrated on fiber facets by means of EBL. Placing nanostructures on fibers could relax strict fabrication requirements during fiber drawing process and additionally endow fibers with more functionalities (e.g., signal multiplexing [21]). This concept also serves to meet the urgent demands of precise light delivery and/or collection, which are of particular interest in the field of biophotonics.

A nanostructure-enhanced fiber is schematically depicted in Fig. 1.1 (a). In general, such a fiber consists of two major components, an optical fiber substrate and functional nanostructures. Here, the horizontally oriented cylinder represents an optical fiber, where the light and dark gray denote the fiber core and cladding, respectively. For illustration, we take an array of hexagonally distributed nanodisks (in orange color) as an example of a nanostructure, which is placed on the end face of this fiber. Under laser excitation (indicated by the multicolor arrow), the optical response of the fiber should be modified due to the presence of the nanodisks.

Apparently, there are certain 'incompatibility' problems between a fiber substrate and functional nanostructures. On the one hand, the majority of subwavelength structures are implemented on flat substrates and may thus not best suit fiber facets. On the other hand, even though there is a wide selection of fibers, none of them is probably specially designed as a substrate to support these nanoscale structures. Hence, an essential issue that needs to be discussed beforehand is which component should be altered (either the fiber substrate or nanostructure) to satisfy certain requirements for the other part.

This prerequisite issue (the modification priority) is described in Fig. 1.1 (b). As indicated by the arrow going from the optical fiber (light-blue background) section to the nanophotonics (light-magenta block) part, the first solution is to alter the fiber geometry and optical property to enable the use of nanostructures. Correspondingly, another approach is to develop specially designed subwavelength structures to meet the requirements of fibers (illustrated by the bottom arrow with the label 2).

Within this work, the second approach (designing and modifying nanostructures to fit fibers) is selected considering the disadvantages of designing new fibers, such as the high costs in terms of time and budget throughout the implementation (the fiber development duration can be a couple of years,

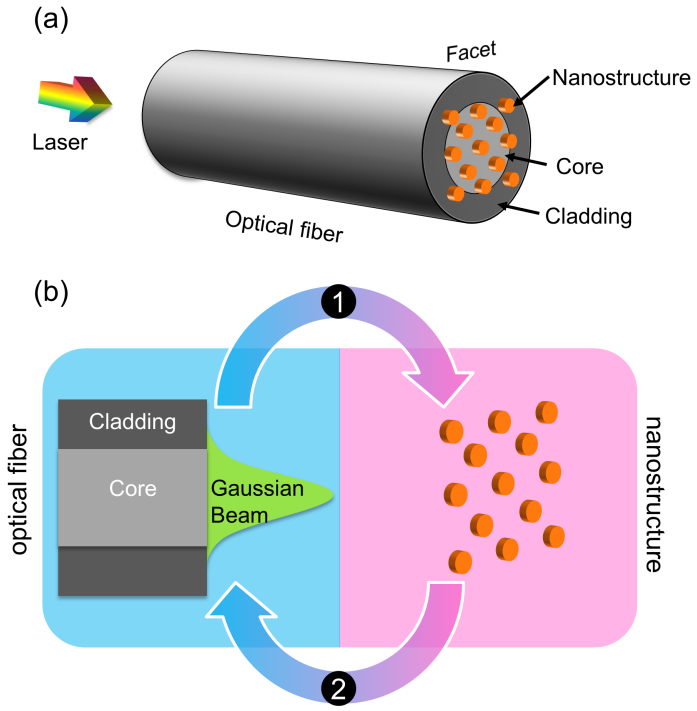

FIGURE 1.1
(a) Schematic showing the concept of nanostructure-enhanced optical fibers. Here, the gray cylinder and orange dots represent an optical fiber and a nanostructure, respectively. (b) Two main research strategies of this work. Label 1 indicates modifying the fiber geometry and optical properties in order to support a nanostructure. Alternatively, a nanostructure can be particularly designed for usage with a fiber (label 2).

and the manufacturing process demands tremendous efforts as well).

Currently, there is a broad range of fibers available in the research field and on the market. Among these fibers, single-mode fiber 28 (SMF-28) [22] is chosen as the substrate based on the following benefits.

- Fiber representative

SMF-28 is the most commonly used fiber in telecommunications. It is commercially available at an extremely low cost ($\ll 1$ €/m).

- Solid fiber facet

SMF-28 consists of a solid silica core and cladding, which can physically support nanostructures. Some microstructured fibers (i.e., hollow core fibers) obviously fail to meet this criterion and thus cannot be used in this project.

- Mode profile

Operating in the IR regime, the fundamental HE_{11} mode of SMF-28 resembles a Gaussian beam profile [2]. Hence, there is no need to adjust the mode excitation.

In summary, the aim of this study is to investigate and design novel plasmonic nanostructures for fiber application, and SMF-28 (Corning Inc. [22]) is selected as the substrate based on the above advantages.

1.2 The state-of-art of this research

We summarize some recently published major achievements in nanostructure-enhanced fibers in Table 1.1 (see page 7) for reference. As seen from this table, a variety of nanostructures (from single monopole [23] to layer-stacked hybrid nanostructure [24]) can be fabricated on different fibers (e.g., SMF-28 [25], photonic crystal fiber (PCF) [26]) via several fabrication schemes (including EBL [27], FIB [28], template transfer [29], etc.). Additionally, these references demonstrate that nanostructure-enhanced fibers benefit multiple fields as a novel platform for chemical and biological sensing [30], beam shaping [28], signal modulations [31], etc.

From the fabrication aspect, Table 1-1 presents two main techniques - FIB and EBL. Some comparative studies [32, 33] have revealed that EBL can produce higher quality nanoantennas (stronger plasmonic response and low contamination) compared to FIB. For fabricating a larger nanoarray pattern, EBL also requires less time than FIB. Hence, we adopt EBL to directly create nanopatterns on fiber facets. In addition, other techniques such as pressure-assisted melt-filling (PAMF) [34], template transfer [29] and EBL-based hybrid method [24]), can also be considered.

Here, we would like to highlight our work in this field [35]. One major contribution is that the proposed EBL-based method could realize parallel fabrication of complex nanoarrays (nanotrimers, nanodot arrays, metasurfaces, etc.; further discussions are provided in chapter 4) on several fiber end faces [25]. This method allows fibers that are meters long to be obtained, which is not typical for the samples in Table 1-1 (fibers are often limited to 1 cm due to the machine confinements). Further modifications of the implementation procedure may also allow fibers to be made of other materials (such as polymers or elastomers).

Furthermore, we carried out in-depth studies on the optical response of nanostructures in close-packed arrays. With this compact distribution, we

demonstrate the strong spectral tunability of nanostructures by modifying their periodic constants. This phenomenon could greatly help in tailoring the desired optical response and further assist in the on-demand design of nanostructures.

1.3 Arrangement of the thesis

The main purpose of this thesis is to present the complete research process for developing nanostructure-enhanced fibers. To fulfill this purpose, the thesis is arranged as follows:

In the current chapter, we have presented the concept of nanostructure-enhanced fibers, in which a well-defined plasmonic nanoantenna array is integrated on the end face of an SMF-28 fiber for applications in telecommunications, remote sensing, fiber endoscopy, novel optical component design, etc. The background, motivation and state-of-art related to this project have been introduced.

In chapter 2, the research background of nanoplasmonics and optical fibers is explicitly illustrated. We introduce basic concepts in nanophotonic and the working mechanisms of plasmonic effects (e.g., dipole resonance [13], Fano resonance [45]). Since this project concentrates on localized surface plasmon resonance (LSPR), fundamentals related to this optical effect (e.g., resonance condition [14] and near-field dipole-dipole interactions) are presented in great detail. We also provide the basics of fiber optics, such as mode calculations and profiles, to understand the fiber optical properties. It is also necessary to illustrate the major study methods used in this thesis, which are particularly presented in the last section of this chapter.

In chapter 3, from theoretical and experimental perspectives, the design procedures for metallic nanostructures for usage with step-index fibers are demonstrated. Based on the characteristics of SMF-28, we propose three requirements for plasmonic nanostructures. In general, the desired nanoantennas should exhibit a narrow spectral lineshape in the infrared (IR) regime. Here, we mainly investigate a closely packed nanotrimer array, which is further patterned on the end face of fibers. In addition to a dolmen-like electric Fano resonance, this specific nanotrimer arrangement (square-shaped unit cell) breaks the three-fold symmetry of the isolated trimer and induces a magnetic Fano resonance. These unique spectral features (working in the IR regime and asymmetric lineshape) enable experimental characterization of nanotrimer-modified optical fibers.

In chapter 4, we show the nanoengineering process of patterning a trimer array on the facet of fibers by means of electron beam lithography. Through planarization of the fiber surface in a custom can-like holder [25], the fiber substrate can be treated as a planar wafer. The manufacturing workflow for patterning nanostructures can be found in this section. In addition to the nanotrimer array, we also fabricated nanobar-based metasurfaces, nanodot arrays and cross-like four-dot antennas on the end face of optical fibers to verify the reliability and reproducibility of the fabrication techniques.

In chapter 5, we demonstrate the characterization of nanotrimer-based fibers by measuring the transmission contrast. The trimers on a fiber substrate exhibit high spectral similarities with the trimers on a flat silica substrate, where a major dip located at approximately 1.6 μm is captured in both contrast spectra. This result strongly proves that the optical response of the fiber has been modified by the nanostructures. In addition, we employ the nanotrimer-enhanced fiber tip as a refractive index (RI) sensor, which shows a sensitivity of 390 nm/RIU, more than two times higher than those of previously reported LSPR-based fiber sensors [37, 46]. At the end of this chapter, we demonstrate a significant enhancement of the light-collecting ability of nanostructured fibers at oblique incident angles. The nanodot-modified fiber tip displays amplitude improvements of several orders of magnitude compared to bare fibers (without any nanostructure). The significant performance enhancements are further examined with a toy model as well as numerical simulations.

In the last chapter, the results and data obtained in this work are summarized. Improvements of this work and an overview of potential applications are also given.

TABLE 1.1
Summary of various nanostructures on fiber end-face

Refs.	Nanostructure type	Nanostructure material	Fiber type	Applications	Fabrication techniques
[23]	Monopole antenna	Aluminum	SMF at 633 nm	Single molecule fluorescence	FIB
[26]	Nanoslot metasurface	Gold	PCF	Beam shaping	FIB
[28]	Phase-gradient metasurface	Gold	SMF-28	Beam shaping and sensing	FIB
[36]	1D diffraction grating	Si_3N_4/SiO_2	Silica fiber	Optode and sensing	FIB
[31]	Split ring apertures	Gold	Silica fiber	Signal modulation	FIB
[30]	Phase diffractive element	PMMA	SMF-28	Beam shaping	EBL
[27]	Nano-gird/grating	Gold	SMF-28	Fiber inline polarizer	EBL
[37–40]	Nanodisks array	Gold	SMF at 633 nm	Biological sensing	EBL
[41]	Concentric ring grating	Gold	MMF	Sensor	EBL
[25]	Trimers array	Gold	SMF-28	Index sensor	EBL
[34]	Spike-like tip	Gold	Nano-bore fiber	End-fire coupling	PAMF
[29, 42]	Nanohole array	Gold	Large-core fiber	Biomolecular sensing	Template transfer
[24, 43]	Hybrid metallo-dielectric	Dielectric metallic	SMF-28	Chemical and biological sensing	EBL-based hybrid method
[44]	Crescents, rings, split rings, coaxial cylinders, nanowire grating	Metallic	MMF	Surface-enhanced Raman spectroscopy	Nanoskiving-based template tranfer

Chapter 2

Fundamentals of plasmonics and fiber optics

Nanophotonics is a general subject related to many scientific and engineering fields, such as optical engineering, nanofabrication in the silicon industry, and quantum computing, to name but a few. With a focus on light-matter interactions at the nanoscale, the rapid development of nanooptics has enabled fictional concepts (e.g., invisibility cloaks [47, 48]), led to fruitful results (e.g., metasurfaces [49]) and greatly benefited human beings (e.g., cancer diagnostics and treatment by nanoshells [50]).

Plasmonics, being a major part of nanophotonics, mainly investigates the optical physics of ordered and/or disordered metallic nanoparticles and has been extended to nanostructures consisting of dielectrics [51], graphene [52] and so on. Twenty-one years ago, the pioneering work of T. W. Ebbesen on extraordinary light transmission through a nanohole array in a gold thin film [53] led to a new phase in the study of nanoplasmonics. Currently, plasmonic-related nanooptics is still a flourishing and extremely active scientific topic.

On the other hand, fiber optics remains one of the 'hottest' fields, even though it has been intensively studied for more than half a century [4]. In this work, we aim to transfer plasmonic nanostructures to fiber facets. To gain a comprehensive understanding, this chapter aims to provide basic concepts and theoretical foundations in the areas of plasmonics and fiber optics.

Starting from Maxwell's equations, we first present elementary equations of classical electromagnetism. Then, two optical effects - localized surface plasmon resonance (LSPR) and surface plasmon polariton (SPP) - will be addressed in detail. In particular, LSPR represents the major working principle of the entire project, and thus, we emphasize this effect. The Fröhlich resonance conditions, coupling between localized plasmons and Fano resonance are given in this section. Furthermore, we examine the fundamentals

of fiber optics from aspects such as the geometric arrangement, mode profile, and dispersion. Here, we take SMF-28 as a specific example for the overall demonstration. Additionally, the recent advancements in optical fibers will be briefly reviewed. Finally, we summarize commonly used research methods in the field of nanophotonics. With a focus on the spectral behaviors of functional nanostructures, we mainly adopt numerical simulations and experimental spectral measurements to design and optimize ordered nanoparticles for usage with SMF-28.

2.1 Fundamentals

2.1.1 Maxwell's equations

Maxwell's equations are fundamental to understanding how electromagnetic fields are generated and modified by charges, currents, and changes in the fields. This set of functions (consisting of four partial differential equations) bears the name of physicist James Clerk Maxwell for his early and preeminent work in electromagnetism.

Now, we first present Maxwell's equations in free space (without any external source) in the presence of external charge ρ_{ext} and current density $\mathbf{J_{ext}}$, which are given in the following forms [14]:

$$\nabla \cdot \mathbf{D} = \rho_{ext} \tag{2.1a}$$

$$\nabla \cdot \mathbf{B} = 0 \tag{2.1b}$$

$$\nabla \times \mathbf{E} = -\frac{\partial \mathbf{B}}{\partial t} \tag{2.1c}$$

$$\nabla \times \mathbf{H} = \frac{\partial \mathbf{D}}{\partial t} + \mathbf{J_{ext}} \tag{2.1d}$$

Maxwell's equations include Gauss's laws (Eq. 2.1 a and b), Faraday's law (Eq. 2.1 c), and Ampère's law with Maxwell's addition (Eq. 2.1 d). Here, the electric field $\mathbf{E}(\mathbf{r}, t) = \mathbf{E}(\mathbf{r})e^{-i\omega t}$ and the magnetic field $\mathbf{H}(\mathbf{r}, t) = \mathbf{H}(\mathbf{r})e^{-i\omega t}$ are both vector functions of positions $\mathbf{r}$ and time t. $\mathbf{D}$ and $\mathbf{B}$ indicate the dielectric displacement and the magnetic induction, respectively. $\nabla\cdot$ and $\nabla\times$ are the divergence and curl operations, denoted by the nabla symbol ∇. Note that external $(\rho_{ext}, \mathbf{J_{ext}})$ and internal $(\rho, \mathbf{J})$ are separated, such that

$\rho_{tot} = \rho_{ext} + \rho$ and $\mathbf{J_{tot}} = \mathbf{J_{ext}} + \mathbf{J}$. By introducing polarization $\mathbf{P}$ and magnetization $\mathbf{M}$, we obtain the subsequent relations:

$$\mathbf{D} = \epsilon_0 \mathbf{E} + \mathbf{P} \tag{2.2a}$$

$$\mathbf{H} = \frac{1}{\mu_0}\mathbf{B} - \mathbf{M} \tag{2.2b}$$

Here, the vacuum electric permittivity constant is represented by ϵ_0, with a value $\approx 8.854 \times 10^{-12} F/m$, and the magnetic permeability μ_0 is $\approx 1.257 \times 10^{-6} H/m$. Henceforth, we only consider a linear, isotropic and nonmagnetic medium. Accordingly, Eq. 2.2 can be modified as follows [14]:

$$\mathbf{D} = \epsilon_0 \epsilon \mathbf{E} \tag{2.3a}$$

$$\mathbf{B} = \mu_0 \mu \mathbf{H} \tag{2.3b}$$

where ϵ and μ are the relative permittivity and relative permeability, respectively (in a nonmagnetic medium $\mu = 1$). Alternatively, Eq. 2.3 can be defined by the electric susceptibility χ_e and magnetic susceptibility χ_m, which leads to

$$\mathbf{P} = \epsilon_0 \chi_e \mathbf{E} \tag{2.4a}$$

$$\mathbf{M} = \chi_m \mathbf{H} \tag{2.4b}$$

Hence the refractive index (RI) can be expressed as $n = \sqrt{\epsilon} = \sqrt{1 + \chi_e}$, indicating that RI ($n$) is the square root of ϵ, and the light speed constant in free space can be obtained by $c_0 = 1/\sqrt{\epsilon_0 \mu_0}$.

2.1.2 Optical properties of metals and glasses

Dielectric function of metals

The optical property of metals can be analyzed by a plasma model assuming that a gas of free electrons moves against a fixed background of positive ion cores. The electrons would oscillate corresponding to the applied electromagnetic field, and their motions are damped due to collisions, which is further indicated by a characteristic collision frequency $\gamma = 1/\tau$ (τ is the relaxation time of the free electron gas). Thereby, the dielectric function of free electron gas can be defined as follows [14]:

$$\epsilon(\omega) = 1 - \frac{\omega_p^2}{\omega^2 + i\gamma\omega} \tag{2.5}$$

where ω_p is the metal plasma frequency, which corresponds to the eigenfrequency of the electronic oscillation.

Hence, the real and imaginary parts of the complex dielectric function ($\epsilon(\omega) = \epsilon_1(\omega) + i \cdot \epsilon_2(\omega)$) are given by

$$\epsilon_1(\omega) = 1 - \frac{\omega_p^2 \tau^2}{1 + \omega^2 \tau^2} \tag{2.6a}$$

$$\epsilon_2(\omega) = \frac{\omega_p^2 \tau}{\omega(1 + \omega^2 \tau^2)} \tag{2.6b}$$

Qualitatively, two different mechanisms [54] (Drude model and Lorentz model) contribute to $\epsilon(\omega)$ in metals (i.e., $\epsilon = \epsilon_{Drude} + \epsilon_{Lorentz} + ...$).

- Drude-Sommerfeld contribution $\epsilon_{Drude}(\omega)$

  $$\epsilon(\omega) = \epsilon_\infty - \frac{\omega_p^2}{\omega^2 + i\gamma\omega} \tag{2.7}$$

  where ϵ_∞ is the residual polarization, with a value of $1 \leq \epsilon_\infty \leq 10$.

- Drude-Lorentz contribution $\epsilon_{Lorentz}(\omega)$

  The effect of electronic inter-band transitions can be taken into account in $\epsilon(\omega)$ by means of a Lorentz-modified item:

  $$\epsilon(\omega)_{Lorentz} = \frac{\Delta\epsilon\Omega_p^2}{\Omega_p^2 - \omega^2 - i\Gamma\omega} \tag{2.8}$$

  where Ω_p and Γ are the plasma and damping frequencies for the bound electrons, respectively, in analogy to Eq. 2.7, and $\Delta\epsilon$ weights the contribution of the given interband transition to the dielectric function.

In Fig. 2.1, the measured data of the real (ϵ_1) and imaginary (ϵ_2) components of the permittivity of gold and silver within a wavelength range from 200 nm to 1900 nm are separately plotted in (a) and (b). These experimental data are obtained from refs. [55, 56]. Comparing the two noble metals, they exhibit a high similarity, where ϵ is governed by the large negative real part ϵ_1, especially for wavelength > 550 nm. In addition, considering the theoretical model (see an example in this ref. [14]), the Drude contributions well fit the measured data at a larger wavelength range (roughtly λ > 400

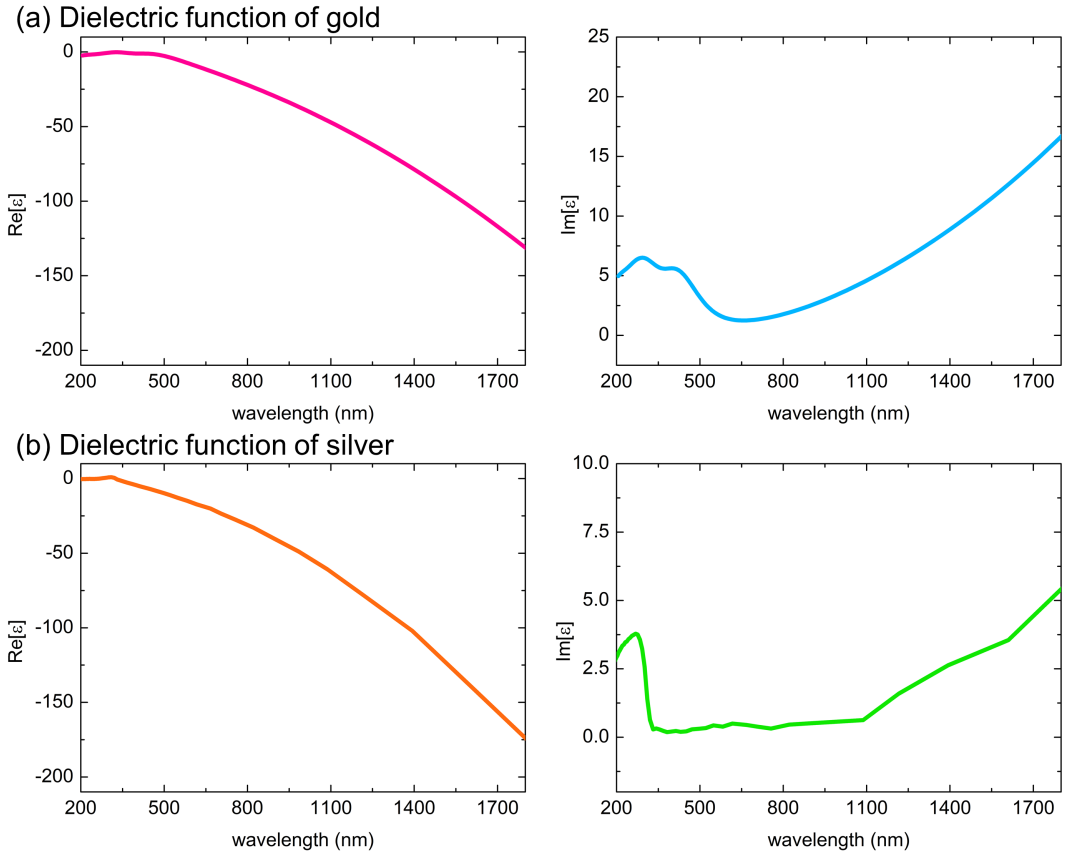

FIGURE 2.1
Dielectric function of gold (a) and silver (b). Re[ϵ] and Im[ϵ] represent $\epsilon_1(\omega)$ and $\epsilon_2(\omega)$, respectively.

nm), whereas they cannot reproduce the increase of metal absorption losses at short wavelengths. This mismatch can be amended by adding Lorentzian terms to the Drude model.

Sellmeier equation and optical loss of SiO_2

The rapidly development of fiber optics has benefited from low-loss glassy material. Among these glasses, fused silica (amorphous silicon dioxide, SiO_2) is the dominating material in fiber optics, especially for optical telecommunications [57]. Therefore, in this section, we would like to briefly introduce the optical properties of this transparent medium, whose refractive index can be approximated by the Sellmeier equation. The Sellmeier equation is an empirical relationship used to determine the frequency-depended refractive index. In general, the Sellmeier equation can be expressed as [58]

$$n^2(\lambda) = 1 + \sum_{k=1}^{n} \frac{B_k \lambda^2}{\lambda^2 - C_k} \tag{2.9}$$

where n and λ are the refractive index and vacuum wavelength, respectively. B_k and C_k are Sellmeier coefficients obtained from experimental measurement. For instance, the RI of fused silica is given by [59]

$$n^2_{silica}(\lambda) = 1 + \frac{0.6961663\lambda^2}{\lambda^2 - 0.0684043^2} + \frac{0.4079426\lambda^2}{\lambda^2 - 0.1162414^2} + \frac{0.8974794\lambda^2}{\lambda^2 - 9.896161^2} \quad (2.10)$$

Note that in this thesis, due to the small RI variations of fused silica (from VIS to NIR region), ϵ_{silica} ($= n^2_{silica}$) in numerical simulation models (a simulated example is given in chapter 3) is often fixed at 2.09 for convenience.

Finally, we can review the intrinsic losses of fused silica (an example for the loss spectrum in ref. [57]). Overall, the optical loss is below 1 dB/km within the wavelength ranging from 1 μm to 1.8 μm. At shorter wavelengths (from 1 μm to 1.4 μm), Rayleigh scattering ($\propto \lambda^{-4}$) is the main reason for the optical loss, further increasing the value to a few dB/km in the visible regime. The infrared absorption related to multiphonon absorption (vibrational resonances) dominantly contributes to the loss at longer wavelengths (from approximately 1.65 μm to 1.8 μm). At 1.55 μm, the loss reaches a minimum value of $\ll$ 0.1 dB/km, which is located at telecommunication C band (1530-1565 nm). In addition, there are five more communication bands in this regime including O band (1260-1360 nm), E band (1360-1460 nm), S band (1460-1530 nm), L band (1565-1625 nm), and U band (1625-1675 nm).

2.2 Plasmonic resonance at the nanoscale

2.2.1 Surface plasmons

Plasmonics is the study of physical phenomena induced by and closely associated with surface plasmons [60–62]. Currently, an increasing number of studies (over 6000 related publications in 2011 [63]) have intensively focused on two types of surface plasmon effects. One (sketch in Fig. 2.2 (a)) is the propagating surface waves named surface plasmon polaritons (SPPs), and the other (Fig. 2.2 (b)) is a 'nonpropagating' excitation called localized surface plasmon resonances (LSPRs).

Surface plasmon polaritons

Surface plasmon polaritons represent an optical phenomenon in which an electromagnetic wave propagates along the interface (along x axis in Fig.

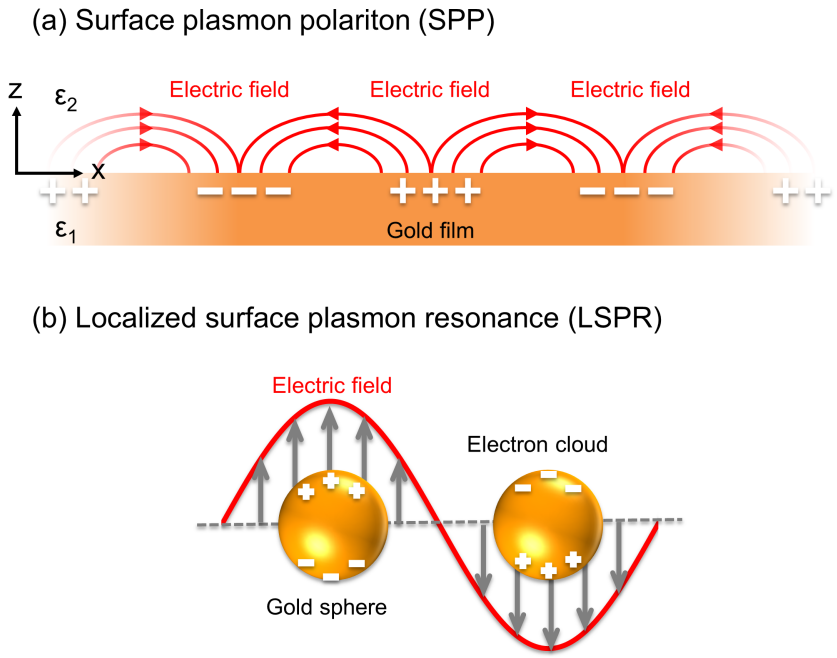

FIGURE 2.2
Sketches of surface plasmon polaritons (a) and localized surface plasmon resonances (b).

2.2 (a)) between a metal and a dielectric (or air) with the maximum intensity along this surface while the electric field exponentially decaying perpendicular to this interface (along z axis in (a)) [14, 64–66]. The electromagnetic surface waves are associated with the collective oscillation of the free electrons in the metal.

Schematically shown in Fig. 2.2 (a), a flat and smooth gold film (orange background, relative permittivity ϵ_1) sustains a travelling electric field (red curves and arrows) confined between this thin film and air (relative permittivity ϵ_2). We define β as the propagation constant of the traveling waves of SPPs (k_0 is the wave number of light wave in vacuum). Hence, the physical model of SPPs can be given by the following equation [14]:

$$\beta = k_0 \sqrt{\frac{\epsilon_1 \epsilon_2}{\epsilon_1 + \epsilon_2}} \tag{2.11}$$

Eq. 2.11 is named as the dispersion relation of SPPs. Note that SPPs only exist for TM polarization [14].

To excite SPPs, additional phase matching techniques are employed with the help of a coupling medium such as a prism or a grating [14]. For instance, the commonly used Kretschmann configuration involves placing a

prism against a thin metal film. The light passes through the prism and illuminate the film at an incidence angle greater than the critical angle of total internal reflection (TIR).

Due to the energy loss of metals [56], SPPs cannot travel a long distance. An example of the calculated propagating length is close to 1080 μm at the wavelength of 1.5 μm assuming a silver/air interface [14]. A general conclusion is that stronger electromagnetic field confinement leads to a shorter propagation length.

From a practical application perspective, SPPs are widely used for novel plasmonic waveguides [67, 68], light concentrator [69], plasmonic sensors [70], plasmonic circuits [71, 72]. Particularly, by filling the air channel of microstructured fibers (e.g., photonic crystal fiber [6] and nano-bore fiber [73]) with metallic nanowires, SPPs are also demonstrated within optical fibers framework [7, 74]. These in-fiber SPPs open new possibilities for fiber-based concentrators [75], near-field detectors [76], and miniaturized nonlinear devices [77].

Localized surface plasmon resonances

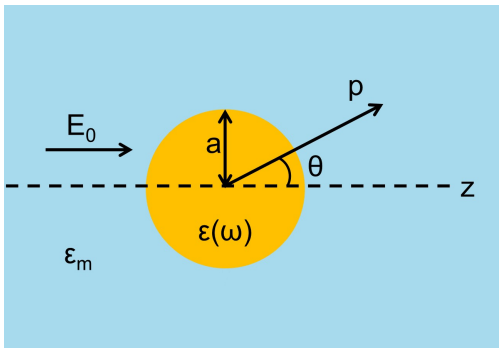

FIGURE 2.3
A schematics of a sphere ($\epsilon(\omega)$) inserted a medium (ϵ_m) with electrostatic field E_0. This image is inspired from ref. [14].

Unlike SPPs, LSPRs are nonpropagating excitations [54, 78] and can be excited by direct light illuminations without any assistance from a phase-matching technique [79, 80]. The mechanism of LSPRs is illustrated in Fig. 2.2 (b). Here, light (in the form of an electric field, red curve) interacts with gold spheres (two yellow circles) whose diameters are much smaller than

the incident wavelength. The interplay (indicated by the grey arrows) between subwavelength nanoparticles and light leads to a plasmon that oscillates locally around the gold nanospheres. The free conduction electrons in the metal nanoparticle are driven into oscillation (resonance) [81].

Now we would like to present the Fröhlich resonance condition in the case of a sphere ($\epsilon(\omega)$, radius: a) embedded in a medium (ϵ_m, isotropic and non-absorbing material) under quasi-static approximation ($a \ll \lambda$, sketch shown in Fig. 2.3.). The general solutions of potentials Φ_{in} (inside the sphere) and Φ_{out} (outside the sphere) based on this model can be written as [14]

$$\Phi_{in} = -\frac{3\epsilon_m}{\epsilon(\omega) + 2\epsilon_m} E_0 r \cos\theta \tag{2.12a}$$

$$\Phi_{out} = -E_0 r \cos\theta + \frac{\epsilon(\omega) - \epsilon_m}{\epsilon(\omega) + 2\epsilon_m} E_0 a^3 \frac{\cos\theta}{r^2} \tag{2.12b}$$

Here θ denotes the angle between the position vector $\mathbf{r}$ (at point p) and the z-axis (see Fig. 2.3). Eq. 2.12 (b) can be generally interpreted as the E-field superposition of applied field E_0 and a dipole field $\mathbf{p}$ situated at the sphere center. By introducing the dipole moment $\mathbf{p}$, we rewrite Eq. 2.12 (b) in the following form [14].

$$\Phi_{out} = -E_0 \mathbf{r} \cos\theta + \frac{\mathbf{p} \cdot \mathbf{r}}{4\pi\epsilon_0\epsilon_m r^3} \tag{2.13a}$$

$$\mathbf{p} = 4\pi\epsilon_0\epsilon_m a^3 \frac{\epsilon(\omega) - \epsilon_m}{\epsilon(\omega) + 2\epsilon_m} \mathbf{E_0} \tag{2.13b}$$

Now, we arrive at the conclusion that the applied E-field induces a dipole moment with a value proportional to $|\mathbf{E_0}|$ according to Eq. 2.13.

By substituting the polarizability α via $\mathbf{p} = \epsilon_0\epsilon_m\alpha\mathbf{E_0}$, we can obtain the formula of Fröhlich resonance condition [14].

$$\alpha = 4\pi a^3 \frac{\epsilon(\omega) - \epsilon_m}{\epsilon(\omega) + 2\epsilon_m} \tag{2.14}$$

To enhance the dipole moment supported by this sphere, the polarizability α is set to the maximum value provided that $\epsilon(\omega) + 2\epsilon_m$ is sufficiently small. Therefore, under the case of small or slowly varying Im $[\epsilon(\omega)]$, the Fröhlich resonance condition requires $Re[\epsilon(\omega)] = -2\epsilon_m$. For gold and silver nano-spheres, the Fröhlich resonance wavelengths are located in the visible region. As a consequence, a bright color (scattered from these nanoscale particles) can be observed when they are illuminated by light under resonance conditions.

In addition, the Fröhlich resonance condition illustrate that the resonance frequence ω can be altered due to the presence of a host medium ϵ_m. In chapter 5, we further explore resonance-induced redshift of gold trimers by increasing the refractive index of surrounding medium.

To evaluate the sphere behaviour regarding light, scattering (C_{sca}), absorption (C_{abs}), and extinction (C_{ext}) cross-sections are commonly employed. In general, C_{abs} determines the particle's capacity to absorb light, while C_{sca} measures how strongly the particle can scatter light. The corresponding cross-sections can be calculated via the Poynting vector. For a sphere with volume of V ($V = \frac{4}{3}\pi a^3$ for the sphere in Fig. 2.3) and permittivity $\epsilon(\omega) = \epsilon_1 + i\epsilon_2$, these cross-sections can be expressed as [14]

$$C_{sca} = \frac{k^4}{6\pi}|\alpha|^2 = \frac{8\pi}{3}k^4a^6\left|\frac{\epsilon(\omega)-\epsilon_m}{\epsilon(\omega)+2\epsilon_m}\right|^2 \tag{2.15a}$$

$$C_{abs} = kIm[\alpha] = 4\pi ka^3 Im\left[\frac{\epsilon(\omega)-\epsilon_m}{\epsilon(\omega)+2\epsilon_m}\right] \tag{2.15b}$$

$$C_{ext} = C_{abs} + C_{sca} = 9\frac{\omega}{c}\epsilon_m^{3/2}V\frac{\epsilon_2}{[\epsilon_1+2\epsilon_m]+\epsilon_2^2} \tag{2.15c}$$

The scattering coefficient (Q_{sca}), absorption coefficient (Q_{abs}), and extinction coefficient (Q_{ext}) correspond cross-sections normalized to the geometric size (πa^2) of the particle.

$$Q_{sca} = \frac{C_{sca}}{\pi a^2}, \quad Q_{abs} = \frac{C_{abs}}{\pi a^2}, \quad Q_{ext} = \frac{C_{ext}}{\pi a^2} \tag{2.16}$$

From an experimental prospective, we assume that the ordered and/or disordered nanoparticles are assembled on a planar surface within a certain area (each particle has a size of s in average). To measure the optical spectrum, some of particles (excited number N) are illuminated by a beam with spot size of S. Once transmission (T) of plasmonic particles is determined, the extinction spectrum, extinction cross-section and extinction coefficient can be obtained by the subsequent formulas.

$$Extinction = 1 - T \tag{2.17a}$$

$$C_{ext} = S(1-T) \tag{2.17b}$$

$$Q_{ext} = S(1-T)/(N\cdot s) \tag{2.17c}$$

Corresponding transmission (T) and extinction spectral measurements

are further demonstrated in chapter 3, where the optical setup and experimental procedures are shown in great detail.

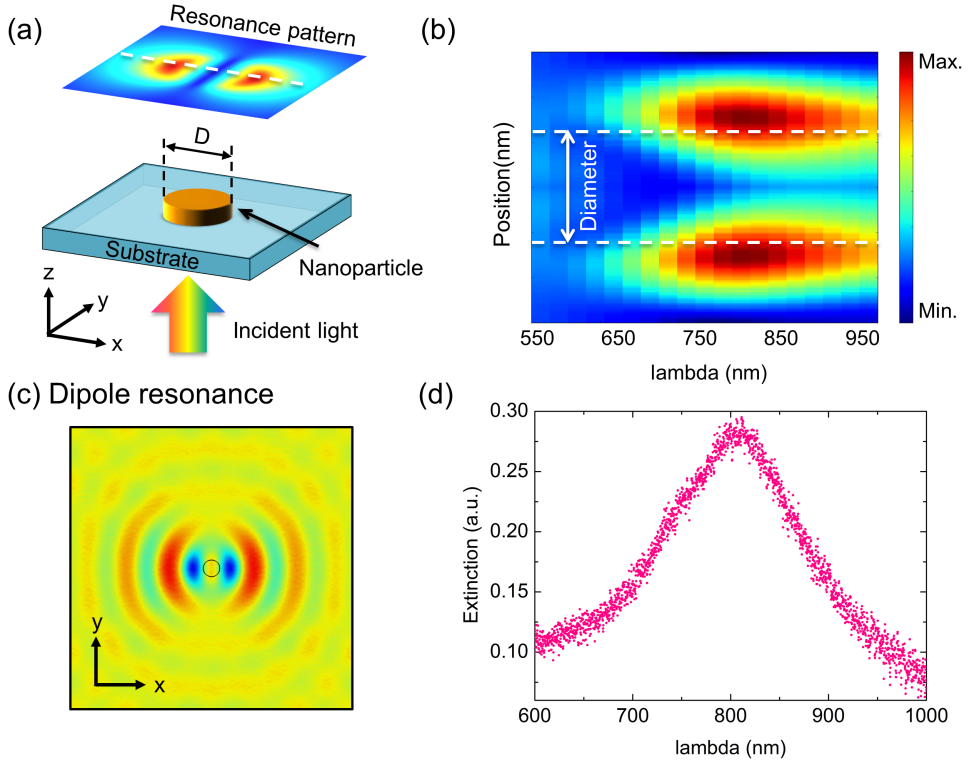

FIGURE 2.4

(a) A typical experimental configuration for excitation of LSPRs. A gold nanodisk fabricated on the surface of a silica substrate is illuminated by normal incident light. (b) A colored map showing the correlation of the E-field and nanodisk diameter. The E-field, indicated by the dashed white line in (a), is distributed along the center of resonance pattern. (c) Dipole resonance electromagnetic field generated by the gold nanodisk (located at center). (d) Measured extinction spectrum (1-T) of an array of nanodots (diameter: 200 nm). The Lorenz-like spectral lineshape shows a central resonance wavelength at approximately 800 nm.

E-field amplification and confinement are major consequences of LSPRs. To give an impression of the E-field enhancement, we illustrate the LSPR effect by plotting the near-field patterns of a gold nanodisk together with its optical spectrum in Fig. 2.4 (a). This gold nonodisk (orange, indicated by the label 'nanoparticle' with a diameter of D) is placed on a flat silica substrate ($\epsilon_{substrate} = 2.09$) and exposed to air ($\epsilon_{air} = 1$). Excited by a normal incident beam (colored arrow at the bottom), the gold nanodisk can generate a dipole resonance pattern (at a plane of 10 nm height above the top surface of this nanodisk), where the E-fields around the edges of the dot is significantly

enhanced. The dipole resonance pattern is further displayed in Fig. 2.4 (c). The central black circle here is the projected contour of the nanodisk.

Now, we can determine the resonance spectral span by inspecting the E-field enhancement and far-field extinction (or transmission or scattering) spectrum. Here, we plot near-field distributions and present the extinction of gold nanodots in Fig. 2.4 (b) and (d), respectively. Obtained by FEM-based commercial software (COMSOL Multiphysics 4.3 a; the details of the simulation model are shown in chapter 3), the electromagnetic fields along the central line of the resonance patterns (indicated by a white dashed line in (a)) are plotted for examination.

Here, two dashed white lines in (b) indicate the nanodisk diameter and its position. According to the E-field enhancements shown in (b), the central resonance wavelengths are located at approximately 800 nm in the air-glass media configuration. This wavelength matches the extinction spectrum (obtained by 1-T) in Fig. 2.4 (d), which exhibits a symmetrical lineshape.

In next sessions, we focus on how to manipulate the resonance lineshape, e.g., to shift the resonance central wavelength using the particle geometry. This information is of great interest for the design of nanostructures for usage with optical fibers.

2.2.2 Geometry/size dependence

Generally, the spectral lineshape of LSPRs can be altered by many parameters, included, but not limited to, the nanoparticle size, geometry and environments [54]. Here three main factors of modifying resonance behaviours would be discussed in detail. These are listed in following sections as geometry/size dependence (e.g., particle length), near-field coupling (e.g., the edge-to-edge distance of a nanodot pair), and Fano-like resonance.

In this section, we will explore particle geometry influence on spectral response [82]. We first assume a physical background similar to the arrangement in Fig. 2.3. However, this time, the sphere is replaced by an ellipsoid with semi-axes ($a_1 \leq a_2 \leq a_3$). The polarizabilities α_i along the principle axes

(i.e., i = 1, 2, 3) can be expressed as [14]

$$\alpha_i = 4\pi a_1 a_2 a_3 \frac{\epsilon(\omega) - \epsilon_m}{3\epsilon_m + 3L_i(\epsilon(\omega) - \epsilon_m)} \tag{2.18a}$$

$$L_i = \frac{a_1 a_2 a_3}{2} \int_0^\infty \frac{1}{(a_i^2 + q) f(q)} dq \tag{2.18b}$$

$$f(q) = \sqrt{(q + a_1^2)(q + a_2^2)(q + a_3^2)} \tag{2.18c}$$

where L_i is the geometric factor.

The geometry (i.e., a_1, a_2, and a_3) of a metallic ellipsoid can affect polarizability α, which further affects the dipole moment via $\mathbf{p} = \epsilon_0 \epsilon_m \alpha \mathbf{E_0}$. This means that the nanoparticle geometry can influence the LSPR resonance wavelength under the assumption that particle radius a is less than wavelength λ. We will further explore geometry dependence under the condition that the nano-particle size approaches the illumination wavelength in chapter 3.

In addition, theoretical studies (such as Mie theory [83]) have predicted the spectra of nanoparticles. For instance, Kuwata *et al*. illustrated an empirical analytical formula for gold and silver spherical particles, which was further verified by experimental data [84]. For more information, we encourage readers to examine these references [85–87].

Perhaps the most intuitive way to understand the surface plasmon geometry/size dependency is to observe vibrant colors scattered from metallic nanostructure [88, 89]. In general, these different colors represent resonance wavelengths corresponding to freely dispersed nanoparticles in liquids [90]. Based on this mechanism, several reports have recently employed these plasmonic nanoparticles in novel color display technology. For example, Xiaoyuan Duan *et al*. demonstrated a scanning plasmonic color generation scheme that could be switched on/off through directional hydrogenation/dehydrogenation [91].

2.2.3 Near-field coupling

The second factor that can modify optical response of a metallic nanoscale structure is the electromagnetic interactions between the local plasmon modes. Here, we address this issue within a scheme of dipole-to-dipole coupling (i.e., higher order mode interactions are beyond the scope of this thesis).

For a proper introduction, we will demonstrate near-field coupling effects using gold nanoparticles from the aspects of (i) a one-dimensional chain, (ii)

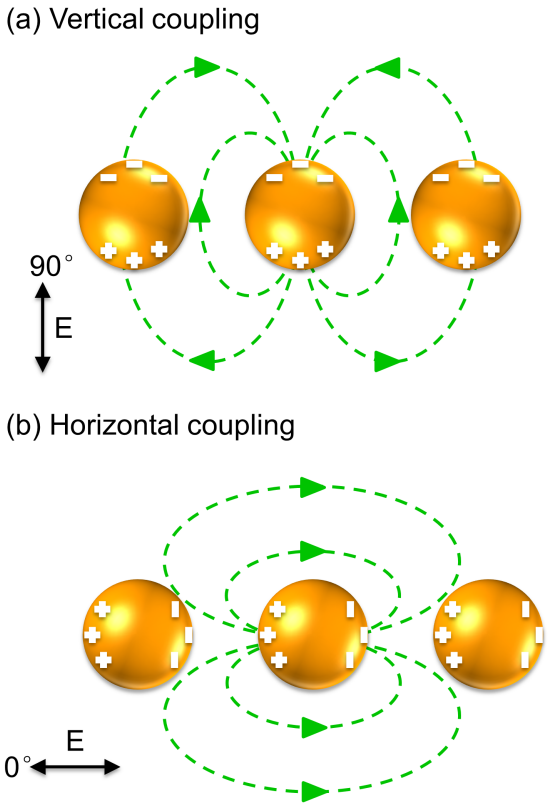

FIGURE 2.5
Near-field coupling of localized plasmons along the vertical direction (a) and horizontal direction (b). This sketch is inspired from ref. [14].

two-dimensional coupled pairs, and (iii) a closely-packed lattice. Note that in second case, Au pairs are distributed in sparse unit cell (the interactions between cells can be ignored), while diffractive couplings of unit cells becomes strong in the third situation (lattice resonance).

Spectral shift in a 1D plasmonic chain

The physical background to address this near-field coupling issue is a one-dimensional plasmonic chain formed by evenly distributed gold particles, in which particles' edge-to-edge distance d is much smaller than incident wavelength λ. As depicted in Fig. 2.5, a gold nanoparticle chain is excited by 90° and 0° polarized light, resulting in the vertical (a) and horizontal couplings (b), respectively.

The direction of the spectral shift of the LSPR position is determined by the near-field coupling circumstance, where Coulomb forces among particles interact along different axis [14]. Therefore, the restoring force acting on the oscillating electrons of each particle is either decreased or increased by the

charge distribution of neighbouring particles, leading to a blueshift for longitudinal modes (a) and a redshift of transverse modes (b). The resonance spectral shifts are demonstrated in Fig. 2.6. Here, λ_0 is the original resonance central wavelength, while λ_1 and λ_2 are the shifted spectral positions.

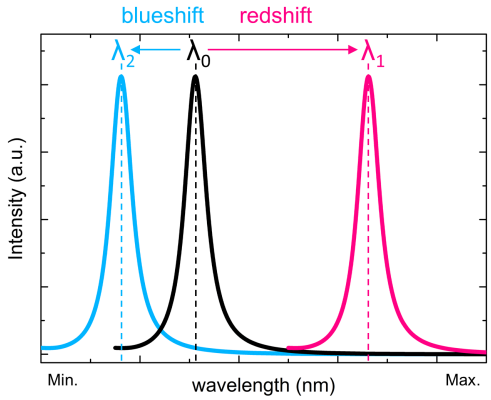

FIGURE 2.6
A sketch showing spectral redshift and blueshift induced by near-field coupling. The spectra are obtained from simulations.

Note that under this closely spaced arrangement ($d \ll \lambda$ in particle chains), the near-field interaction with a distance dependence of d^{-3} dominates, while the dipolar coupling with a distance dependence of d^{-1} dominates in the far field for the case of larger particle separations. [14]

Resonance evolution of 2D coupled nanoparticle pairs

For the next topic, we would like to discuss spectral evolution of the coupled Au nanodisk pairs under a geometric distribution in which two nanoparticles come into close contact. This is a good example for understanding the spectral evolution of complex nanostructures in two-dimensional distributions. As illustrated in Fig. 2.7, d and D represent the interparticle edge-to-edge separation and the particle diameter, respectively.

In general, excited by 0° or 90° polarized light, the Au pairs exhibit spectral behaviour akin to the plasmonic chain [92, 93]. Under parallel polarization illumination (0°, magenta), the plasmon resonance strongly transits to a longer wavelength (redshift, from λ_0 to λ_1 in Fig. 2.6) as the interparticle gap d is reduced. In contrast, there is a very slight blueshift (from λ_0 to λ_2) for orthogonal (90°, blue) polarization with decreasing gap d.

Based on this spectral behaviour, several studies proposed the plasmon ruler [94], which is intended to measure nanoscale distances within chemical

or biological species via a simple exponential function. Here, a valid configuration [95] of a plasmon ruler requires that the separation distance d be at least less than two particle diameters D. For further information, please check these references [95–97].

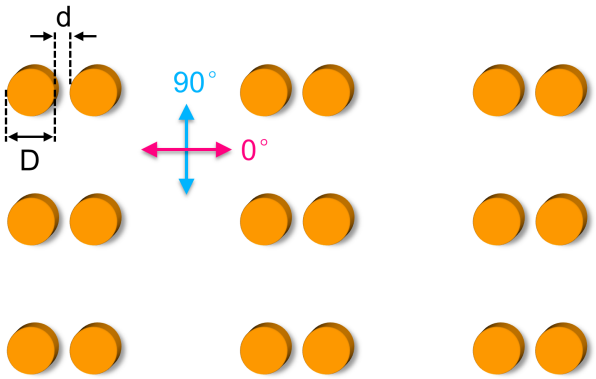

FIGURE 2.7
Coupled Au pair excited by 0° (magenta) and 90° (blue) polarized light.

Lattice resonances in an ordered array

As discussed in Fig. 2.7, Au pairs are distributed a lattice configuration where the periodical constant is not at same scale as the particle size. Under this arrangement, the near-field pair-to-pair coupling is much weaker due to the sufficient geometric distance. However, when the LSPR wavelength of particle is commensurate with the periodicity of the array, electromagnetic coupling between unit cells occurs, leading to the emergence of so-called lattice resonance.

Lattice resonance has been intensively discussed as surface lattice resonance (SLR) [98, 99] in the plamonics community. The spectral position of the sharp transmission dip caused by SLRs can be modified by tuning the corresponding geometric parameters (e.g., increasing the pitch imposes a spectral redshift [98]). Since first experimental SLR demonstration with a nanorod array [98], various structures, such as arrays of nanodots [100–104], disks dimers [105, 106], and split-ring resonators [107], have been investigated to explore the fundamentals of this collective resonance along with its applications, such as an ultra-narrow absorber [108], fluorescent emission shaping [109] and organic molecule excitation [110].

Here, we introduce a general formula [102] predicting spectrum lineshape mediated by the SLR effect. Assuming that identical nanoparticles are placed

in an array, the polarizability α of a single isolated nanoparticle is introduced as α^* by inserting an array factor S.

$$\alpha^* = \frac{1}{1/\alpha - S} \tag{2.19}$$

S is given by

$$S = \sum_j exp(ikr_j)\left[\frac{(1-ikr_j)(3\cos^2\theta_j - 1)}{r_j^3} + \frac{k^2\sin^2\theta_j}{r_j}\right] \tag{2.20}$$

where r_j is the distance from the central particle to particle j and θ_j is the angle between $\vec{r_j}$ and the dipole moment j.

Hence, the extinction cross-section C_{ext} of SLR in densely packed arrays of plasmonic particles is rewritten as

$$C_{ext} = C_{abs} + C_{scat} \tag{2.21a}$$

$$C_{abs} = 4\pi k Im(\alpha^*) \tag{2.21b}$$

$$C_{sca} = \frac{8}{3}\pi k^4 |\alpha^*|^2 \tag{2.21c}$$

2.2.4 Fano resonance

In a work [111] published in 1961, Ugo Fano derived an analytical formula (known as Fano formula) for an asymmetric spectral lineshape for the quantum mechanical study of the autoionizing states of atoms. Nowadays, multiple researches [45, 112–114] have revealed that the microscopic origin of Fano resonance is the constructive or destructive interference of a narrow discrete dark resonance with a broad spectral line or continuum.

Now, we focus on the Fano resonance supported by an individual plasmonic nanostructure. The fundamental criterion for this type of resonance is the spectral overlap between a broad bright resonance and a narrow dark resonance [115]. We depict the working principle in Fig. 2.8. Here, the bright mode is excited by external electromagnetic excitation, and the dark mode can be triggered by near-field coupling. Destructive or constructive interference between these two modes leads to a spectrum with an asymmetric lineshape. The lineshape of the dark mode ($\sigma_a(\omega)$) can be illustrated as [115]

$$\sigma_a(\omega) = \frac{\left(\frac{\omega^2-\omega_a^2}{2W_a\omega_a} + q\right)^2 + b}{\left(\frac{\omega^2-\omega_a^2}{2W_a\omega_a}\right)^2 + 1} \tag{2.22}$$

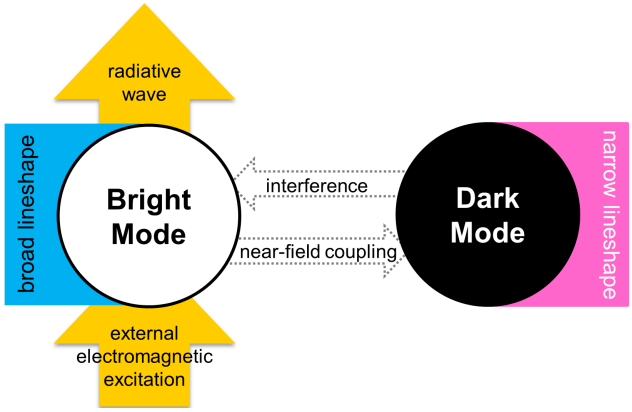

FIGURE 2.8
Working principle of Fano resonances in a plasmonic nanostructure. The constructive or destructive interference between a bright mode and a dark mode would introduce Fano resonances such that the scattering spectrum becomes asymmetric.

where ω_a is the dark mode resonance central position (frequency), W_a estimates the spectral width ($W_a \ll \omega_a$), q is the asymmetry factor, and b is the modulation damping parameter.

The bright mode $\sigma_s(\omega)$ is as follows: [115]

$$\sigma_s(\omega) = \frac{a^2}{\left(\frac{\omega^2-\omega_s^2}{2W_s\omega_s}\right)^2 + 1} \tag{2.23}$$

where a is the maximum resonance amplitude, ω_s is bright mode resonance frequency, and W_s gives an approximation of the spectral width under the assumption of $W_s \ll \omega_s$. Hence, the interference of the bright mode and dark mode leads to

$$\sigma_t(\omega) = \sigma_s(\omega) \cdot \sigma_a(\omega) \tag{2.24}$$

In most situations, this analytical function $\sigma_t(\omega)$ can describe theoretical or experimental spectra such as reflectance, transmission, absorbing, or extinction cross-section [115]. In addition to Eq. 2.24, there are also various theories to analyze Fano resonance in plasmonic nanostructure. For more detailed studies, please examine these corresponding references [114, 116–118]. We will continue to study the so-called electric- and magnetic-based Fano resonances supported by gold trimer arrays in chapter 3.

2.3 Fiber optics

2.3.1 Fiber characteristics

An optical fiber is intended to guide light over hundreds of kilometer. There are numerous advantages [119] making fiber the ideal platform for use in the modern telecommunication industry, including ultralow loss, large bandwidth, immunity to external interference (e.g., electromagnetic interference), small size, and light weight.

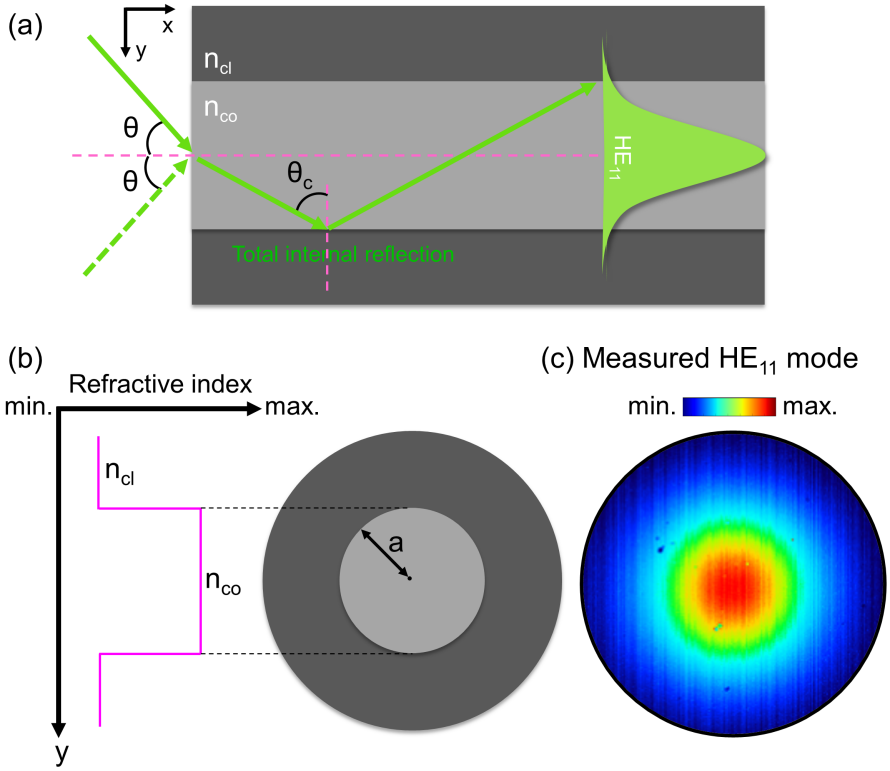

FIGURE 2.9
Cross-section view (a) and top view (b) of a short piece of fiber. This fiber consists of a core (light grey, RI of n_{co}) and a cladding (dark grey, RI of n_{cl}). θ_c stands for the critical angle of total internal reflection. The refractive index profile (magenta step-like curve, $n_{co} > n_{cl}$) is demonstrated in (b) together with a measured HE_{11} mode image in (c) (obtained from an SMF-28 fiber). Here, a represents fiber core radius.

As the cross-section sketched in Fig. 2.9, an optical fiber is typically composed of a core (light grey), a cladding (dark grey), and a coating (outside layer, not shown in this figure) [120]. The fiber core is the region where the majority of light intensity is confined. Typically, for the widely used telecommunication fiber, the core is made of silica or doped silica with a higher RI

than the cladding ($n_{co} > n_{cl}$). The cladding (diameter of 125 μm for SMF-28) is an outer layer around the core and is also made of silica or doped silica. The coating is an additional non-optical layer around the cladding. In addition, for real-world applications, optical fibers are commonly packed as cables (similar to electrical cables) containing single or multiple fibers. In this case, there are more mechanical layers (an outer jacket, strength members, a buffer, etc.) for protection.

From geometric ray optics aspect, total internal reflection (TIR) (owing to the RI difference) is the fundamental working mechanism for optical fibers [2, 121]. Fig. 2.9. (a) describes TIR when the propagating light (green lines) reaches the interface between the fiber core and cladding. If the incidence angle is greater than a certain degree (the angle is defined with respect to the normal to the core-cladding interface, i.e., θ_c in Fig. 2.9 (a)), the light will be reflected back to the fiber core [122]. Here, this critical angle θ_c is given by

$$\theta_c = \sin^{-1}(\frac{n_{cl}}{n_{co}}) \tag{2.25}$$

Correspondingly, the numerical aperture (NA) of a fiber is defined as a sine function of the angle θ (labeled in Fig.2.9 (a), namely, acceptance angle) at which TIR occurs.

$$NA_{fiber} = \sin\theta = \sqrt{n_{co}^2 - n_{cl}^2} \tag{2.26}$$

Note that NA_{fiber} is a key parameter to evaluate fiber light-gathering ability, indicating how 'easy' it is to couple a beam into the fiber. NA_{fiber} is commonly determined by measuring the far-field beam profile emerging from a cleaved fiber tip [119]. Coupled with an LED or a laser source, the output light from a fiber is projected onto a screen. Once the beam spot radius R (commonly measured from the spot center with I_{max} to 5% power level $I_{max}/20$ [123]) and the distance D (from the fiber to the screen) are quantified, the acceptance angle θ and NA_{fiber} can be acquired by the following equations.

$$\theta = \arctan(R/D) \tag{2.27a}$$

$$NA_{fiber} = \sin\theta = \frac{R}{\sqrt{R^2 + D^2}} \tag{2.27b}$$

We will continue to discuss the fiber light-collecting ability in chapter 5 and demonstrate the significant improvement in the fiber in-coupling efficiency obtained by integrating plasmonic nanostructures.

According to its structure and index distribution, an optical fiber can be generally classified as a step-index fiber (SIF) and a graded-index fiber (GIF) [119]. Within this chapter, we focus on the SMF-28 (a typical SIF) to present fundamentals of fiber optics. We plot an RI profile of SIF in Fig. 2.9 (b) together with an image (c) displaying HE_{11} mode (the profile is obtained from an SMF-28 fiber). Resembling a step-like function, a uniform index of n_{co} with a higher value is distributed within the core area, while the index decreases in the cladding to n_{cl}.

From the perspective of electromagnetic theory, the light propagating along z-axis in the fiber geometry is generally described as

$$\mathbf{E}(t,z) = E_0 \exp\left[-\alpha z/2 + j(\beta_j z - \omega t)\right] \tag{2.28}$$

where α is the attenuation coefficient and $\beta_j = n_{eff} 2\pi/\lambda = n_{eff} k_0$ is the propagation constant of different modes in fiber.

We first examine fiber loss in terms of the attenuation coefficient α. In general, the optical loss of commonly used fibers is below 1 dB/km within the wavelength range from 1 μm to 1.8 μm [22, 119]. There is an additional loss peak near 1.4 μm with a value above 1 dB/km (a measured GeO_2-SiO_2 fiber is shown in ref. [124]). This loss peak is caused by the overtones of OH ion absorption (fundamental vibrational absorption peak at around 2.73 μm), which is inevitably introduced during the fiber fabrication process. Nevertheless, advanced development of fiber manufacturing techniques can reduce this value to < 0.5 dB, ensuring a low loss over a broad communication range (1.3 μm to 1.7 μm).

Note that in this project, the length of nanostructure-enhanced fibers is limited to several meters. Hence, transmission loss and any spectral features caused by the fiber substrate can be neglected (e.g., the lineshape of a bare SMF-28 fiber is regarded as flat in single mode regime).

Now we focus on the propagation constant β_j. The mode remains guided provided that β_j satisfies the condition $n_{co}k_0 > \beta_j > n_{cl}k_0$. Here, we introduce a key dimensionless fiber parameter V, which is given by [119]

$$V = k_0 \cdot a \cdot NA_{fiber} = k_0 \cdot a \cdot n_{co} \cdot (2\Delta)^{1/2} = k_0 \cdot a \cdot n_{co} \cdot \sin\theta_c \tag{2.29}$$

where $\Delta = (n_{co}^2 - n_{cl}^2)/2n_{co}^2 = sin^2\theta_c/2$ is the fiber profile height parameter.

To analyze the fiber modes, two model parameters U_j and W_j for the core and cladding are given as

$$U_j = a(k_0^2 n_{co}^2 - \beta_j^2)^{1/2} \tag{2.30a}$$

$$W_j = a(\beta_j^2 - k_0^2 n_{cl}^2)^{1/2} \tag{2.30b}$$

where the wave-guide parameter (V) and modal parameters (U_j and W_j) are connected by

$$V^2 = U_j^2 + W_j^2 \tag{2.31}$$

The eigenvalue equation of HE_{vm} mode and EH_{vm} mode for the step-index fiber can be expressed as [2]

$$\left\{\frac{J_v'(U)}{UJ_v(U)} + \frac{K_v'(W)}{WK_v(W)}\right\}\left\{\frac{J_v'(U)}{UJ_v(U)} + \frac{n_{cl}^2}{n_{co}^2}\frac{K_v'(W)}{WK_v(W)}\right\} = \left(\frac{v\beta}{kn_{co}}\right)^2\left(\frac{V}{UW}\right)^4 \tag{2.32}$$

where $J_v(U)$ is the Bessel functions of the first kind (v denotes the function order) and $K_v(W)$ is the modified Bessel functions of the second kind. Note that each mode is labelled by two subscripts. The subscript v denotes mode order, and m is the m^{th} root of the eigenvalue equation.

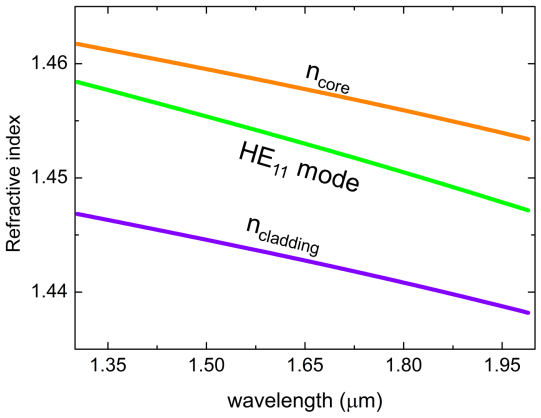

FIGURE 2.10
Dispersion relation of a step-index fiber. The effective index of fundamental HE_{11} mode (green curve) is obtained from analytical data using Eq. 2.32.

The measured HE_{11} mode image is displayed in Fig. 2.9 (c). The intensity distribution of HE_{11} mode can be approximated by a Gaussian function (i.e., $E \propto exp(-x^2/w^2)$) [119]. In fact, the mode section is larger than actual core

section. For instance, the mode diameter of an SMF-28 is about 10.4 μm at 1550 nm, while the core diameter is approximately 8.2 μm [22].

The dispersion of fundamental mode for SMF-28 in the wavelength range from 1.35 μm to 2.0 μm is plotted in Fig. 2.10, obtained by solving eigenvalue equation (Eq. 2.32). Here n_{co} and n_{cl} are fitted by Sellmeier equation to imitate the SIF arrangement. The effective index (green curve) of the HE_{11} mode is distributed between n_{co} and n_{cl} and can thus be guided in this fiber geometry.

2.3.2 Advancements in fiber optics

Recent developments (such as rare-earth-doped fibers [125, 126], polarization maintaining fibers [10] and microstructured fibers [6, 127]) dramatically enrich fiber types and expand fiber applications for endoscopy [128], remote sensing [121], lightening [129], to name just a few. Among these innovations, photonic crystal fibers (PCFs) [5, 6] are regarded as having initiated renewed interest in optical fibers studies. By applying a periodic array of microscopic air holes in a cladding, a PCF can guide light, relying on the modified total internal reflection. Compared to the well-developed SIF, a major benefit of PCF is the considerable design freedom to achieve a variety of particular properties (e.g., a high nonlinear effect and controllable dispersion characteristics).

More recently, a new direction of fiber studies has emerged, which is to add more and more functionality into the fiber. With the integration of materials such as metals, semiconductors, and metamaterials, the concept of hybrid fibers [130] has drawn increasing attention and has become an innovative platform for studies on light-matter interactions. Based on this concept, a wide range of fundamental research as well as practical applications have been conducted and achieved, e.g., monolithic fiber probes [34] and nano-objective in-fiber tracking [131].

2.4 Studies methods

In the last section, we present the approaches used to analyze optical properties (mainly the optical spectral response) of nanoscale functional structures. As generally summarized in Fig. 2.11, a set of methods is illustrated from the aspects of theoretical methods and experimental characterizations. Here,

we briefly review the approaches specifically used for probing nanostructure spectral behaviour.

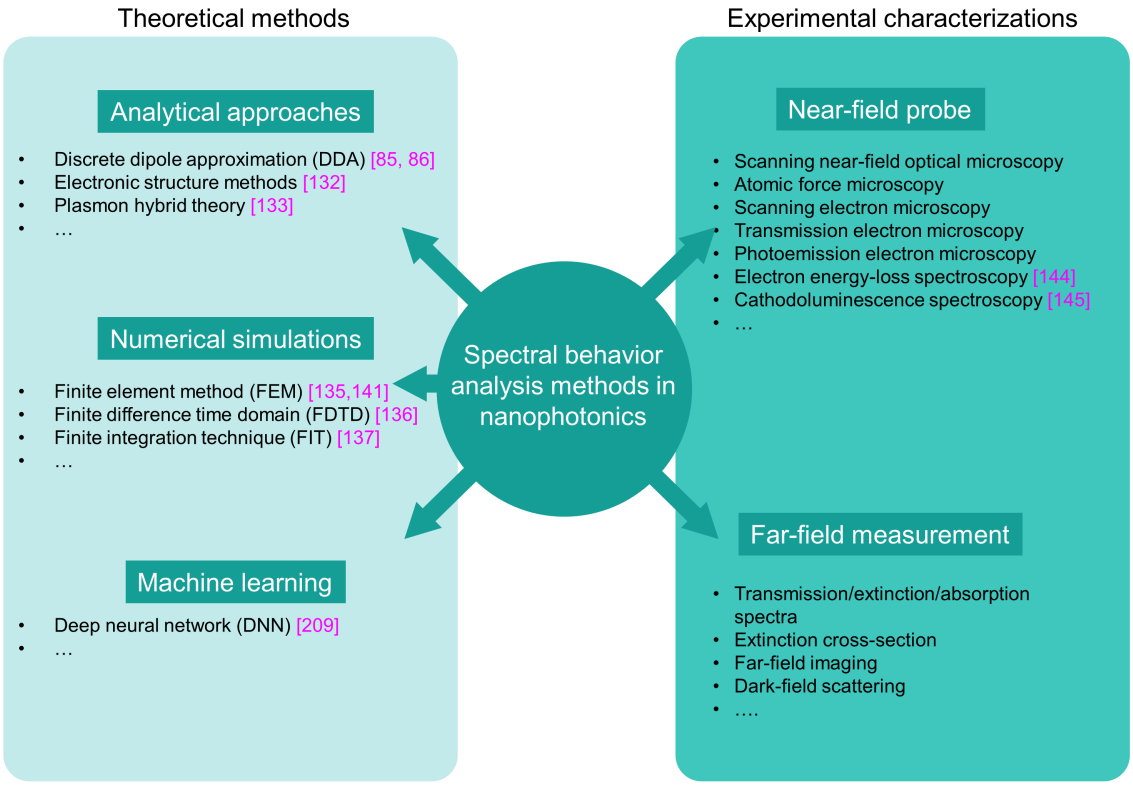

FIGURE 2.11
Commonly used methods in nanophotonics to study the optical spectral response from theoretical and experimental perspectives. In this study, we employ finite element method numerical simulations to design appropriate nanostructures and characterize nanostructure-enhanced fibers through experimental far-field transmission/extinction spectra.

Theoretical methods

- Analytical models

The cornerstone of artificial nanoantennas is metallic nanosized particles. For the analytically modelling of metallic nanoparticles, we refer readers these reviews [85, 86] for more detailed discussions.

To understand the complex properties of nanoantennas, a set of theoretical analysis methods (e.g., electronic structure method [132] to imitate electrical network) have been proposed. Among these approaches, plasmon hybrid theory [133] is one of the most widely used models and can be used to investigate the nature of coupled nanostructure system. In chapter 3, we will

employ plasmon hybrid theory to inspect optical properties of nanotrimers [134].

- Numerical simulations

Numerical simulation software relies on solving Maxwell'S equations by analysis technique such as finite-element-method (FEM) or finite-difference-time-domain (FDTD). Almost any arbitrary nanostucture can be modelled by appropriately configurating the geometric distributions, boundary conditions, and excitation. Currently, there are several commercial available 2D and/or 3D software programs (e.g., COMSOL Multiphysics [135], Lumerical FDTD Solutions [136] and CST Studio Suite [137]). Alternatively, some open-source tools (such as Meep [138], MNPBEM Toolbox [139], and DDSCAT [140]) can be considered for electromagnetics simulations.

In this work, we use FEM-based numerical simulations (COMSOL Multiphysics) to design nanostructures for usage with SMF-28. The working mechanism of the FEM is to solve complex partial differential equations [141]. Instead of obtaining accurate solutions, this method aims to approximate values of these functions. The FEM has been intensively employed to analyze scientific problems and engineering applications. Currently, the FEM is a dominating technique for solving solid-mechanics problems, and most computer-aided design software integrates this method for mechanical performance evaluations. A simulation example is demonstrated in chapter 3 (Fig. 3.4).

Experimental methods

- Near-field probing

Mode mapping is an effective method to visualize electromagnetic field distributions. To 'see' resonance patterns, two-photon induced luminescence (TPL) [142] or two-photon excited photoluminescence (TPIP) [143] imaging can be used. These mode-mapping techniques require high-resolution microscopes, such as scanning electron microscope (SEM) or scanning near-field optical microscope (SNOM). Other advanced spectroscopic techniques (e.g., electron energy loss spectroscopy [144] and cathodoluminescence spectroscopy [145]) can also be employed for near-field imaging of nanoantennas.

- Far-field measurements

Far-field spectrum characterization is perhaps the most straightforward method to connect theoretical predictions to experimental results. These

measurements include, but are not limit to, the transmission (T), extinction ($1 - T$), scattering, absorptance, etc. Other alternative measurements, such as extinction cross-section and scattering efficiency, can be classified in this category.

Here, we mainly employ far-field spectral measurements to characterize on-demand nanostructures and compare them with simulation results. The home-built optical setup (see the example in chapter 3, Fig. 3.2 (b)) allows us to obtain desired optical spectra over a broad wavelength range. With the help of additional components (e.g., waveplates and high-definition cameras), more advanced measurements (such as mode imaging) can be performed.

2.5 Chapter summary

In this chapter, we briefly introduce the fundamentals of plasmonics as well as fiber optics. Starting from Maxwell's equations, the dielectric functions of gold and silver are shown. The focus of this chapter is LSPRs supported by metallic nanoparticles. We illustrate the LSPR-related physical background, working principle, and spectral behavior through examples of gold nanodots. Furthermore, Fano resonance is generally introduced, which can modify the spectral lineshape to a highly asymmetric curve.

Additionally, the basics of optical fibers are presented in detail. We show a quasi-analytic model of step-index fibers together with dispersion relations. The measured HE_{11} mode image of an SMF-28 fiber exhibits a Gaussian-like beam profile. Finally, we concisely state the current research approach for analyzing nanostructures from the aspects of theoretical methods and experimental characterizations.

By illustrating the fundamental knowledge and study methods, we hope that readers can grasp the basic principles behind this project and thus gain a better understanding of the following sections of this thesis.

Chapter 3

Nanostructures designed for fiber applications

As discussed in chapter 2, intensive investigations on light-matter interactions at the nanoscale have revolutionized the field of nanooptics. These functional nanostructures are commonly fabricated on planar substrates, such as silica wafers and polydimethylsiloxane (PDMS). However, such planar substrates are not ideal for many situations requiring a flexible and remote delivery platform (e.g., remote sensing and in vivo endoscopy). Hence, patterning specially designed nanostructure at the end face of a flexible probe (i.e., optical fibers) would particularly benefit the fields of bioanalytics and medicine.

As the first step towards fiber-integrated plasmonic devices, designing specific types of nanostructures is a solid foundation. In this chapter, we illustrate the design and optimization procedures of metallic nanostructures for usage with fibers. As a conclusion, a trimer array is eventually determined to be patterned on a fiber facet based on analytical mode analysis, FEM-based numerical simulations, and experimental measurements.

This chapter is organized as follows. First, we compare the benefits and shortcomings of two types of substrates: optical fibers and flat silica glass. We propose the required optical responses of nanostructures (e.g., spectral lineshape) for usage with SMF-28. Second, through theoretical analysis and experimental measurements, we examine the optical properties of a gold dot array to determine if the spectral features can be shifted to the IR regime (the single mode regime of an SMF-28 fiber). Finally, we deeply analyze the optical response of a densely packed trimer array by modifying the unit cell arrangement within its distribution.

One of the particular striking effects of the trimer array is that it can support electric and magnetic Fano resonances, which arise from the destructive interference of a monomer-like mode and a dimer-like mode. Together with

the strong polarization dependence, these spectral features make the trimer array a potential candidate for patterning on fiber facets.

3.1 Benefits and challenges of fiber substrates

Initially, we would like to generally discuss the substrates used in functional nanostructure studies and why we try to transfer these nanostructures from flat substrates to fiber facets.

3.1.1 Planar substrate in plasmonics research

Perhaps the most commonly used substrate in photonics research is the silica wafer. This flat transparent substrate is compatible with current nanoengineering devices (e.g., lithography machines), and the stable chemical properties prevent it from interacting with well-defined nanostructures.

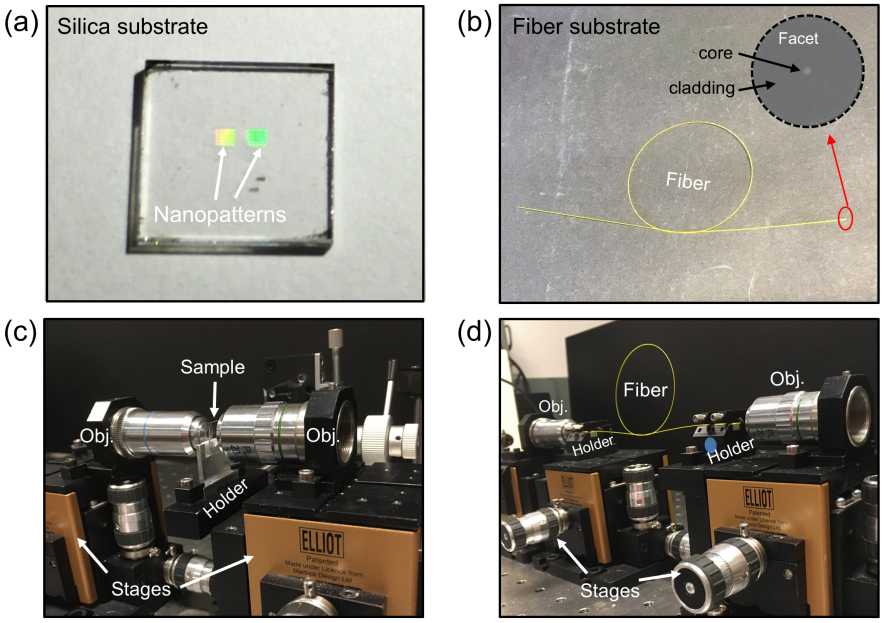

FIGURE 3.1
Comparison of a flat silica substrate and an optical fiber substrate. (a) Overview of a square-shaped silica substrate patterned with nanostructures. (b) A curved optical fiber (yellow coating). The top SEM image shows the facet of this SMF-28 fiber. (c) and (d) Typical experimental configurations for a flat substrate and an optical fiber, respectively.

One example of a silica substrate is shown in Fig. 3.1. (a), where gold nanostructures are patterned on its surface. The colors at the center of the

plate, which are caused by plasmonic resonances, indicate the nanopattern sites. Image (c) of Fig. 3.1 demonstrates the experimental configuration for optical spectrum characterization. Normally, the sample is fixed on a 3-axis stage (to finely control the sample position) and further placed between two optical objectives/lenses. Using high-resolution cameras (see the setup in Fig. 3.2 (b)), the nanoantennas and beam spots can be clearly observed.

For optical measurements, the procedures are straightforward. For instance, the transmitted spectrum (I, the beam on the nanostructure) and the reference spectrum (I_0, the beam on the bare substrate) can be separately recorded to obtain the transmission (defined as I/I_0). Here, the data errors caused by light coupling to substrates can be eliminated by ensuring identical experimental arrangements. During two spectra measurements (I and I_0), only the relative position of the silica substrate is slightly altered by using the 3-dimensional stage (see Fig. 3.1 (c)).

3.1.2 Fiber matters

Benefits:

In comparison to the planar arrangement, an optical fiber provides additional advantages as a substrate. It allows very precise control over the excitation conditions (in terms of the propagation constant, spatial mode pattern and polarization), i.e., the optical mode reaching the nanostructures, which is not a typical case for free beam excitation.

An optical fiber is also an ideal platform to deliver light on demand. Manipulating light propagation in free space requires additional components (e.g., mirrors) to reflect/diffract the beam at certain positions. Adjustment of the light path and alignment of these components takes tremendous effects. As a flexible waveguide, an optical fiber is a 'short-cut' tool for transmitting beams without supplemental assistance from bulky mirrors.

The fiber geometry (small cross-section) and the light weight are particularly helpful for space-constrained situations such as surgical operations [146] and spaceships [147]. In addition, an optical fiber is a versatile platform for cross-disciplinary studies, including those on optofluidics [131], glassy materials [148], etc.

Challenges:

Owing to the extremely high aspect ratio, an optical fiber induces two major challenges from fabrication [149] (e.g., implementing nanostructures

on its facet) and characterization (e.g., experimental spectral measurements) aspects. The former problem will be in-depth illustrated in chapter 4 (using a homemade container designed for electron beam lithography [25]), and the latter will be further properly solved in chapter 5 (by measuring the transmission contrast to reduce fiber coupling errors).

Here, we would like to emphasize the unique geometry of the fiber substrate. Fig. 3.1 (b) and (d) shows a 50-cm-long SMF-28 fiber along with an SEM image of the cross-section (inserted graphic at the top right corner), demonstrating the fiber shape and experimental configuration. This special geometry of fibers produces a severe light coupling problem in experiments.

The small core section and low NA of fibers could cause massive technical problems, especially when guiding an incident beam into fibers. One major consequence is the varied light in-coupling conditions between a reference bare fiber (I_0) and a nanostructured fiber (I). In this case, the transmission spectral features of nanostructures can be completely covered by the data errors caused by light coupling to the fibers.

The experimental errors induced by the fiber substrate mainly originate from two aspects. One is random surface variations (e.g., micrometer scale grooves) on the fiber core (induced by mechanical striping and cleaving). Another is the optical path misalignment that arises when substituting fibers and adjusting optical components (e.g., objectives and 3D stages). From the experimental setup in Fig. 3.1 (d), we can clearly observe the fiber coupling difficulty. To reduce the influence of the fiber in-coupling problem, the experimental method and procedure need to be carefully considered.

Required profound spectral response as fiber platform

The transmission lineshape of a bare SMF-28 (meters long) is much flat (single mode range, from 1.3 μm onward) with an amplitude approaching to unity in the decibel scale. As for the functional fibers with applications in fields such as sensing, the typical lineshape features of the fibers (e.g., transmission dips) should exhibit a considerable amplitude (e.g., > 3 dB) with a relatively narrow width (e.g., < 300 nm). These characteristics make the dip 'visible' (easier to detect and capture).

Hence, the shallow plasmonic responses (percentage scale) on flat substrates are not ideal for fiber application (dB scale). The spectral variations of nanostructures may not be detected on the fiber end face. This substrate substitution (from flat glass to fibers) requires a more intense optical response for experimental characterization.

Based on the above discussions, we propose **three design criteria** of nanostructures for usage with SMF-28.

- The optical spectral features (e.g., transmission dips) of nanostructures should be located in the **NIR regime**, roughly above 1300 nm, in order to match single mode regime of an SMF-28 fiber.
- The nanostructure should manifest strong and **sharp optical responses** (e.g., resonance amplitude > 30%, FWHM < 200 nm) even though the working area is confined to about 10×10 μm^2 (SMF-28 core section).
- Spectral **polarization dependence** is preferred. Here, polarization dependence denotes that different polarization of an incident beam could lead to different spectral features of the nanostructures. Therefore, measurement of relative spectral characteristics (instead of the transmission spectrum) can be conducted on a nanostructured fiber by merely changing the polarization. In this case, the perturbation caused by fiber coupling can be reduced as much as possible compared to reference fiber replacement.

3.2 Nanodisk spectral evolution: shifting resonance to the NIR regime

3.2.1 Theoretical model analysis

Now, we examine the first design principle - the possibility of shifting plasmonic resonance to the IR wavelength. As discussed in chapter 2, one of the key nanoantennas used in the project is the gold nanodisk. A sketch describing its geometry is shown in Fig. 3.2 (a). Here, D stands for the disk diameter, and H represents the disk height. We first address this resonance shift issue using an analytical model [150] and then carry out experiments to verify the theoretical model.

Under the assumption of a resonance spheroid in a homogeneous medium (vacuum), the polarizability ($\alpha(\omega)$, discussed in chapter 2) of an oblate spheroid in the quasistatic limit can be written as [150]:

$$\alpha(\omega) = \frac{4\pi a^2 b}{3} \frac{\epsilon(\omega) - 1}{1 + L \cdot [\epsilon(\omega) - 1]} \tag{3.1}$$

where a and b are the length of long and short axis of the spheroid, respectively, and L corresponds to the geometric factor of this spheroid. Using the dielectric function of metals in the form of Drude $\epsilon(\omega) = 1 - \omega_p^2/\omega(\omega + i\gamma)$ (ω_p is the plasmon frequency of the metal and γ is the damping term, more discussions in chapter 2), the polarizability of a spheroid becomes

$$\alpha(\omega) = \frac{4\pi a^2 b}{3} \times \frac{\omega_p^2}{L\omega_p^2 - \omega^2 - i\omega\gamma} \tag{3.2}$$

The the general form of modified long wavelength approximation (MLWA) formalism is given as (where c is the light speed constant)

$$\alpha(\omega)_{MLWA} = \frac{\alpha(\omega)}{1 - \frac{\omega^2}{4\pi c^2 a}\alpha(\omega) - i\frac{\omega^3}{6\pi c^3}\alpha(\omega)} \tag{3.3}$$

Combining Eq. 3.2 and Eq. 3.3, we obtain following equation:

$$\alpha(\omega)_{MLWA} = \frac{4\pi a^2 b}{3} \times \frac{\omega_p^2}{\left[L\omega_p^2 - \omega^2\left(1 + \frac{\omega_p^2}{3c^2}ab\right)\right] - i\omega\left(\gamma + \frac{2\omega_p^2\omega^2}{9c^3}a^2 b\right)} \tag{3.4}$$

Now we focus on the correction of plasmonic resonance frequency ω_{LSP} in the large particle assumption, which is indicated by the pole of the real part of Eq. 3.4.

$${\omega_{LSP}}^2 = L\omega_p^2/(\frac{ab\omega_p^2}{3c^2}) = L3c^2/ab \tag{3.5}$$

Translating this general equation to nanodot used in following experiments, we can define $a = D/2$ and $b = H/2$. The geometry factor L can be approximated as $L \approx (\pi/4) \times (H/D)$, and resonance wavelength $\lambda_{LSP}(\mu m) \approx 1.24/\omega_{LSP}(eV)$. Therefore, we obtain the following linear relationship: $\lambda_{LSP} \propto D$. This strongly supports the first design principle of shifting resonance features to the IR regime.

3.2.2 Experimental verification

Now, we can examine this formula (Eq. 3.5) from an experimental perspective. Before any optical tests, the first step is to acquire these nanostructures. Here, a concise fabrication process [134, 151, 152] for metallic nanodisk arrays is presented:

The sample fabrication starts with a fused silica chip (10×10 mm^2, 1 mm thick, see Fig. 3.1 (a)). Applying Caro's acid (peroxymonosulfuric acid) and

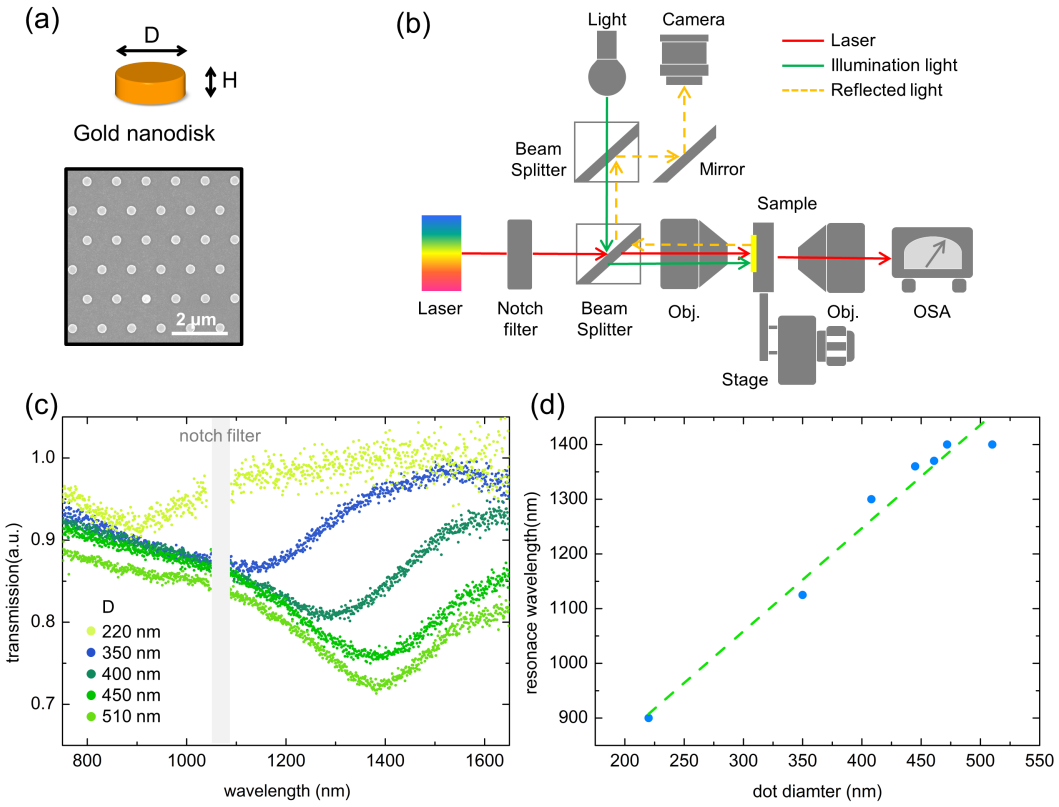

FIGURE 3.2
Gold nanodisk spectral behavior. (a) Nanodisk geometry and corresponding SEM image. (b) Experimental setup. (c) Optical transmission spectra of nanodisks with increasing diameter. (d) Resonance spectral shift (blue dots). The dashed green line is the linear fit of this spectral shift.

oxygen-plasma cleaning, the surface of the substrate can be properly cleaned. Afterwards, a 3-nm-thick titanium film is vapor deposited on this chip surface as an adhesive layer. Then, a 40-nm-thick gold layer (Roth&Rau Microsys 600) together with 130-nm-thick negative e-beam resist (micro resist technology GmbH) is coated on the titanium film.

The vital step is to pattern the nanodot array on the resist layer by electron beam lithography (Vistec 350 OS). Equipped with the character projection technique, the lithography machine allows fast quasi-parallel exposure of nanopatterns on large areas. Here, the nanostructure size (dot diameter from 200 nm to 510 nm) is finely tuned by the electron dose. Further development of the resist is conducted with the AZ MIF-736 developer. The next step is to etch the nanodot array into the gold film using Ar+ ion beam etching (IBE, tool: Multiplas II from 4-TEC).

After the key step of e-beam lithography, the residues are wet chemically

removed, followed by oxygen plasma cleaning (50 W, 1 min). Finally, a 10 nm alumina film is deposited on the entire chip surface using an atomic layer deposition process (plasma enhanced ALD, tool: "Oxford Opal"). This alumina film serves as a mechanical protection layer for the following optical measurements.

Each fabricated nanodot array has a size of approximately $100 \times 100\ \mu m^2$, which completely covers the beam spot of the $20\times$ objective used in the optical experiment. In Fig. 3.2 (a), we show an SEM image of one sample (disk diameter: 510 nm). The gold nanodisks are distributed in a hexagonal lattice where the pitch is chosen to be 1.7 μm, which is sufficiently large to reduce the diffractive dot-to-dot coupling.

Once these nanostructures are created, the corresponding optical characterization can be carried out. Fig. 3.2 (b) depicts the experimental setup for transmission/extinction spectrum measurements. The nanodisk sample is placed on a two-axis stage with normal incident light from a supercontinuum laser (NKT Photonics SuperK Compact) covering a wavelength range from the visible to the infrared regime. A notch filter (Thorlabs Inc.) working at 1064 nm is used to eliminate the laser source pump wavelength. The lower beam splitter (Thorlabs Inc.) couples illumination light (660 nm LED) to the sample and is additionally used for camera imaging. Note that this beam splitter needs to be removed when recording spectra. Two $20\times$ objectives (Olympus Corp.) are employed to obtain a focused beam with a spot diameter of approximately 10 μm. The transmitted light is recorded by the optical spectrum analyzer (Instrument Systems SP330-134). The transmission curve is acquired based on the power ratio of two spectra, with one beam on the nanostructures and the other beam passing through a bare silica substrate. A real-time spectral measurement configuration is shown in Fig. 3.1. (c).

For resonance spectral behavior studies, five types of nanodisks are made by gradually increasing their diameter from 220 nm to 350 nm, 400 nm, 450 nm and 510 nm. Note that the dot height (H) is fixed at 40 nm based on previous fabrication experience. The measured transmission data are presented in Fig. 3.2 (c).

Generally, all the nanodot spectra exhibit symmetric lineshapes, and the resonance wavelength (transmission dip) shifts from approximately 850 nm to 1400 nm as the dot diameter increases. We extract the resonance wavelength of each curve and plot these data (blue dots) in Fig. 3.2 (d). Clearly, the spectral redshift induced by increasing the dot diameter is well fitted by a linear function (green dashed line, coefficient of determination $R^2 = 96.4\%$).

Based on the theoretical model calculation and experimental observations, shifting the resonance features of gold nanodots to the telecommunication band (1.3 μm to 1.6 μm) is feasible, which can be realized by properly modifying the nanoparticle geometry. However, the transmission dips of these nanodots are still too shallow to be used for fiber application. Compared to the typical fiber spectrum, the amplitude of the plasmonic resonance is less than 3 dB, while the FWHM is greater than 300 nm. This dip feature could be completely overlapped by the noise induced by the fiber coupling problem.

3.3 Symmetric trimer array with Fano resonances

3.3.1 Background studies

In the last section, we have achieved the first target of designing nanostructures for fiber applications. However, the spectrum of the sparsely distributed nanodot array is not the best candidate for further fiber-based experimental characterization due to its shallow features. As discussed in chapter 2, Fano resonance is an optical effect that generates narrow spectral features [45]. Hence, nanostructures that can support Fano resonance are ideal candidates for patterning on fiber facets. For the following discussions (section 3.3), most of the data have been published in the literature [134].

Generally, Fano resonances arise from the interference between a broadband bright mode and a spectrally sharp dark mode. This modal interaction dramatically changes the lineshape of the scattered light by introducing a narrow dip or peak into the extinction/scattering spectrum. To achieve this unique effect, numerous nanostructures, such as single split nanodots [153, 154], nanocavities [155], nanosphere dimers [156], dolmen-like nanostructures [155, 157], plasmonic clusters [158] and oligomers [159–161], have been employed.

Among all these nanostructures, trimers consisting of three close-packed nanoparticles exhibit a strong magnetic resonance, which was first experimentally demonstrated in 2010 [162]. Therefore, the trimer system represents a potential design for realizing Fano resonance, especially when the magnetic resonance is the dark mode. Since then, several studies [163–166] have tried to obtain this magnetic-based Fano resonance in trimers by the symmetry-breaking method.

For the majority of Fano resonances mentioned above, distributions of nanostructures in which the periodic constants are commensurate with the resonance wavelength have been avoided. In such dense configurations, lattice collective resonances [98, 99] (e.g., surface lattice resonances), originating from the diffractive coupling of localized plasmons, could strongly modify the optical properties, leading to complicated lineshapes.

The near-field interactions among neighboring elements are strong and further result in more sophisticated effects. For instance, Chen Yan *et al*. demonstrated how near-field coupling of unit cells can impact the optical response of dolmen-like Fano resonance arrays [157]. By varying the periodicity along the horizontal or vertical axis, the far-field response of the plasmonic system can evolve into a tight-binding regime [157]. However, these complex optical responses mediated by the diffractive coupling of adjacent resonance elements have not yet been widely discussed.

In this section, gold trimers consisting of three identical nanodisks are selected for observing electric and magnetic Fano resonances. As shown in Fig. 3.3 (a), a schematic of trimer arrays with relevant geometric parameters is presented in detail. In general, symmetric trimers, where the dot-to-dot gaps G_1 all have the same value, are distributed in a rectangular unit cell with two periodic constants Λ_x and Λ_y (the coordinates at the right corner). The value of the trimer height (thickness of gold film: 40 nm) is mostly based on preliminary fabrication experiences, where this thickness gave the best nanostructures.

For the specific samples used in the characterizations, the two pitches are chosen to be 1.1 μm, resulting in a square unit cell ($\Lambda_x = \Lambda_y$ = 1.1 μm). Note that only normal incident light with linear polarization along the x direction is considered for the excitation of the trimer electric and magnetic Fano resonances. In addition, we need to emphasize the tight distribution of the trimers, which distinguishes this research from previous reports [167–169]. Within the close-packed array, the coupling of neighboring unit cells cannot be neglected, which further leads to the strong hybridization of multiple effects, e.g., trimer-to-trimer interactions and lattice resonance. The SEM image below the sketch clearly demonstrates the compactness of the trimer array.

Now, we briefly introduce two main methods used for analyzing trimer properties (both are generally discussed in chapter 2). The first is plasmonic hybridization theory, and the second is numerical FEM simulations. First, the trimer resonance can be interpreted as the interference between a dipole and a quadrupole based on hybridization theory [133, 170]. As shown in Fig. 3.3

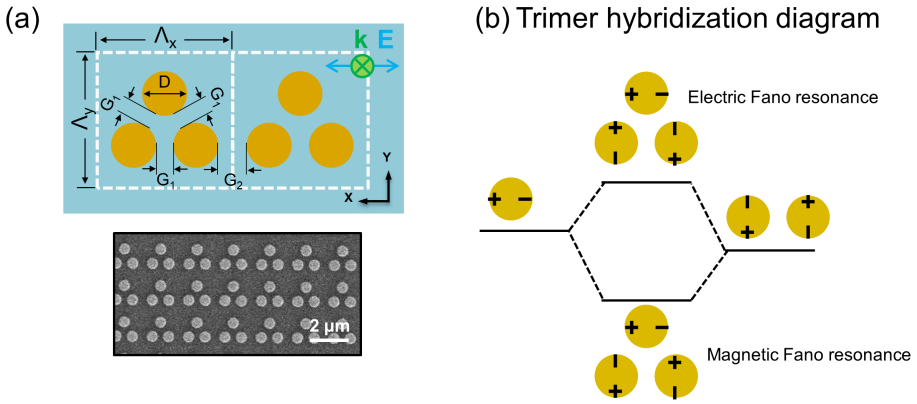

FIGURE 3.3
(a) Details of the symmetric trimer geometry (top) with corresponding SEM image (bottom). The symmetric trimer shares the same interparticle gap distances G_1 between all three nanodisks. For this example, the pitch Λ_x and Λ_y (distance to adjacent unit cell along x- and y- axis respectively) are both set at 1.1 μm. G_2 is the edge-to-edge distance of lower neighboring trimer dots. Here G_1 and G_2 are named as intra-trimer gap and inter-trimer gap, respectively for simplification. (b) Trimer hybridization diagram. The interaction of a dipole and a quadrupole results in two types of Fano resonances.

(b), a dipole resonance, supported by the upper dot of an isolated trimer, can interact with a quadrupolar-like resonance (two lower dots). Note that the quadrupole is often regarded as a dark mode, which can be triggered by near-field coupling instead of an external electromagnetic field. The interaction yields two different charge distributions, which resemble an electric Fano-like mode (top case) and a magnetic Fano-like mode (bottom case). Multiple studies have revealed that a wide range of nanostructures (e.g., dolmen-like nanobars) can support either electric [155, 157] or magnetic [164–166] Fano resonance, while there is still no strong experimental evidence of excitation of both types of Fano modes by the same nanostructure.

We use FEM-based simulation software to probe the details of the trimer array by analyzing the electromagnetic near-field distribution and transmission/extinction spectra. Here, we present a simulation example (Fig. 3.4) of a 3D trimer model using the RF (radio frequency) module [135] of COMSOL Multiphysics.

Based on the FEM, COMSOL Multiphysics is a powerful tool to study multiple interacting physical properties. For optical studies, electromagnetic

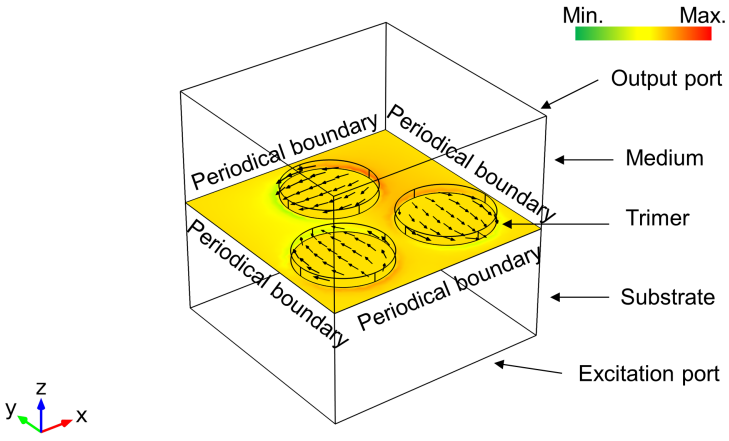

FIGURE 3.4
Simulation model of trimers in Fig. 3.3 (a). The RF module in Comsol Multiphysics is employed for 3D nanostructure simulations.

modules such as RF, wave optics and ray optics are commonly used. A typical simulation procedure includes building the geometry of the nanostructures, modifying properties of the materials and embedded environments, defining the physics (e.g., excitation and boundary conditions), meshing the system, defining details of the study (e.g., spectral analysis), and data post-processing (e.g., exporting E-field distributions).

For this specific demonstration of COMSOL Multiphysics, we arrange a trimer (D: 400 nm, H: 40 nm, G_1: 100 nm, pitch: 1100 nm) on the surface of a substrate. Based on actual experimental configurations, the surrounding medium can be either air or an index-matched environment (using similar index liquids to approach the index of glass substrates). The heights of the medium and the substrate are set to 500 nm. For the purpose of imitating the real trimer distributions, periodical boundary conditions of the RF module are selected and applied to faces of this cube. Accordingly, periodic ports (consisting of excitation and output ports) are employed to obtain the transmission curve. Only the 0^{th} diffraction order is recorded by using the S-parameter (S_{21} for transmission and S_{11} for reflection). The permittivity of gold is taken from the experimental data of ref [56]. The permittivities of the medium and substrate in this example are fixed at 1.0 and 2.09, respectively, since there is only a slight variation of the refractive index in the measured spectrum range.

To obtain high simulation accuracy, the dots need to be finely meshed. Here, the maximum mesh value is 5 nm. The 'parameter sweep' function

is used for the spectrum simulation, covering a range from 500 nm to 2100 nm (depending on the actual demands). In this specific example (Fig. 3.4), the electromagnetic field distribution of the trimer lattice at a wavelength of 1480 nm shows that the two lower dots resonate in oppose directions (i.e., magnetic-based Fano resonance).

3.3.2 Trimers optical response with increasing dot diameter

As a first step, the spectral distribution of the transmission of different types of symmetric trimers is measured with polarization resolution and compared to numerical simulations. Generally, the inter- and intra-trimer coupling strength of the investigated trimer arrays can be gradually increased by modifying the geometric parameters D, G_1 and G_2. Specifically, the diameter of the trimer dots varies from 200 nm to 250 nm, 300 nm, 350 nm, 375 nm and 425 nm, whereas the center-to-center distance between two dots is fixed at 500 nm. As the diameter of the dots increases, the intra-trimer gap G_1 and inter-trimer gap G_2 decrease to 300 nm, 250 nm, 200 nm, 150 nm, 125 nm, and 75 nm and to 400 nm, 350 nm, 250 nm, 225 nm, and 175 nm, respectively. In short, the trimer units change from an isolated particle status to a system of strongly coupled nanodisks.

The measured transmission spectra of symmetric trimers are shown in Fig. 3.5 (a), with corresponding SEM images in (b) (lower column numbers indicate the dot diameter of the trimers). Overall, the LSPR dips of various size trimers shift to longer wavelengths with increasing nanodisk diameter. This result can be intuitively understood based on the well-known relation between the plasmonic resonance spectral position and the size of nanoparticles (see discussions in chapter 2), which is also experimentally demonstrated in Fig. 3.2 (c).

However, the spectral lineshape of the trimers becomes increasingly asymmetric for larger disk sizes. For the first two cases (diameters of 200 and 250 nm), only one pronounced dip near 800 nm is observed. Here, the two spectra show a high similarity to that of single isolated nanodots in Fig. 3.2 (c). However, in the remaining four cases (diameters from 300 nm to 425 nm), two other dips are observed, which are close to 1100 nm and 1700 nm, respectively. Consequently, a narrow transmission maximum emerges at approximately 1600 nm.

Note that for the trimer with a diameter of 425 nm, there is another small

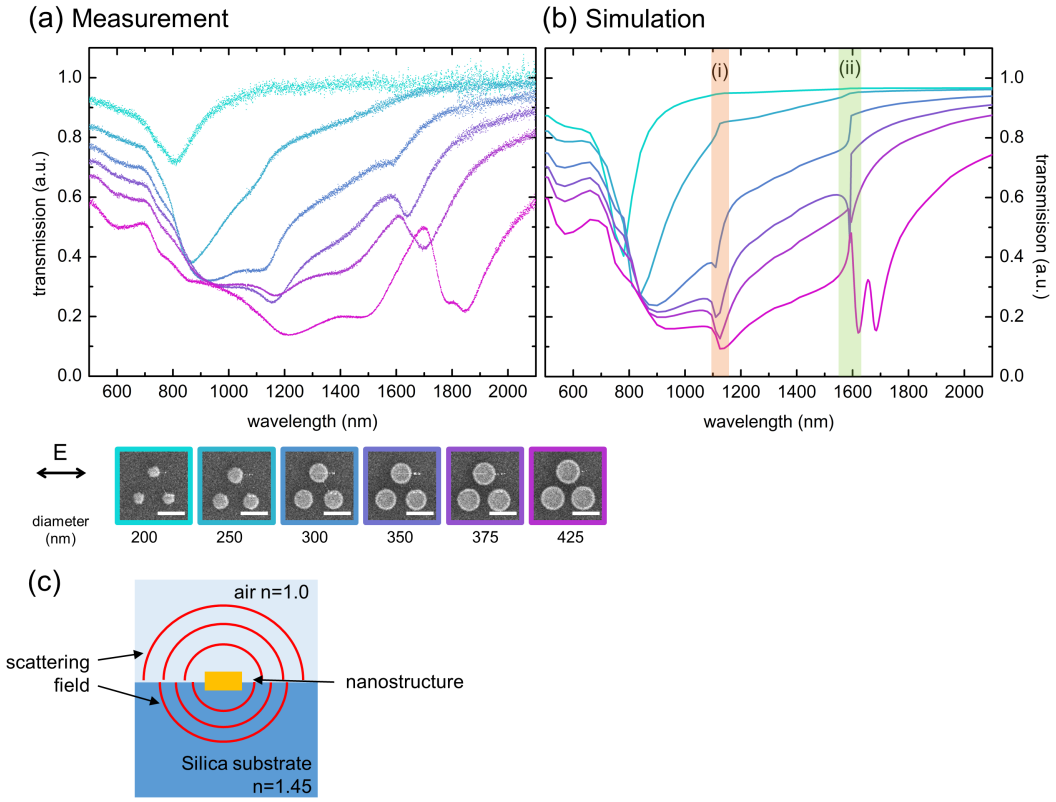

FIGURE 3.5
Measured transmission spectra of various symmetric trimers, with the corresponding geometry shown in the bottom SEM images. The polarization of incident light is parallel to the axis of the bottom two dots (x direction), indicated by the double headed arrow. Note that in all SEM images, the scale bar is 500 nm. The frame colors of SEM images correspond to the measured curve colors. (b) Corresponding simulated data. The positions and amplitudes of dips and peaks are generally in good agreement with the experimental curves. Here, (i) with a light orange background and (ii) with a light green background represent the diffraction orders in air and the substrate, respectively. (c) Illustration of different scattering fields induced by the air-silica environmental configuration.

transmission peak at approximately 1800 nm. Although this peak is less visible in air-substrate index-mismatched measurements, it becomes more pronounced in homogeneous surroundings (see Fig. 3.7 (a)). In depth studies on the formation of this peak are presented in sections 3.3.4 and 3.3.5.

Corresponding simulations (Fig. 3.5 (b)) by COMSOL Multiphysics match the experimental curves, where the peaks at approximately 1600 nm are fully reproduced. Comparing the two sets of spectra, the features (peaks and dips)

in the simulations are narrower and blueshifted compared to their experimental counterparts. This result partly occurs because of the higher losses in the real materials (i.e., larger imaginary part of the permittivity), which lead to broadened resonances. Moreover, the simulations assume a plane wave at normal incidence, while a focused Gaussian beam with a nonzero angular spectrum is used in the experiments.

Henceforth, we concentrate on the narrow spectral features of trimers (nanodot diameter > 300 nm) and analyze their formation based on simulation results. In the simulated spectra of Fig. 3.5 (b), these characteristic features are located at wavelengths of 1100 nm and 1600 nm (indicated by orange and green stripes), which can be attributed to the onset of the first diffraction order in air (n_{air} = 1.0, $\lambda_{air} = \Lambda \times n_{air}$ = 1100 nm) and in the substrate (n_{sub} = 1.45, $\lambda_{sub} = \Lambda \times n_{sub}$ = 1595 nm). Highlighted by the colored backgrounds (i) and (ii), the step-like spectral behavior originates from the power decrease of the transmitted 0^{th} order of light at the diffraction wavelengths. Here, the excitation of a trimer by the waves scattered from neighboring trimers is in phase with the external field, leading to a transmission minimum. This effect becomes stronger with larger disk diameter.

The experiments and simulations presented here involve different substrate and superstrate RIs (air-cladding and substrate in Fig. 3.5 (c)), with the result that the two different media result in two scattered waves with different wavelengths. The distribution of the scattered energy into two waves of different wavelengths yields weaker spectral features than the strong ones achieved in the case of a homogeneous environment. This result can be found in the next section (Fig. 3.7 (a)), where the measurement under the index-matched situation presents stronger spectral characteristics than the current results.

Based on the aforementioned discussions on Fig. 3.5, we find that the closely arranged trimer array meets the second nanostructure design requirement (narrow spectral features in the IR) better than sparse nanodot arrays (Fig. 3.2 (c)). In particular, for a trimer array with a dot diameter > 350 nm, these types of nanoantennas show narrow spectral features at approximately 1700 nm (i.e., the relative amplitude contrast of this dip > 20%, FWHM < 300 nm).

3.3.3 Spectral polarization dependence of trimers

We further inspect the trimers response under different polarization excitations. Here the transmission spectra of trimers (diameter: 400 nm, G_1: 100 nm, pitch: 1100 nm) are experimentally obtained by rotating the incident light polarization from 0° to 90°. The measured transmission spectra from 1400 nm to 2000 nm are shown in Fig. 3.6. The polarization angle is defined relative to the line connecting the centers of the lower two dots (i.e., the x-axis). In detail, the trimers are illuminated under the normal incident light with polarization angles of 0°, 15°, 30°, 45°, 60°, 75°, and 90°.

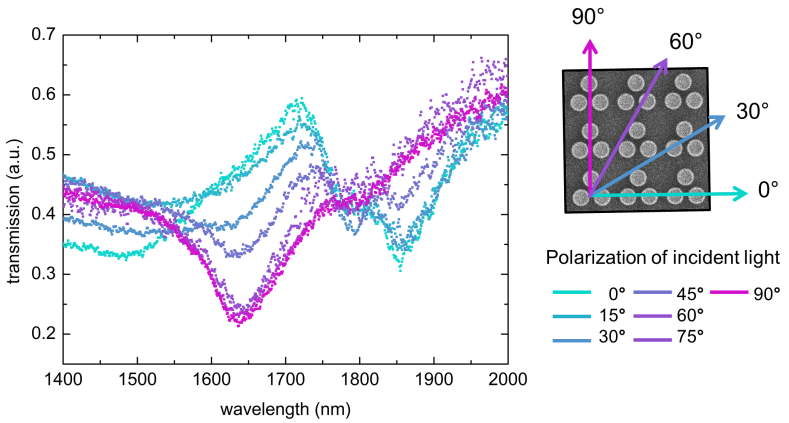

FIGURE 3.6
Transmission spectra of the trimer array with a nanodisk diameter of 400 nm for different input polarization angles (from 0° to 90° in steps of 15°). Remarkably, at approximately 1650 nm, the peak gradually changes from a peak to a pronounced dip. An illustration of different polarization directions with respect to the trimer array geometry is shown at the right. Note that all the measurements are carried out in air-silica RI configurations.

Intensive research [167–169] on trimers (isolated case or sparsely distributed) has illustrated that changes in the incident light polarization cannot induce any major spectral modification, while the spectra of the close-packed trimer array contradict these observations, as the spectra can be dramatically altered by changing the incident light polarization (see Fig. 3.6). We believe that this polarization dependence of the trimer array is caused by symmetry breaking, where the square distribution of unit cells breaks the geometric symmetry of trimers. For the isolated symmetric trimers, three identical nanodisks are situated at three vertices of an equilateral triangle. Obviously, the trimers have a six-fold symmetry regarding normal incident light polarization. Hence, rotating the excitation E-field by 60° should result in an identical

optical response where the spectral features match at the same wavelength. However, the square-shaped unit cell used here breaks this 60° symmetry of individual trimers. The trimer array is two-fold symmetric with two main axes (0° and 90°, corresponding to the x- and y-axes). All other polarization direction responses can be described by a superposition of the effects along the main axes.

We would like to conclude that the closely arranged trimer array is an ideal nanostructure for usage with fibers according to Fig. 3.5 and Fig. 3.6. For trimer arrays with a dot diameter > 400 nm distributed in square-shaped unit cells, this nanoantenna meets all three requirements proposed in section 3.1. Exhibiting narrow spectral features (i.e., relative dip amplitudes > 30%, FWHM < 300 nm) in the telecommunication band (e.g., a transmission dip at approximately 1600 nm), trimers in tight distributions (i.e., pitch of 1.1 μm) are more suitable for an SMF-28 fiber (the fiber core diameter is merely 8 μm). Here, we highlight the strong polarization dependence (Fig. 3.6), which is a valuable property for the subsequent characterization of nanotrimer-enhanced fibers (see chapter 5). In the following sections, we study the formation of two transmission peaks (at 1700 nm and 1800 nm, respectively, in Fig. 3.5 (a)) supported by the trimers with a dot diameter of 425 nm.

3.3.4 Electric and magnetic Fano resonances in a trimer array

Henceforth, all experimental characterization and numerical simulations are carried out in a homogeneous environment to achieve a higher signal-to-noise ratio. Please note that in the remaining parts, we present extinction spectra (obtained by 1-T), which are more commonly used in nanophotonics research.

We focus on the dipolar resonance range (approximately above 1600 nm) for the trimer geometry (D: 425 nm, H: 40 nm, G_1: 75 nm) with a fixed pitch (1100 nm, G_2: 175 nm). The extinction of the trimer array (Fig. 3.7 (a)) is obtained with the trimers immersed in an analytical liquid (RI = 1.45). A corresponding numerical calculation (Fig. 3.7 (b)) is also conducted for index-matched configurations by setting the medium index to 1.45. Fig. 3.7 (c) shows the simulated electric and magnetic field distribution within two cut planes together with the electric polarizations (arrows) at the central surface of each disk. In particular, the plots show the out-of-plane electric field component (E_z) in a plane 1 nm above the disks (z = 41 nm) and the normalized value of the magnetic field (|H| at z = 50 nm). The former indicates the

charge distribution at the disk surfaces, whereas the latter allows visualization of the out-of-plane magnetic moment.

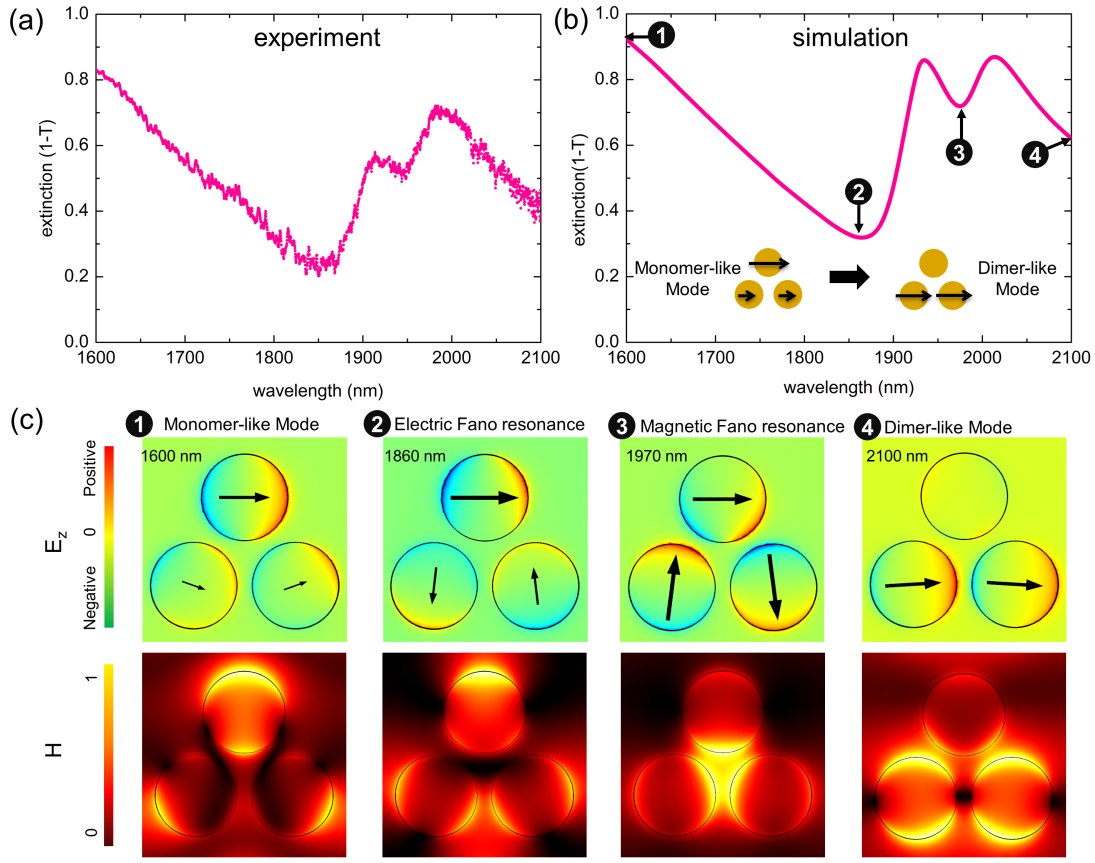

FIGURE 3.7
Experimental extinction spectrum (a) and numerical simulation (b) of the trimer array (dot diameter of 425 nm) with selected electromagnetic field distributions in (c). Polarization directions (arrows) and the out-of-plane (along the z-direction) E-field component E_z (colored contours, indicating the charge distribution) are shown in the upper row of (c) together with the normalized magnetic field distributions in the lower row. The number labels of (c) correspond to the wavelengths in (b).

Comparing the two extinction curves (Fig. 3.7 (a) and (b)), the experimental spectrum coincides very well with the numerical simulation, in which the two minima are both captured (one is near 1850 nm, and the other one is close to 1950 nm), even though the features in the simulation are slightly redshifted.

Generally, a transition from a monomer-like resonance pattern (case 1 in Fig. 3.7 (c)) to a dimer-like pattern (case 4 in Fig. 3.7 (c)) can be found for the trimer array when the wavelength increases from 1600 nm to 2100 nm. The former case exhibits a strong dipole moment supported by the upper

disk (the two lower dots show a relatively weak dipole moment) at 1600 nm, whereas the latter case exhibits a strong dimer-like resonance pattern, indicated by the in-phase oscillation of the two lower dots at 2100 nm. This transition process is schematically depicted in Fig. 3.7 (b).

Between these two wavelengths, the spectral lineshape becomes highly asymmetric. Two extinction minima (cases 2 and 3 in Fig. 3.7 (c)) are observed, corresponding to different Fano resonance modes. In particular, at the wavelength of 1860 nm, the polarization of the upper dot is parallel to the applied incident light polarization (along the x-axis), while the two lower dots are polarized mainly in the y-direction with opposite polarities. This polarization and charge distribution resemble a dolmen-like Fano pattern, which is widely discussed as the electric Fano resonance. In these references [155, 157], the dolmen-like Fano resonance is commonly supported by individual nanostructures, while the trimer-based electric Fano resonance here is generated in a close-packed nanostructure array.

It is of great interest to observe the loop-like polarization (named magnetic Fano resonance in Fig. 3.7 (c)) situated at the extinction dip near 1970 nm. In particular, the magnetic field (case 3 in Fig. 3.7 (c) bottom row) at this wavelength is highly confined within the inner section of the three dots, which cannot be found at the other three wavelengths. Numerous studies [164–166] refer to this specific pattern as a magnetic-based coil-type Fano resonance. Here, the bright mode, formed by the three individual dipole modes being in electric resonance, couples to the magnetic resonance, resulting in a circle-like polarization distribution. Therefore, the destructive interference of the bright electric mode and the dark magnetic mode results in an extinction dip.

Several reports have revealed that the excitation of this magnetic Fano resonance requires additional symmetry breaking (modifying the interparticle gaps [163] or geometry of trimer dots [164], etc.). This mode is assumed to be forbidden for a single equilateral trimer since the electric dipole and magnetic dipole modes belong to different symmetry groups and thus cannot interact. However, in the symmetric trimer array presented here, we experimentally observe magnetic Fano mode spectral features and mode profiles, which cannot be found in sparsely distributed trimers. This result indicates that the diffractive coupling of units may lead to magnetic-based Fano resonance generation. In the following sections, we will explore how trimer-to-trimer coupling can influence mode behavior.

To the best of our knowledge, the trimer array used here may represent

the first experimental demonstration of a nanostructure that supports both electric and magnetic Fano resonance. Although there are several reports claiming the so-called 'double Fano resonance' [171, 172], the dark modes in all of these systems are still electric resonances rather than magnetic modes. For example, Alp Artar *et al*. demonstrated directional double Fano resonance with a compact hetero-oligomer [171]. According to the charge distribution diagram, both dark modes still rely on the electric resonances (the polarizations in the nanostructures are in opposite directions) instead of the enhanced magnetic resonances in trimers.

3.3.5 Trimer optical response with modification of the unit cell

In this section, we study the adjacent unit coupling influence on the trimer spectra by altering the unit cell geometry. For the following numerical simulations, the trimer dot diameter (D), height (H) and intra-trimer gap (G_1) are fixed at 425 nm, 40 nm, and 75 nm, respectively. Again, by applying a homogeneous environment and periodic boundary conditions, simulated data are obtained, as presented in Fig. 3.8 and Fig. 3.9. For simplification, the horizontal and vertical lengths of the rectangular unit cell are named Λ_x and Λ_y, respectively.

We first inspect the trimer spectra and mode profiles by merely extending Λ_x from 1000 nm to 1600 nm (G_2 from 75 nm to 675 nm) while fixing Λ_y at 1100 nm. The simulated data are presented in Fig. 3.8 with a sketch showing how the unit cell is modified (left corner). Overall, two major modes, namely, a monomer-like mode (extinction minima, blue dashed line) and a dimer-like mode (extinction maxima, orange dashed line), can be found for all trimer geometric arrangements. In particular, the two modes almost remain at the same wavelength when $\Lambda_x > 1200$ nm (monomer mode: approximately 1900 nm, dimer mode: approximately 1950 nm). From case 3 to 7, the inter-trimer gap G_2 is greater than 275 nm, nearly four times larger than the intra-trimer gap G_1 (75 nm). For such large horizontal pitches, the diffractive trimer-to-trimer coupling should be weaker than the 'internal' dot-to-dot coupling. Hence, trimers behave like an individual element, and the interaction between the monomer mode and dimer mode is less pronounced.

Highlighted by the blue dashed line in Fig. 3.8 (a), a mode transition from the monomer-liker mode (cases 7 to 3) to the electric Fano mode (cases 2 and 1) is clearly observed at the same spectral feature (extinction dip) with

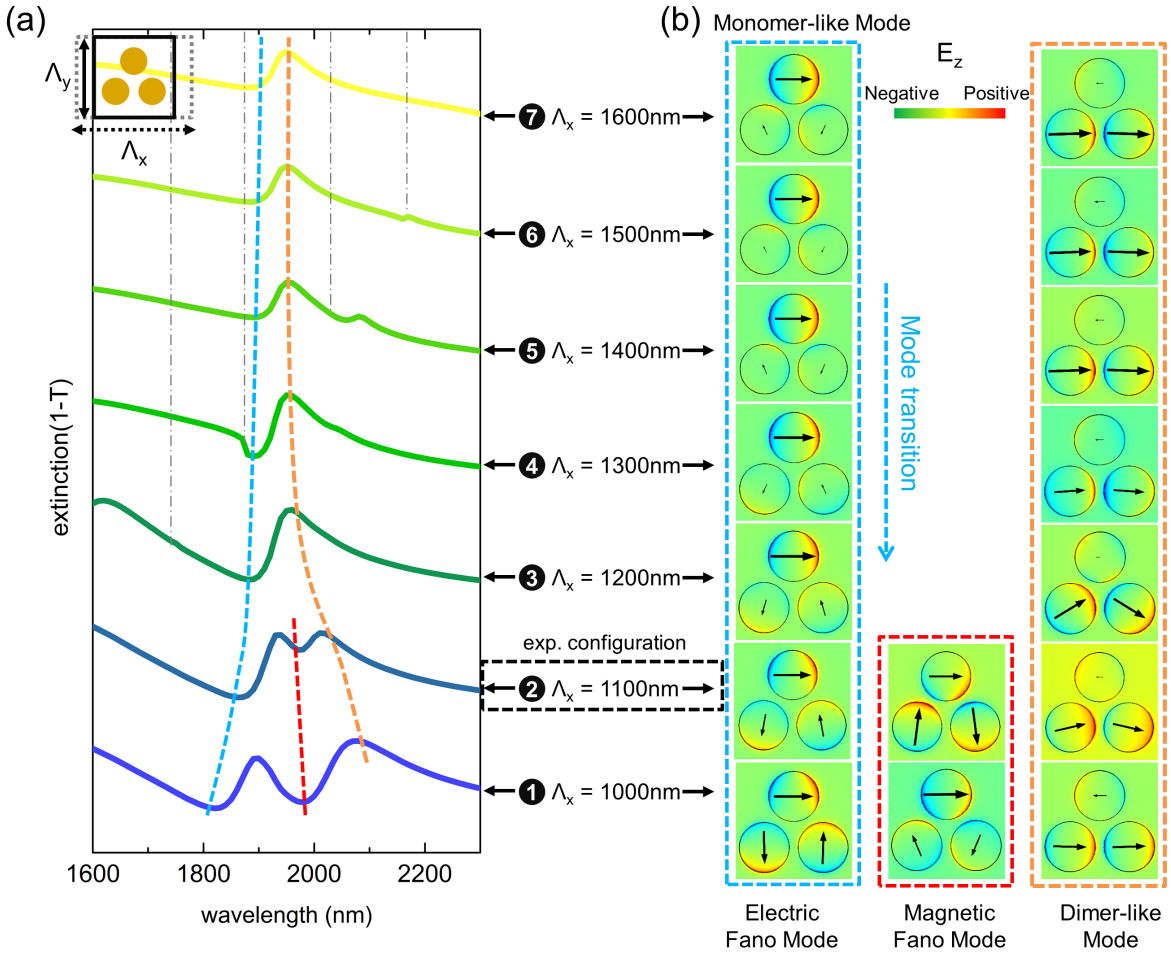

FIGURE 3.8

(a) Dependence of the extinction spectra of trimer arrays on the pitch along the horizontal direction (x-axis). The schematic in the top left corner illustrates how the unit cell is modified. The vertical pitch Λ_y is set to 1100 nm, and Λ_x varies from 1000 nm to 1600 nm. (b) Simulated resonance patterns at the selected wavelengths corresponding to the same color dashed lines in (a). The designated number and the value of Λ_x connect the spectral features and near-field patterns. Note that in the blue frame, a mode transition from the monomer-like pattern to the electric Fano resonance pattern is clearly observed with decreasing Λ_x. The vertical dashed-dotted gray lines indicate the onset of the $< 1, 0 >$ diffraction order. The experimental configuration of unit cells in case 2 is highlighted.

decreasing Λ_x. In the case of $\Lambda_x < 1100$ nm, the hybridization of the monomer mode and dimer mode becomes stronger due to improved adjacent coupling along the horizontal axis. Now, the value of G_2 (75 nm for case 1 and 175 nm for case 2) is comparable to that of G_1 (75 nm). The interaction of the two modes leads to an additional extinction dip, highlighted by the dashed red

line in Fig. 3.8 (a). The simulated mode profiles (red framed images in Fig. 3.8 (b)) correspond to the magnetic Fano resonance patterns where a loop-like polarization is generated within a trimer unit. Especially for the case of Λ_x = 1000 nm, the identical values of G_1 and G_2 (both 75 nm) denote an evenly distributed plasmonic chain formed by the bottom two dots. Here, the magnetic Fano mode becomes prominent, with a complete closed loop-like polarization, and the extinction minimum is most remarkable among all the spectra. It can be predicted that the coupling along the x-axis can be further improved by reducing G_2, and the magnetic Fano resonance should be consequently enhanced.

Now, let us consider vertical trimer coupling influences on the mode performance. Here, the trimer lattice is calculated as a rectangular cell in which G_1 and G_2 are assigned as 75 nm and 175 nm, respectively. By varying the pitch Λ_y, we obtain the set of extinction spectra shown in Fig. 3.9 (a), accompanied by the E-field distributions shown in (b). The evaluations of trimer spectra become more complicated and the spectra become highly asymmetric due to the additional strong modification of < 0, 1 > diffraction. Nevertheless, a dimer-like pattern (orange dashed line) can be detected in cases 1 to 6, and this feature shifts towards longer wavelengths with increasing Λ_y. For cases 2 to 5, the magnetic Fano resonance is represented by the extinction minimum along the red dashed curve in Fig. 3.9 (a). Inspecting the near-field patterns (red frame) in (b), the resonance of the two bottom dots becomes less visible while the top dot gradually exhibits strong resonance as Λ_y increases. Once the vertical pitch is > 1500 nm, the extinction becomes much flatter, and the magnetic Fano resonance cannot be observed anymore.

It is interesting to note that enhanced trimer-to-trimer couplings along different axes (x- or y-direction) lead to distinct optical responses in this close-packed array. For instance, the unit cell configuration of Λ_x = 1000 nm and Λ_y = 1100 nm results in a pronounced magnetic Fano mode (case 1, Fig. 3.9), while this mode is strongly suppressed for Λ_y = 1000 nm and Λ_x = 1100 nm (case 1, Fig. 3.10). This underlying mechanism remains unclear and should be further investigated.

Finally, we discuss the impact of the intra-trimer gap (G_1) and inter-trimer gap (G_2) on the trimer spectra under a square-shaped unit cell. The trimer geometry remains the same as in Fig. 3.8 and Fig. 3.9 (D: 425 nm, H: 40 nm). For convenience, we focus our study on the periodic constant (pitch) Λ instead of the inter-trimer gap G_2 ($\Lambda = 2\times D + G_1 + G_2$). In detail, the spectral distributions of the extinction for various pitches Λ between 1000

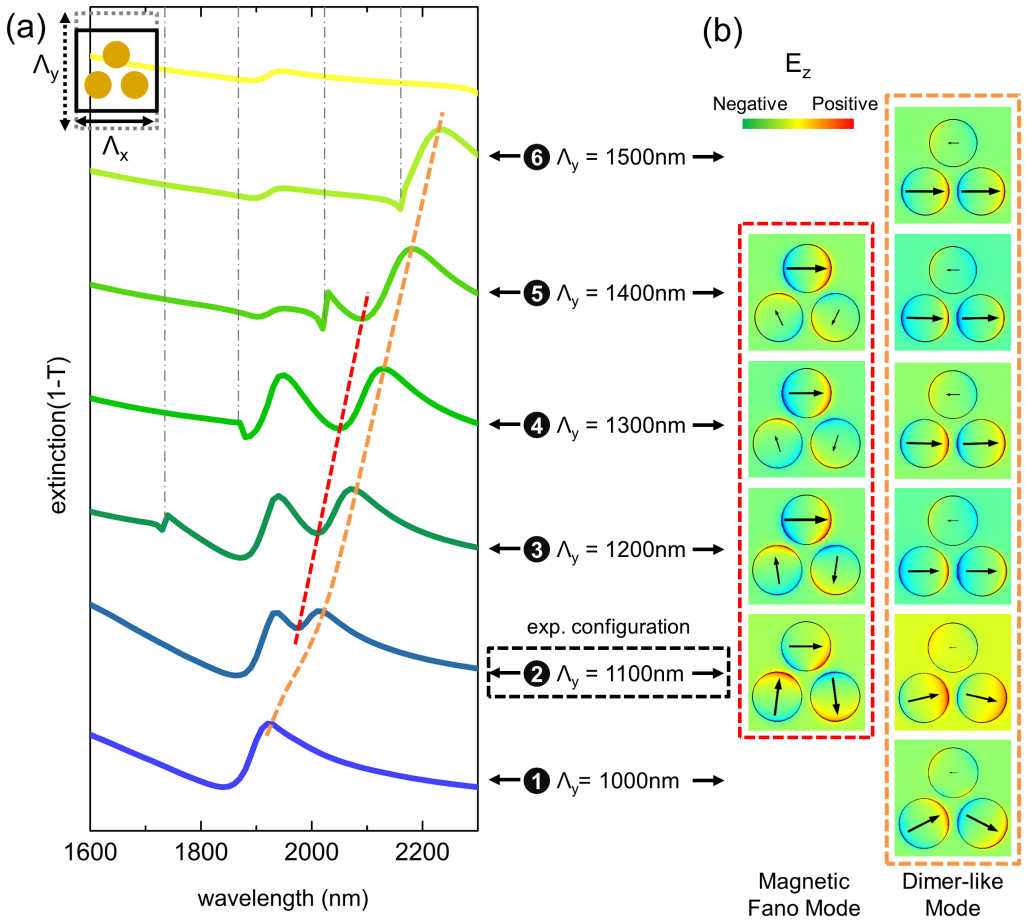

FIGURE 3.9

(a) Dependence of the extinction spectra on the pitch along the vertical direction (y-axis, schematic in the top left corner). Λ_y varies from 1000 nm to 1600 nm, while the horizontal pitch Λ_x is set at 1100 nm. (b) Corresponding simulated electric field patterns and polarizations at the wavelengths highlighted by the various dashed lines in (a). The designated number together with the horizontal pitch Λ_y connects the spectral features and near-field patterns. The dashed colored lines are guides to the eye showing the spectral shift of the respective feature. The vertical dashed-dotted gray lines indicate the onset of the $< 0, 1 >$ diffraction order for the respective pitch. The experimentally investigated configuration is highlighted by the framed box.

nm and 1700 nm at a step of 50 nm (G_2: 75 nm to 775 nm, G_1 is fixed at 75 nm) are presented in Fig. 3.10 (a). Fig. 3.10 (b) displays the extinction spectra obtained by modifying the intra-trimer gap G_1 from 12.5 nm to 137.5 nm (step size of 12.5 nm). Both calculations are carried out in the index-matched configuration under x-polarized incident light, and the white dashed line indicates the $< 1, 0 >$ diffraction order in this configuration.

Electric and magnetic Fano resonances can be manipulated by varying

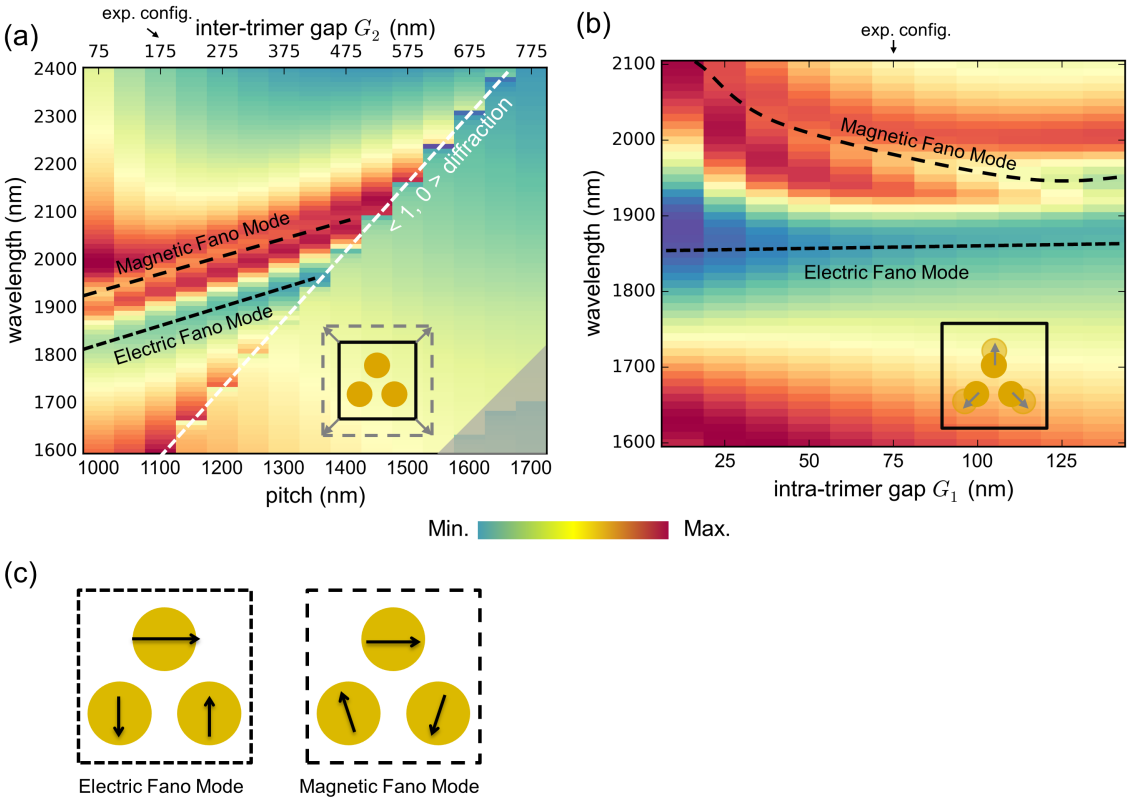

FIGURE 3.10

Trimer spectra behavior in the square-shaped unit cell. (a) Extinctions of trimer arrays as the pitch Λ increases from 1000 nm to 1700 nm. The white dashed line is the < 1, 0 > diffraction in the index-matched environment. The modification of the unit cell is schematically depicted at the right corner. More sophisticated lattice modes are greyed out. (b) Extinction spectra of trimer array with increasing intra-trimer gap (G_1) while Λ is fixed at 1100 nm. (c) Schematics of two types of Fano resonances. Two patterns are represented as short dashed and long dashed lines in (a) and (b).

the inter- and intra-trimer gaps. In Fig. 3.10 (a), two modes are located at the pitch range from 1000 nm to 1400 nm and are suppressed by the first diffraction order. Within this pitch range, the trimer-to-trimer coupling distance G_2 is gradually varied, whereas the trimer internal dot-to-dot interactions should remain the same (G_1 is fixed at 75 nm). Noticeably, both patterns move towards longer wavelengths, indicating that the mode behavior can be modified by external (inter-trimer) coupling, i.e., G_2 plays a more important role than G_1. Once the pitch is greater than 1400 nm, the extinctions only exhibit a step-like lineshape along the diffraction order, while the two types of Fano resonances cannot be detected anymore. More sophisticated lattice modes at the left corner are grayed out since they are beyond the scope of

this thesis.

Furthermore, let us consider a complex coupling configuration in which the intra-trimer gap G_1 and the inter-trimer gap G_2 are both adjusted. Fig. 3.10 (b) displays simulated extinctions by varying the intra-trimer gaps G_1 (from 12.5 nm to 137.5 nm) at a fixed pitch (Λ = 1100 nm). In this case gap G_2 is inevitably altered from 237.5 nm to 112.5 nm. Surprisingly, the central position of the electric Fano mode remains at approximately 1850 nm, while magnetic Fano pattern shifts from about 2100 nm to 1970 nm. This spectral blueshift with increased separation agrees with the discussion in ref. [162], which is attributed to the reduced capacitive couplings.

It can be summarized that the magnetic Fano resonance strongly relies on the neighboring unit cell coupling. In Fig. 3.10 (a), the Fano spectral feature is most evident at the pitch condition of 1000 nm, where G_2 reaches the minimum value of 75 nm (G_1 is always 75 nm). This amplitude enhancement of the Fano mode can also be observed in Fig. 3.10 (b) with decreasing G_2. In particular, at the minimum value of G_2, the trimer array is so closely packed that it cannot be divided into unit cells of individual trimers because G_2 is less than G_1 (G_2 of 112.5 nm and G_1 of 137.5 nm).

3.3.6 Summary of optical properties of trimer arrays

Now, we would like to present a conclusion about the impact of near-field coupling on the formation of magnetic Fano resonance based on the plasmon mode performance in Figs. 3.8, 3.9, and 3.10.

First, the distribution of trimers matters. According to the group theory analysis of trimer eigenmodes [163, 168, 173], the magnetic Fano resonance of the equilateral trimer cannot be excited by in-plane excitation since a nonzero net dipole moment requires additional symmetry breaking. However, in densely packed symmetric trimers, magnetic-based Fano resonance is generated. The excitation of magnetic resonance can still be attributed to the symmetry-breaking approach, which is induced by the geometry of the unit cell rather than the trimer itself. Here, the square-shaped unit cell breaks the six-fold symmetry of an individual trimer and changes the trimer array symmetry to two-fold symmetry. Hence, the interaction of magnetic and electric modes becomes active.

Second, this system symmetry breaking only works under certain conditions (e.g., geometric distribution, wavelength and incident light polarization). For instance, according to the square-shaped unit cell studied in Fig.

3.10 (a), the edge length should not exceed 1400 nm to trigger magnetic Fano resonance. Under such distribution configurations, the diffraction order position can be shifted to below the working wavelength, while the adjacent unit cell coupling will still be effective.

Finally, we would like to emphasize that the external trimer-to-trimer coupling plays a more important role in magnetic Fano resonance generation than the internal dot-to-dot interaction within a trimer unit. This phenomenon can be found in Fig. 3.8 (a) and Fig. 3.10 (b), where a complete loop-like polarization is gradually formed by decreasing the inter-trimer gap G_2.

3.4 Chapter summary

In this chapter, we have mainly studied the optical properties of a sparsely arranged gold nanodot array and close-packed gold trimer lattices using a theoretical model and numerical simulations as well as experimental characterizations to fulfill the proposed three design principles of nanostructures for fiber application.

Initially, a resonance spectral redshift is observed in both types of nanostructures with increasing nanoparticle diameter. In particular, a single nanodisk with diameter > 400 nm exhibits a transmission dip at the telecommunication band (Fig. 3.2). This phenomenon meets the first demand - to transfer the spectral features to the IR regime. Second, the asymmetric lineshape generated by the trimer lattice (Fig. 3.5) satisfies the second requirement, where a major narrow peak (at approximately 1700 nm) emerges within the broad transmission dip (from 700 nm to 2100 nm). The detailed investigations reveal that the close-packed trimer array can excite electric and magnetic Fano resonances owing to the near-field coupling (Figs. 3.7, 3.8, 3.9 and 3.10). Furthermore, the strong polarization dependency (Fig. 3.6) of the trimer spectra fulfills the third principle of nanostructure design. This spectral feature is of great help in identifying nanostructure-enhanced optical fibers (see the characterization in chapter 5).

Throughout the entire chapter, the principal goal is to obtain the desired optical response of nanostructures, in particular, narrow spectral features in the telecommunication band. The prediction of the optical spectrum is a time-consuming process that requires not only a good understanding of plasmonic fundamentals but also numerical modeling as well as hands-on

experimental ability. Recently, several references have demonstrated that artificial intelligence [174] can address these challenging tasks in nanophotonic imaging, design and characterization.

Chapter 4

Implementation of nanostructures on optical fiber facets

In this chapter, the nanofabrication techniques used for creating nanostructures on a fiber end face will be presented. In particular, fiber-substrate electron beam lithography (EBL) (typical length: tens of centimeters) is the manufacturing method used in this work, where we successfully employed EBL to produce nanostructure-modified fibers [25]. Here, we take the trimer array as a specific example to illustrate the fabrication process. The detailed discussions in chapter 3 reveal that a densely packed trimer array is an ideal candidate for fiber application due to its narrow spectral features in the IR regime and strong polarization dependence.

The commonly used nanoengineering methods were originally designed for wafer-based substrates. These approaches cannot be applied to an optical fiber in a straightforward way owing to the small cross-section of the fiber facet (diameter < 300 μm) and the extremely large aspect ratio. For instance, a typical 'problem' of lithography is the operating space of machines, which allows a maximum thickness of the substrate < 2 centimeters. This geometric confinement makes the fabrication of 2D nanostructures on optical fiber surfaces challenging [149]. One approach is to customize the fiber length (i.e., to cut fibers into short pieces) to fit individual lithography machines. However, sacrificing fiber length obviously brings many disadvantages as well (e.g., the cladding mode is inevitably excited).

In this chapter, we introduce the EBL-based fabrication method relying on planarizing fiber surfaces in a can-like holder. In this way, fiber substrates become compatible with planar fabrication technology (i.e., the optical fibers can be treated in the same way as typical wafers).

4.1 Overview of current fabrication techniques for fiber tips

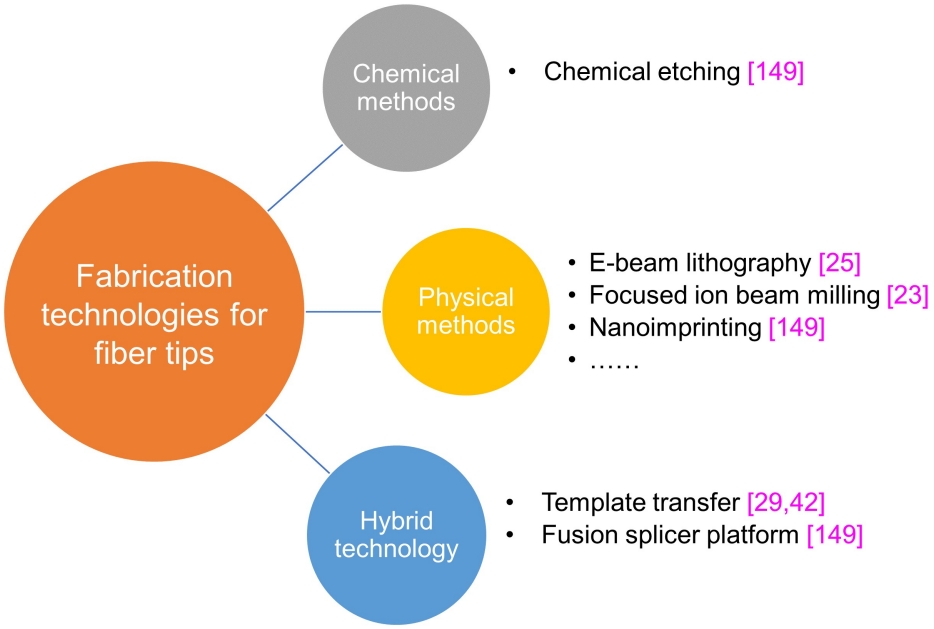

FIGURE 4.1
Currently reported nanofabrication techniques modified for fiber substrates.

First, we briefly review current fabrication methods for micro- and nanostructures modified for fiber application. As shown in Fig. 4.1, these approaches can be generally classified as chemical, physical and hybrid techniques. These approaches are well summarized in refs [149, 175].

To demonstrate the implementation of nanostructures on fiber end faces, we chose electron beam lithography as the fabrication method because of its wide usage in nanostructure creation and extensive team experience in Leibniz-IPHT. A major advantage of this approach is that any type of nanostructure implemented with EBL could be well transferred onto fiber facets [27, 37–39, 41, 46]. Additionally, further modifications of the implementation procedure may allow not only silica fibers but also fibers made from other materials (such as polymers or elastomers) to be used.

We need to note that before being patterned on fiber facets, these nanostructures are first created on planar chips for the purpose of optimizing the manufacturing parameters as well as for performance comparison with fiber substrates.

4.2 Working process of e-beam lithography on fiber facets

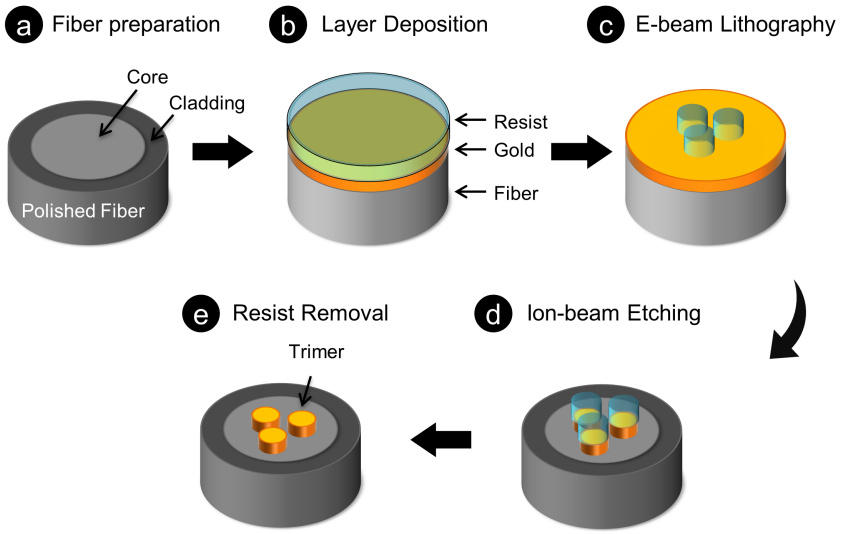

FIGURE 4.2
Fabrication workflow for obtaining a fiber-substrate nanostructure by means of electron beam lithography. The planarized fiber end face goes through various steps, including layer deposition, e-beam lithography, ion-beam etching, and resist removal.

The fabrication procedure [25, 152] of nanostructure patterning on a fiber end face is illustrated as follows (Fig. 4.2):

- Prestep:

Seven fibers are glued within silica capillaries and then inserted into a glass tube (See an image of the fiber bundle in Fig. 4.3 (a)). For protection, the fiber bundles are positioned inside an aluminum support carrier.

- Fiber preparation:

A premise of fabrication is polishing the fiber facet to a flat and smooth surface. Otherwise, any cracks or corrugations may ruin the well-defined nanostructures.

- Layer deposition:

A 40-nm-thick gold film together with 130-nm-thick negative photoresist is placed on the fiber surface by vapor deposition and spin coating (micro resist technology GmbH).

- E-beam lithography and ion-beam etching:

Nanotrimers are written into the photoresist by EBL. Subsequently, the remaining gold (except for the nanotrimers) is removed by ion-beam etching.

- Resist removal:

The photoresist residues are chemically removed. An additional alumina film (thickness of 10 nm) is deposited on the surface by atomic layer deposition (plasma enhanced ALD, tool: Oxford Opal) for the purpose of mechanical protection.

Now, some fabrication details are presented in the following sections. First, we examine the development procedure for the fiber substrate. Microscope images of the fiber end face before and after polishing and cleaning are compared in Fig. 4.3. Obviously, after this step, the surface of the seven-fiber bundle becomes much smoother. Through inspection by the naked eye and a microscope, it is necessary to ensure that no cracks or corrugation remain visible on the facets. To obtain such flat surfaces, the sandpaper (Fig. 4.3 (c)) of the fiber polisher has to be substituted by smaller grit sandpaper.

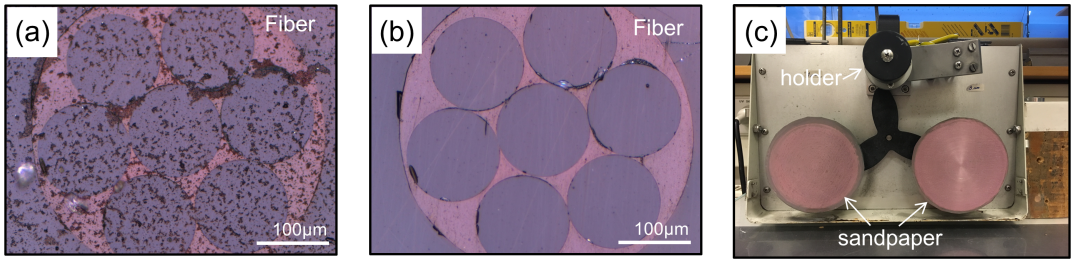

FIGURE 4.3
Fiber preparation. (a) and (b) Fiber end faces before and after polishing. (c) The fiber facet polisher. (type: Buehler fibermet optical fiber polisher)

After fiber preparation, the bundle can be inserted into the housing holder, as shown in Fig. 4.4. Based on the specific type of e-beam lithography machine used (here, a Vistech 350OS), the custom holder (shown in Fig. 4.4 (a)) is a flat metallic cylinder with a diameter of approximately 75 mm and a height of approximately 10 mm. In general, the metallic holder is composed of a cover (left round part in Fig. 4.4 (a), with a hole included to match the fiber bundles) and a base (right ring-like part in Fig. 4.4 (a)). The fibers (meters long) are packed along the inner circular 'wall' of the holder. Finally, the cover and the base can be closed to protect fibers from potential external damage during EBL.

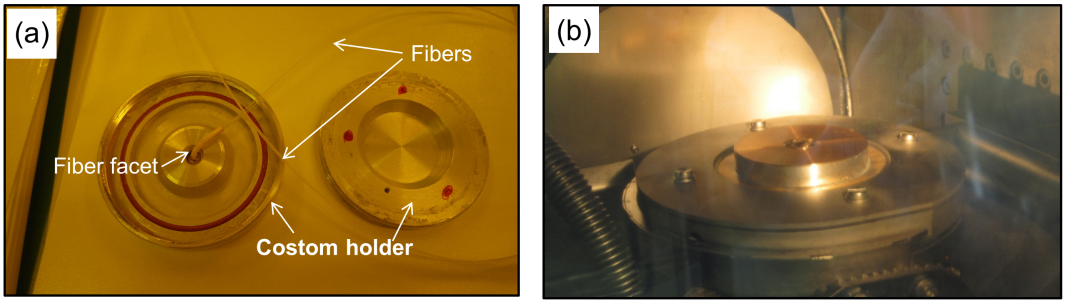

FIGURE 4.4
(a) A custom can-like holder designed for fibers. (b) Ion-beam etching process on the fiber facet.

Note that the holder is designed to only expose fiber facets during the nanoengineering process. An overview of the holder is displayed in Fig. 4.4 (b), where the fiber facets are positioned relative to the ion beam.

4.3 Fabricated fiber-substrate nanostructures

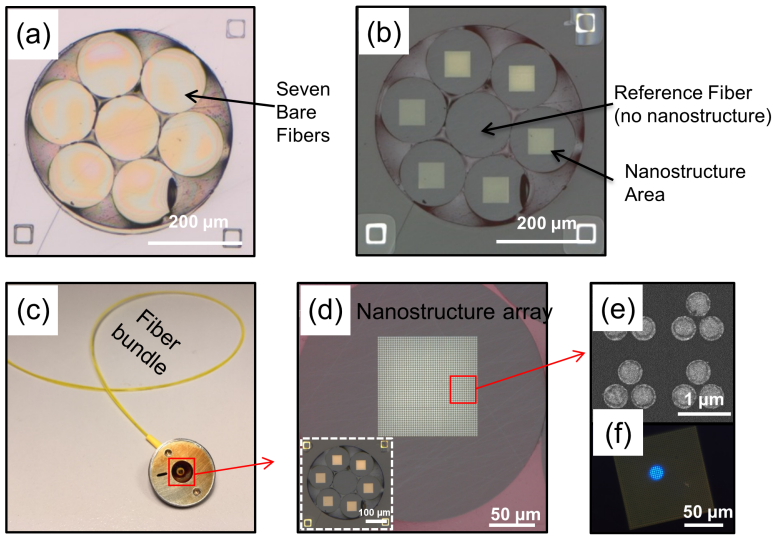

FIGURE 4.5
Images of nanotrimer arrays on fiber end faces. (a) and (b) Seven-fiber bundle facets before and after nanostructuring. (c) A typical fiber bundle composed of seven 50-cm-long fibers. (d) Microscope image showing the array of nanostructures. (e) SEM image of four trimer units on the fiber facet. (f) Image of the output beam spot when white light is coupled into the unstructured fiber tip.

Fig. 4.5 shows one example of a fiber bundle (fiber length of 50 cm) that includes nanotrimer arrays. In this sample (Fig. 4.5 (b)), nanostructures have been fabricated on the end faces of the outer six fibers, whereas the central fiber remains bare (without any nanostructures) for reference.

As shown in Fig. 4.5 (d), the total area of the array (100×100 trimer units, 110×110 μm^2) covers the fiber core region (diameter of $\approx$ 8 μm). The interaction between the fiber mode and metallic array can be straightforwardly observed when inspecting the output mode pattern for the case where white light is coupled into the unstructured side of the fiber. A clear and fine-structured beam spot at the location of the fiber core (close to the array center) is captured in Fig. 4.5 (f).

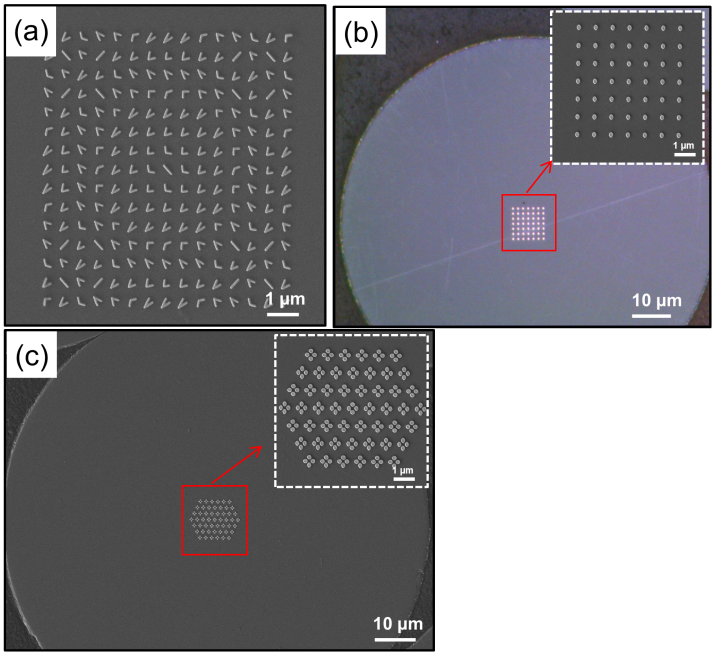

FIGURE 4.6
Several nanostructures fabricated on fiber end faces. (a) V-shaped metasurface. (b) Nanodisk array. (c) Four-dot cross-like array.

Benefiting from e-beam lithography, this top-down method enables a high degree of control of our nanostructures in terms of the structural dimensions and small feature sizes (i.e., the minimum interparticle gap of nanotrimers is below 50 nm). The implementation approach here relies on planarizing the fiber end face rather than modifying the e-beam machine itself. Therefore, our concept can be applied to almost any type of e-beam lithography machine, and any type of nanostructure that has been implemented with this infrastructure is now accessible.

To prove this point, we also produced other nanostructures on fiber end faces. These are displayed in Fig. 4.6 together with corresponding SEM images. From (a) to (c), the plasmonic nanostructures are V-shaped nanobars (a metasurface [16]), single nanodot arrays and four-dot cross-like nanoantennas. These samples strongly confirm the reliability and reproducibility of our fabrication method.

4.4 Chapter summary

Here, we have discussed a fabrication approach for patterning plasmonic nanostructures on the end face of optical fibers. Utilizing a can-like custom holder, the fibers can be planarized to match EBL prerequisites. By adapting this high-precision manufacturing method, we anticipate that nanostructure-enhanced fibers will have a number of important applications, such as in bioanalytics, telecommunications, nonlinear photonics, optical trapping and beam shaping.

Chapter 5

Characterization & application of nanostructured fibers

We have explicitly illustrated the nanostructure design process and deeply studied the optical properties of nanotrimer arrays in chapter 3. In conclusion, the densely packed trimer array has been made to be patterned on an SMF-28 facet by electron beam lithography, where the fabrication process is demonstrated in chapter 4.

In this chapter, we present the characterization of nanostructure-enhanced optical fibers at the beginning of this section. Instead of transmission measurement (corresponding spectral features are covered by measurement errors and noise), we propose to employ the spectral contrast as a key performance factor using the polarization dependence of the nanotrimer array. The definition and measurement procedures for transmission contrast will be explained in section 5.1.

As illustrated in chapter 1, the goal of this study is to implement a functional nanostructure-based optical fiber probe for applications in the fields of sensing, beam shaping, telecommunication, etc. Here, we demonstrate two main uses of nanostructured fibers, as an environmental index sensor and a light detection probe, in sections 5.2 and 5.3, respectively. The first application involves using a nanotrimer-modified fiber as an RI sensor because of the high resonance factor (Q-factor). In the second application, the nanodot array can significantly enhance the light-collecting ability of fibers, especially at a large incident angle. This phenomenon can further be utilized to realize a fiber-based signal probe within the application fields of green photonics and quantum technologies.

Through this chapter, we demonstrate that fiber-integrated functional nanostructures may enrich the 'lab-on-fiber' framework. Please note that some of the results and data have been published in these references [25, 134, 176].

5.1 Characterization of nanotrimer-enhanced fibers

First, let us review the concept of a nanotrimer-enhanced fiber tip (a sketch is shown in Fig. 5.1). Generally, the concept of nanostructure-enhanced fibers aims to realize functional fiber probes by patterning well-defined plasmonic nanoantennas on the facet. Here, we illustrate this idea by integrating a densely packed arrays of gold nanotrimers onto an SMF-28 fiber.

In this specific example (shown in Fig. 5.1), the trimers are arranged in a square lattice (unit cell pitch Λ: 1.1 μm), with the dot diameter (D), height (H) and interparticle gap (G) given by 375 nm, 40 nm, and 75 nm, respectively. An SEM image of the trimer array is shown in Fig. 5.1. (b). Note that the trimer arrangement is slightly different from those studied in chapter 3. The diameter of the nanodots and the intratrimer gap G are both smaller than those of the trimers presented in section 3.3. The reason for utilizing such a geometry is to enhance the electric Fano resonance (see the conclusion regarding Fig. 3.10) to create a stronger asymmetric spectral lineshape. Additionally, the plasmonic resonance of the nanotrimers overlaps the single mode regime of SMF-28 (above 1310 nm). More importantly, this type of nanostructure satisfies all three requirements demonstrated in chapter 3.

The working principle of the nanostructure-enhanced fiber is as follows: Light (working wavelength in the IR regime), which is coupled into the unstructured side of the fiber by a lens or an objective, propagates along the core and reaches the nanostructured tip (patterned with the trimer array here). The plasmonic resonances of the gold nanostructures are excited by the fundamental HE_{11} mode, and the overall fiber optical response should be modified by these nanostructures. As seen from the SEM image in Fig. 5.1 (b), the geometries of the fabricated trimers have good consistency.

First, the optical properties of nanotrimers implemented on planar substrates are studied in depth. Note that the arrays share the same geometry as those created on the fiber end faces (D = 375 nm, H = 40 nm, G = 75 nm, Λ = 1100 nm). The polarization of normal incident light is set as 0° and 90°, where the polarization degree refers to the acute angle between the incident light polarization and the axis of the two lower dots (illustrated by the inserted sketch in Fig. 5.2.(a)). A supercontinuum source (NKT Photonics SuperK Compact) provides broadband incident light, and a spectrometer (Instrument Systems SP320-124) is used to record transmitted light for spectral analysis.

The measured transmission spectra under 0° and 90° polarization are

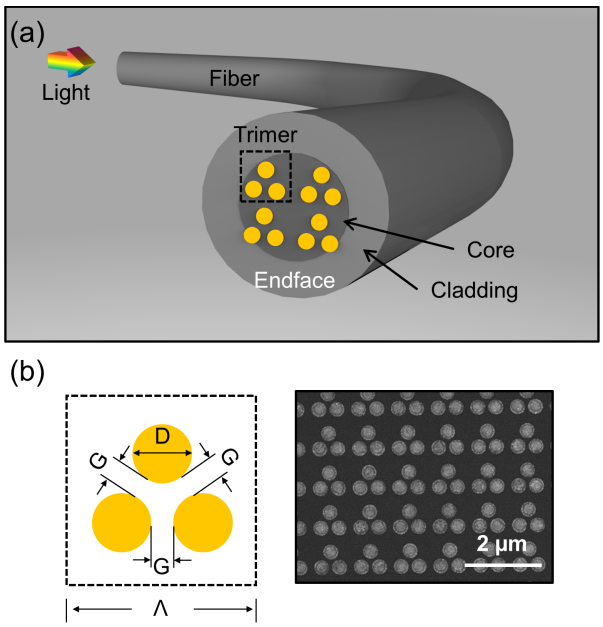

FIGURE 5.1
The concept of a nanotrimer-enhanced optical fiber. (a) Schematic showing an SMF-28 fiber with a trimer array integrated on its end face. (b) Nanotrimer array geometric arrangement. Here, D is the diameter of the nanodots, and G is the edge-to-edge distance between two nanodots. The value Λ denotes the periodic constant (pitch) of the square unit cell. At the right, an SEM image gives an overview of the entire array. In this example, D, G, and Λ are fixed at 375 nm, 75 nm and 1100 nm, respectively.

shown in Fig. 5.2 (a) as the green and magenta curves, respectively. Noticeably, a major transmission dip at approximately 1625 nm is observed for 0° polarization, while a weak but wide dip located at approximately 1580 nm is found when the polarization is rotated to 90°. The transmission of the trimer array shows strong polarization dependence, and the lineshapes are highly asymmetric, especially for the 0° polarization. The spectral minima (near 1600 nm) are both located close to the first diffraction order of the glass substrate (1595 nm, calculated as $\Lambda \times n_{glass}$ = 1100×1.45). The formation of these spectral characteristics have been intensively investigated in chapter 3.

To further analyze the trimer properties, numerical simulations based on COMSOL Multiphysics are conducted using the periodic boundary condition. The simulated spectra are displayed in Fig. 5.2 (b) with a green line for 0° polarization and a magenta line for 90° polarization. Overall, the simulated spectra fit the measurements well, where the two dips at 1600 nm are fully reproduced. The spectral differences between Fig. 5.2 (a) and (b) are

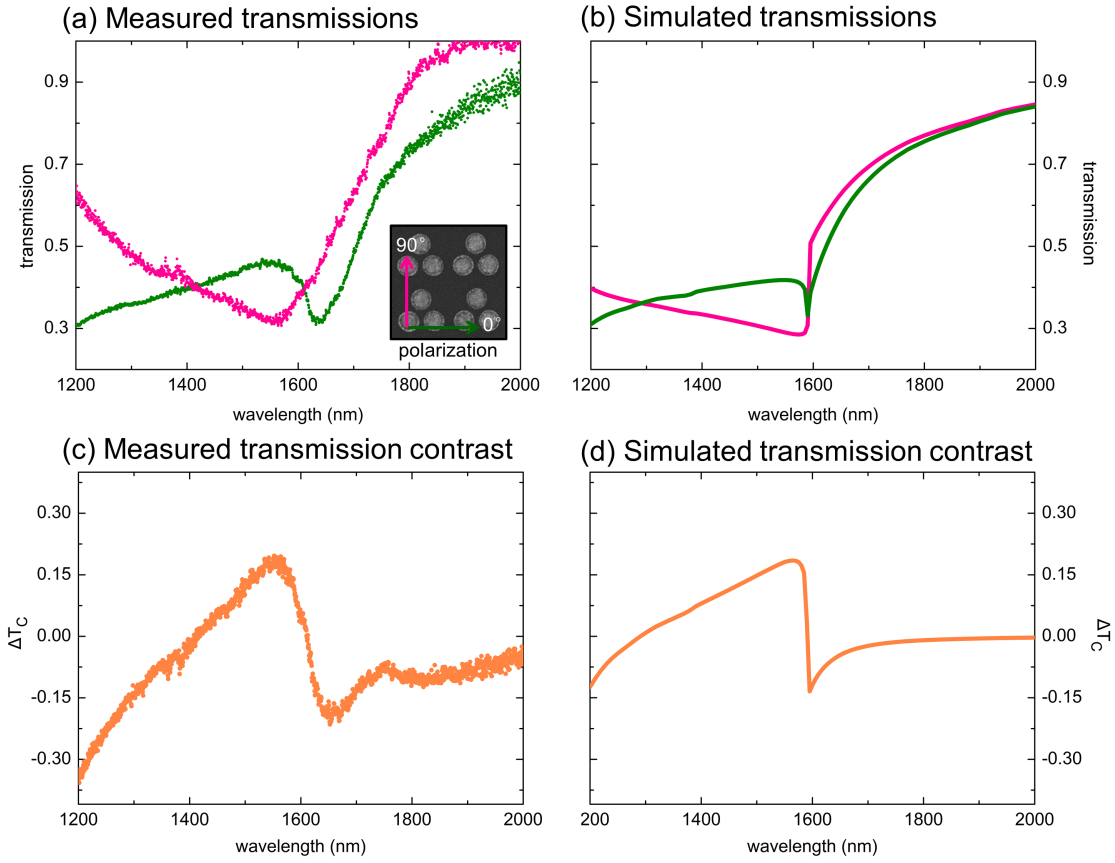

FIGURE 5.2
Measured (a) and simulated (b) transmission spectrum (from 1200 nm to 2000 nm) of nanotrimers on a planar silica substrate. Note that two sets of spectra are obtained in the air-silica environment. The trimer array is illuminated under 0° (dark green) and 90° (dark pink) polarized incident light, where the polarization degree is illustrated in the lower inset of (a). Measured (c) and simulated (d) transmission contrast based on the data from (a) and (b), respectively.

partly attributed to the excitation configuration. In the simulation model, a plane wave (by periodic ports) is used for excitation, while a Gaussian beam (generated by an objective) is launched onto nanotrimers in the actual experimental setup.

Now, we would like to introduce the transmission contrast defined by two spectra obtained under two orthogonally polarized incident beams. This contrast is particularly relevant for the analysis of nanostructures on fiber end faces since an SMF-28 fiber is not polarization maintaining, i.e., the polarization state that reaches the nanostructures is not the same as the input polarization state. In principle, for one contrast curve, two transmission spectra need to be obtained under identical experimental configurations with varied

polarization excitations (i.e., 0° and 90°).

It is essential that the nanostructures exhibit different spectral features over a certain wavelength range under varied excitation. Otherwise, the contrast curve would be rather flat without any 'visible' features. For instance, in the case of the trimer array presented in Fig. 5.2, the positions and amplitudes of two dips distinctly depend on the polarization. This difference allows straightforward extraction of highly polarization sensitive features from the spectral distribution measurements of nanostructures.

Hereby, the transmission contrast (ΔT_c) is defined by the following equation:

$$\Delta T_c = \frac{T(0^\circ) - T(90^\circ)}{T(0^\circ) + T(90^\circ)} \tag{5.1}$$

with $T(0^\circ)$ and $T(90^\circ)$ being the transmission spectra excited by 0° and 90° polarized light, respectively.

Here, we introduce two main methods to acquire ΔT_c. The first one is to measure every single transmission at the corresponding polarization and then calculate the spectral contrast based on Eq. 5.1. The second approach only requires altering the incident light polarization. The transmitted spectrum can be continuously recorded, and thus, a reference fiber is not necessary.

In this work, we adopt the first method for contrast measurement on a planar substrate and the second one for corresponding tests on a fiber end face. Fig. 5.2 (c) and (d) show the measured and simulated transmission contrast of the trimer array on the planar substrate, respectively. Both spectra display high similarities, where dips and peaks are captured at a wavelength of approximately 1600 nm.

Now, we focus on fiber facets patterned with nanotrimers. The experimental setup for contrast quantification is shown in Fig. 5.3 (a). The light from a supercontinuum laser goes through a linear polarizer (Codixx) and is coupled into the bare tip by a 20× objective (Olympus). The light output from the nanostructured fiber facet is guided into an optical spectral analyzer using a multimode fiber (Thorlabs custom fiber). Here, we use this large core fiber (diameter of core: 1 mm) to collect as much output intensity as possible since the signal is very weak (fiber coupling loss > 3 dB).

The polarization of incident light before reaching the fiber is gradually changed from 0° to 180° at a step of 10°, where the initial polarization angle (0°) is arbitrarily chosen. Note that in addition to rotating the polarizer

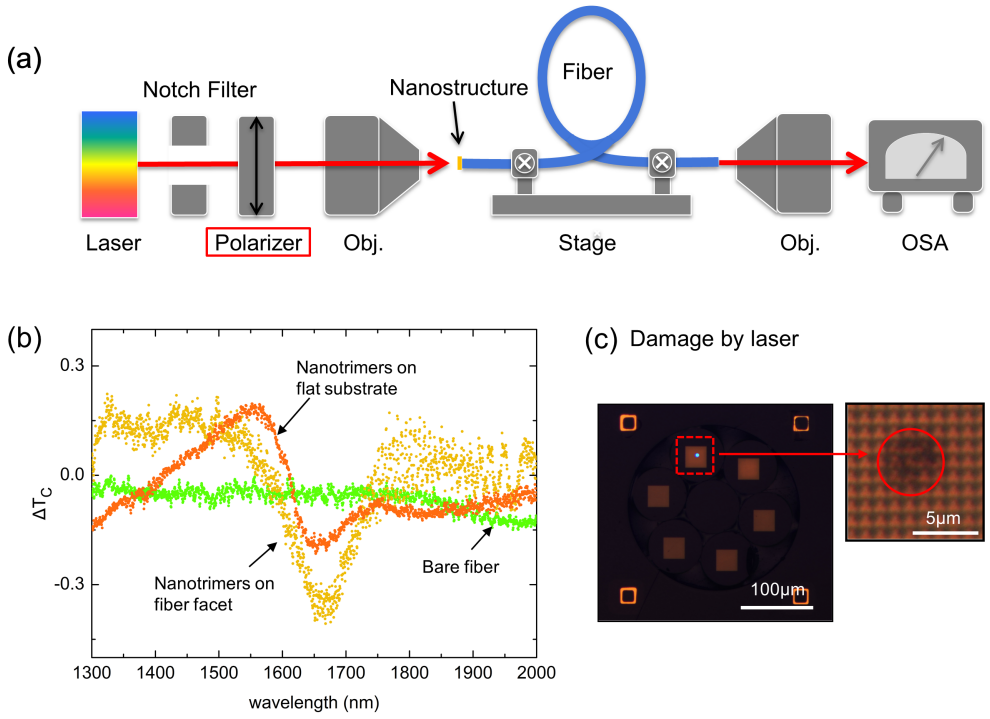

FIGURE 5.3
Transmission contrast measurement on a fiber substrate. (a) Experimental setup. The nanostructured facet of the fiber is facing the incident light in order to observe the nanostructure state. During the measurement process, only the polarizer (highlighted by the red rectangle) is manipulated, and no reference fiber is needed for contrast qualification. (b) Experimental results of bare fiber (green) and nanotrimers on a flat substrate (orange) and fibers (yellow). (c) The array damage due to long-term exposure to the laser.

(highlighted in a red rectangle in Fig. 5.3 (a)), the coupling objective also needs to be slightly altered to compensate for power loss due to misalignment (induced by the rotation of the polarizer).

Therefore, 19 spectra (representing different polarizations 0° to 180°) are obtained. Nine transmission contrasts of the fiber substrate are computed based on Eq. 5.1. Since the 'correct' ΔT_c for planar glass is demonstrated in Fig. 5.2, we can identify the corresponding contrast curve of the fiber substrate based on the spectral feature at approximately 1.65 μm.

Fig. 5.3 (b) compares the measured optical transmission contrasts. The orange curve represents the trimers on planar glass, and the yellow curve indicates the same nanostructure on the fiber end face. The dip positions (approximately 1.65 μm) of the two spectra match well, even though the data variations for the fiber are much larger than those for the planar substrate.

The spectral mismatch between the two substrates may result from the following factors. First, the experimental error of the incident light polarization is $\pm 10^{\circ}$. Second, bending of the fiber can reduce the unwanted cladding mode, but it also introduces birefringence. The spectral variance also partly originates from the experimental configuration differences between fibers and glass substrates. Furthermore, geometric variations of trimers and post-processing of data may also cause spectral inconsistency. In addition, nanostructure damage could also induce data errors. As shown in Fig. 5.3 (c), the trimers located in the fiber core area (highlighted by the red circle) are damaged due to the long-term exposure of the nanostructures to the laser (i.e., thermal ablation).

Nevertheless, the nanostructure-enhanced fiber exhibits a unique spectrum lineshape compared to the bare fiber (the green curve in Fig. 5.3 (b)), which is flat and slightly varies from -0.15 to 0. This result strongly confirms that the optical response of the nanotrimer-enhanced fiber is modified by the applied nanostructure.

5.2 Nanotrimer-based fibers for RI sensing

5.2.1 Introduction of LSPR-based sensing

Effective detection of refractive index variation is of key importance for multiple fields such as optofluidics and single molecule sensing, representing a 'hot' subject intensively addressed by the optics community [177–181]. In terms of RI detection, the working mechanism of plasmonic sensing is the interaction between surface plasmons and the analyte liquid. Conventional thin film SPP sensing is a very mature technique that has been studied for more than three decades [182]. Commercial instrumentation based on thin film sensing has had a considerable impact on bioanalytics research.

Different from the well-studied SPP sensing, LSPR sensing has the major advantage of straightforward plasmon excitation. The former approach requires an additional optical component (e.g., the Kretschmann configuration demands a glass prism, see discussions in chapter 2), while the latter can work without assistant elements. This relaxed excitation demand of LSPR-based sensing enables a compact and portable detection device [183–185].

Owing to the significant enhancements and highly confined electromagnetic fields, two-dimensional LSPR-based sensors are capable of detecting small index changes. Benefiting from the nanoscale geometry of metallic

and/or dielectric structures, these sensors can still actively work even when packed in a tiny volume. This fact is of great help for remote detection in little analyte amounts and space-constrained environments.

Fundamentally, LSPR-based RI sensing relies on the spectral shift due to an index change of the surrounding medium. It is well-studied that the resonance lineshape can be adjusted by modifying the refractive index of the dielectric medium. Here, we concentrate on the spectral evolution mediated by the environmental RI.

5.2.2 RI sensing of nanotrimers on a planar substrate

Owing to the asymmetrical lineshape and narrow features, Fano resonances exhibit a higher resonance factor (Q-factor) compared to LSPRs of isolated nanodisks, which suggests the use of an array of coupled trimers as a plasmonic RI sensor. Apart from the improved Q-factor (value up to 7), there is another advantage of the trimer array (nanodisk diameter of 400 nm) that needs to be noted, which is the unique transmission spectrum with a single sharp peak, leading to a FWHM of $\approx$ 200 nm.

Experimentally, the spectral distributions of the transmission of the trimer array illuminated at a 0° polarization angle have been determined for five different RI liquids (n = 1.33 to 1.73) to study the impact of the environment on the optical response of the trimer array. The measured spectra are shown in Fig. 5.4 (a), and the spectral shift is further analyzed in (b).

The experimental arrangements for RI sensing are demonstrated in Fig. 5.4 (c). A sticky foil (orange thin slice with a thickness of 1 mm) is placed on the surface of the planar substrate. There is a central hole in this foil to reserve a space for nanostructures. Analyte liquids with different RIs are injected into this small chamber, after which the top opening is sealed by a transparent glass slide during the experiments. One issue that has to be particularly considered is to avoid bubbles when dealing with these liquids.

In general, the original resonance spectral position (near 1600 nm) of the nanotrimer array for the media arrangement of air-superstrate shifts towards longer wavelengths as the RI of the liquid increases. This spectral redshift is highlighted by the dashed red line in Fig. 5.4 (a). All Fano resonance wavelengths are plotted in Fig. 5.4 (b) (black squares, left axis) along with the corresponding calculated Q-factors (orange squares, right axis). The spectral positions and FWHM of the transmission peaks are acquired by fitting a Lorentz function within a certain spectral bandwidth (approximately 400

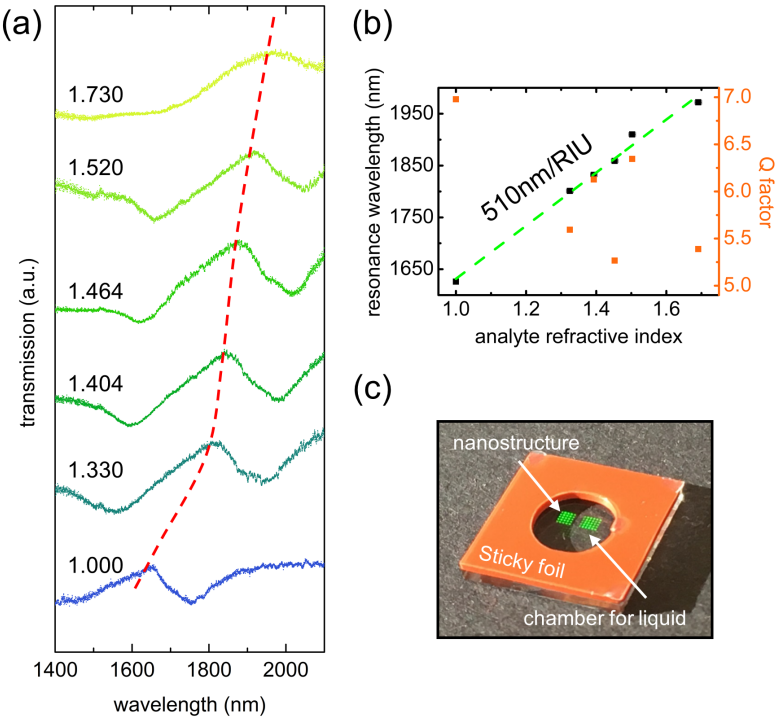

FIGURE 5.4
(a) Transmissions of a nanotrimer array located on a planar glass substrate (n = 1.45) immersed in analyte liquids of different refractive indices. Here, each curve refers to one measurement, and the upper numbers indicate the corresponding refractive index value. (b) Resonance wavelength (red dashed line in (a)) as a function of the analyte refractive index, corresponding to the wavelength of the peaks (black dots). The orange squares indicate the corresponding resonator quality factors (Q-factors). (c) Experimental configuration for RI sensing using nanotrimers on a flat glass substrate.

nm). The resonance wavelength can be well fitted by a linear function (green dashed line), which shows an RI sensitivity of 510 nm/RIU (coefficient of determination R^2 = 98.8%).

The trimer array offers sensitivity on the same order of magnitude as randomly distributed gold nanodisks (RI sensitivity ≈ 180 nm/RIU [37, 46]) and trimer lattices (≈ 170 nm/RIU in VIS [186], ≈ 370 nm/RIU in IR [186]). The trimer array sensitivity also exceeds the sensitivity of other reported Fano resonance structures (approximately 300 nm/RIU in nanohole quadrumers [187] and heptamer cluster [188]). Together with the large Q-factors (all above 5), the results clearly suggest that the trimer array is an alternative platform for high-precision RI sensing.

One additional advantage of our trimer array is that the working area

can be minimized to several μm^2 in size due to the dense geometric configuration. In the next section, we will show the sensing performance of a trimer-modified fiber sensor where the total size of the sensing area is approximately 80 μm^2 (fiber core section), which would be difficult if the array was very dispersed.

5.2.3 Nanotrimer-enhanced fiber-based RI sensor

Now let us focus on the RI sensing performance of nanostructure-enhanced fibers. To demonstrate its potential, the spectral distribution of the transmission contrast of the nanotrimer-based fiber has been measured in the situation where the nanostructures are immersed in an aqueous analyte. For these measurements, a glass slide is placed close to the nanostructures (distance between fiber end face and glass slide: 1 mm, see the similar configuration shown in Fig. 5.4 (c)), and the gap is filled with analyte refractive liquid (n = 1.33).

The measured spectra (Fig. 5.5) clearly reveal that the main dip originally located at approximately 1650 nm (dark green points) shifts to approximately 1800 nm as the RI increases from 1.0 (air) to 1.33. The resulting RI sensitivity is approximately 390 nm/RIU, which is about two times higher than that for the reported LSPR fiber tip sensors ($\approx$ 190 nm/RIU [37, 46]).

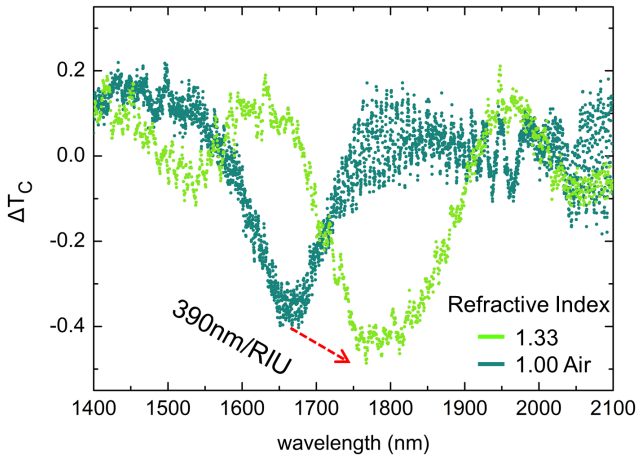

FIGURE 5.5
RI sensing with a nanotrimer-based fiber tip by measuring its transmission contrast spectra. The red arrow indicates the spectral redshift of the main dip.

Unfortunately, the weak adhesive force between the nanostructure and fiber surface cannot sustain more tests after cleaning. The nanotrimer array

on the fiber core is ablated and completely removed (see the damaged example in Fig. 5.3 (c)). However, based on the result of Fig. 5.4, we believe that a nanotrimer array on a fiber end face would show identical behavior, e.g., the dip will redshift following a linear relationship with the surrounding RI.

5.3 Nanodisk-assisted fiber probe for light collection

5.3.1 Weak signal detection at wide angles

To effectively collect light, optical lenses and sophisticated optical systems have been systematically studied [189]. For free-space objectives, the key parameter to evaluate the light-gathering capacity is the numerical aperture (NA), which is defined as $NA_{obj} = n \times \sin\theta$. Here, n refers to the refractive index of the medium, and θ denotes the maximum reception angle. Currently, commercial objectives reach a maximum NA of 0.96 (in air) [190], corresponding to a collection angle θ of $\approx 73^{\circ}$.

Due to the internal multilens systems, well-designed optical objectives normally have a relatively bulky geometry with limited working wavelength range and a submillimeter focusing length [191]. These disadvantages inhibit high NA objective applications in space-constrained situations. A common alternative method to improve the NA is to increase the RI of the surrounding medium, e.g., by using water (n = 1.33), glycerin (n = 1.47), or immersion oil (n = 1.51). However, it is not practical to fill free space with these liquids under dry working conditions.

Let us return to the optical fiber aspect. As illustrated in the introduction chapter, fibers are commonly used in the modern telecommunication industry and can transport optical signals over hundreds of kilometers with extremely low loss. Hence, the use of optical fibers to collect and transport weak optical information would benefit numerous applications such as wide-field fiber endoscopy [192] and green photonics (e.g., photovoltaics).

However, commonly used step-index fibers have a very weak light gathering ability. For instance, the NA of SMF-28 is only 0.16 at the wavelength of 1550 nm. This small NA value is a result of the slight RI variation ($\Delta n = 4 \times 10^{-3}$) between fiber core ($n_{co}$) and cladding ($n_{cl}$). More information can be found in the discussion of chapter 2.

To enhance the fiber light-collecting ability, several studies have suggested using microstructured fibers [11, 193] to increase Δn. For instance, William

J. W. *et al*. developed two types of double-clad air-silica optical fibers to decrease the RI of the cladding [193]. The suspending webs (width of 230 nm, located at the additional outer cladding) are filled with air (n = 1.0), and thus, Δn becomes much larger than that of SMF-28, yielding NA > 0.9 at the wavelength of 1.54 μm.

Alternatively, the material of the core and cladding can be carefully selected to increase the index difference [11, 194]. For example, a commercial high NA multimode fiber [123] has a hard polymer cladding ($n_{cl} \approx 1.365$, $n_{co} \approx 1.458$), resulting in an NA of 0.50 at 589 nm. However, these methods change either the fiber structures or materials and thus cannot be directly applied to an SMF-28 fiber.

In addition, another approach is to place miniature lenses on standard fiber facets [195–197]. In this way, the optical fiber can remain intact, while the light-gathering improvement is limited by the lens performance.

5.3.2 Concept of nanodisk-enhanced light collection

Due to the rapid development of nanophotonics in the last decade, the manipulation of light at the nanoscale has become a reality. Based on resonant elements such as nanobars [15, 16, 198], nanodisks [199] and nanopillars [18], a metasurface is artificially designed to tailor light propagation by introducing an additional phase gradient [15, 200]. Several works [201–203] have demonstrated that nanostructure-based metalenses exhibit extraordinary light collection performance (NA close to 1) with a subwavelength geometry.

Here, we apply plasmonic resonance structures on the facet of a standard step index fiber to boost its light-collecting ability. Although the nanodot array may not be the ideal nanostructure, we still observe significant improvement of the fiber in-coupling performance compared to bare fibers. In addition, instead of fiber NA measurement, actual coupling experiments at different incident angles (0° (normal incidence) to 80°) are conducted to evaluate the fiber light-gathering performance.

The working principle of the nanodot-based fibers for improving light collection is schematically illustrated in Fig. 5.6. A gold nanodot array is fabricated on the facet of a fiber by means of EBL. When incident light is launched at this nanostructure-enhanced tip at an angle of incidence θ, some of the light will be reflected into the air, and some could excite plasmonic

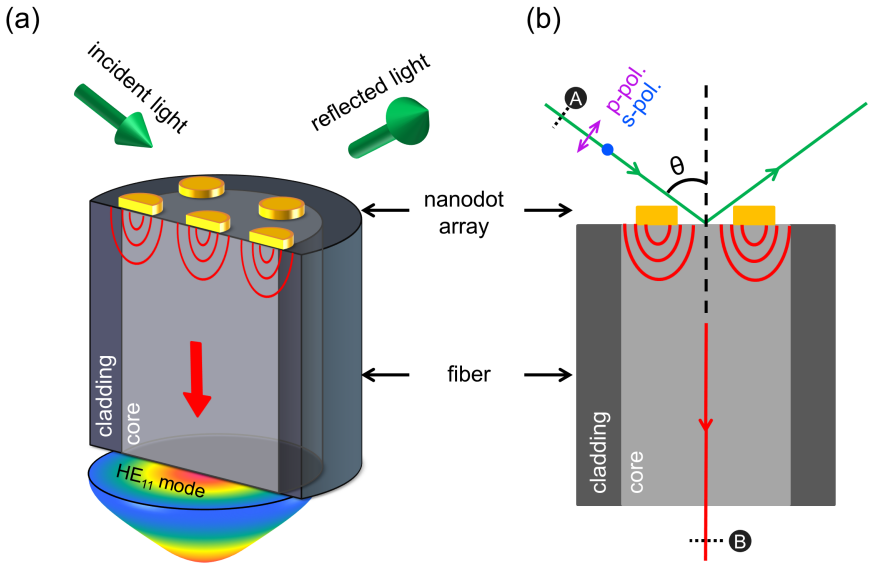

FIGURE 5.6
Overview (a) and side view (b) of a nanodot-based fiber tip for enhanced light-collecting ability. The incident light (green arrow) impinges on the facet of the fiber at an angle of θ and excites plasmon resonance of gold nanodots. The red arrows and curves denote the scattered electromagnetic fields that are coupled to the fundamental HE_{11} mode of the fiber used. The purple arrows and blue dots in (b) illustrate the incident light polarization state. Here, points A and B are the positions used to determine the coupling efficiency η.

resonances due to the presence of gold particles. The radiation fields of individual nanodots could be coupled into the core and thus improve the fiber light-collecting ability. Additionally, the grating-like distribution formed by the periodically arranged nanodisks could diffract some of the light into the fiber. We will further explore these two optical effects using a toy model and numerical simulations in subsequent studies.

Note that a key parameter to evaluate the fiber light-gathering ability - the coupling efficiency η - is defined as the power ratio at positions B and A in Fig. 5.6 (b), i.e., $\eta = P_B/P_A$. In the subsequent sections, the parameters (including periodic constants of the array, incident light wavelength and polarization) related to the fiber coupling efficiency are investigated in-depth by experimental measurements and compared to numerical calculations.

As the first step, we examine the optical properties assuming the nanodot lattice at the end face of an SMF-28. After the procedures of layer deposition, e-beam lithography, ion-beam etching and resist removal, an array of gold nanodisks (D: 480 nm, thickness: 40 nm) are successfully patterned on the

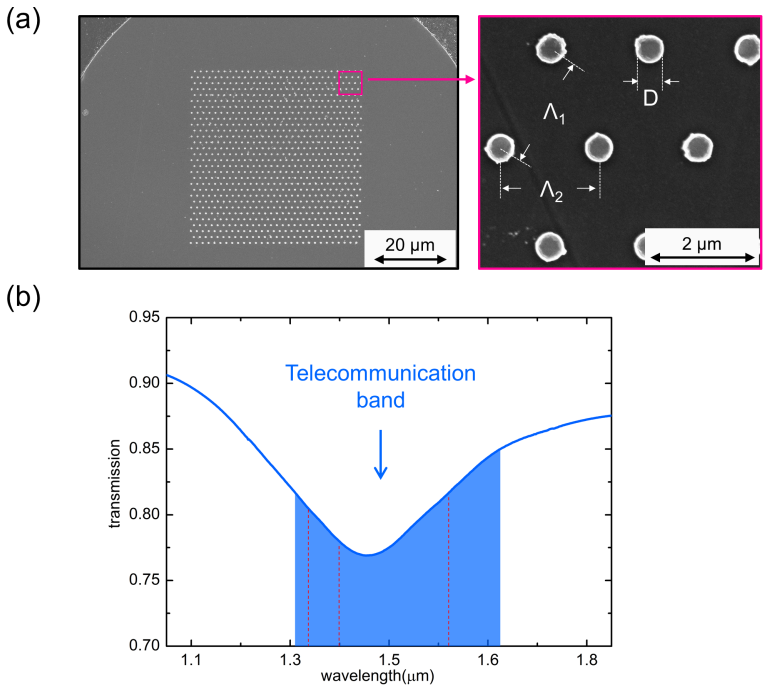

FIGURE 5.7
SEM image (a) of a nanodot array (on a fiber facet) together with its optical transmission spectrum (b) (measured on a planar substrate). D stands for the diameter of the nanodisks. Λ_1 and Λ_2 are the two periodic constants (pitch) along the respective lattice axes. The three dashed red lines indicate the experimental wavelengths of 1310 nm, 1400 nm and 1560 nm, respectively.

facet of long fibers (length of approximately 50 cm; more fabrication details can be found in chapter 4). Note that the area of the nanodots should span the fiber core section (diameter of 10 μm). To address this issue, the total size of patterned nanodisks is 50×50 μm^2, which is approximately 30 times larger than the core section size.

As shown in Fig. 5.7 (a), these gold nanodisks are arranged in a hexagonal unit cell with two periodic constants Λ_1 = 1.9 μm and Λ_2= 1.7 μm). In Fig. 5.7 (b), we present the transmission spectrum of the dot array on a planar silica substrate (same nanodisk geometry as for the fiber sample). Clearly, the LSPR wavelength of the dot array ranges from approximately 1100 nm to 1600 nm, overlapping the telecommunication band (blue background) and SMF-28 single mode regime. Due to the sufficient interparticle distance (at least two times larger than the dot diameter), the lattice resonance arising from the dot-to-dot diffractive coupling should be suppressed at this specific wavelength, which is confirmed by the symmetric transmission lineshape.

5.3.3 Theoretical and numerical calculations

Now, we investigate the fiber in-coupling problem starting with a bare fiber (without nanostructures) illuminated by a Gaussian beam. In general, the fiber coupling efficiency can be calculated using the surface overlap integral between the field amplitudes of the fiber mode and the incident light on the facet. Here, only the HE_{11} mode of an SMF-28 fiber is considered, where the mode profile can be approximately interpreted as $E \propto exp(-x^2/w^2)$ in one dimension.

In fact, there are multiple factors that influence the coupling efficiency, such as optical aberrations, mismatch of the incident beam, and misalignment of the optical fiber (defocusing, lateral displacement, and angle deviation in the arrangement of the fiber) [204]. To simplify the model, we assume a well-cleaved fiber tip excited by a Gaussian beam (wavelength λ) at the incident angle of θ, which is schematically illustrated in Fig. 5.8 (a).

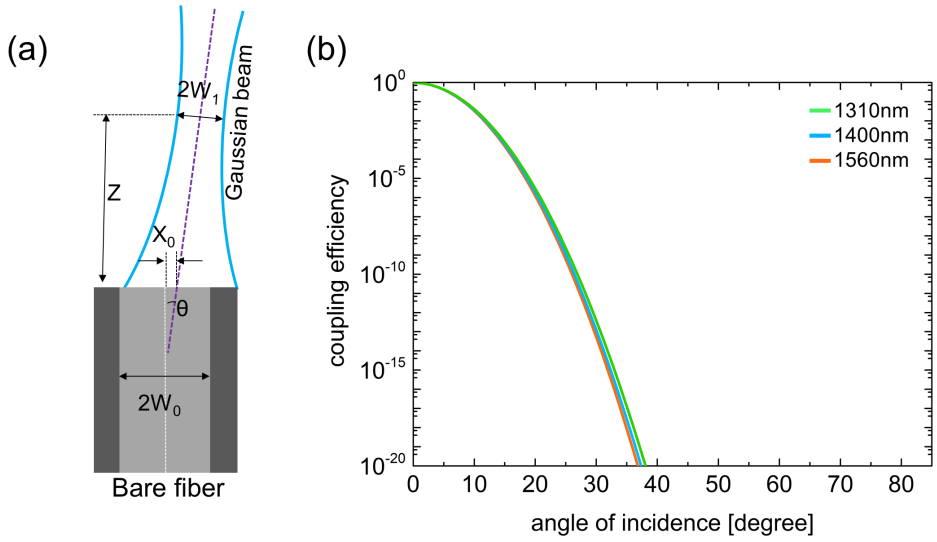

FIGURE 5.8
Analytical model calculations of the coupling efficiency for a bare fiber tip. (a) Model background. (b) Coupling efficiencies computed at wavelengths of 1310 nm (green), 1400 nm (blue), and 1560 nm (orange).

Here, W_1 and W_0 are the incident beam spot waist and fiber core radius, respectively. X_0 is the lateral misalignment between the beam waist and the fiber facet, and Z is the distance from the beam center to the fiber facet. Assuming no displacement Z, the coupling efficiency η is calculated by the following equation [204]:

$$\eta = \kappa_0 \exp\left[-\frac{2X_0^2}{W_1^2 + W_0^2} - \frac{2\pi^2\theta^2 W_1^2 W_0^2}{\lambda^2(W_1^2 + W_0^2)} \right] \tag{5.2}$$

where $\kappa_0 = \frac{4}{(W_0/W_1 + W_1/W_0)^2}$.

The fiber coupling efficiency η can be further simplified provided that the lateral mismatch X_0 is 0:

$$\eta = \kappa_0 \exp\left[-\frac{2\pi^2\theta^2 W_1^2 W_0^2}{\lambda^2(W_1^2 + W_0^2)} \right] \tag{5.3}$$

Equation 5.3 demonstrates that η is primarily related to the angle of incidence θ once the parameters of the fiber and incident beam are given. To visualize the correlation between η and θ, we calculate the coupling efficiency at three wavelengths (green: 1310 nm, blue: 1400 nm, and orange: 1560 nm; these three wavelengths are used in the following experiments) and plot the corresponding data in Fig. 5.8 (b) (all necessary parameters of the light beam and fiber are obtained from the experimental configurations in Fig. 5.13).

This diagram clearly suggests that the fiber coupling efficiency η drops significantly as the angle of incidence increases. In particular, when θ exceeds approximately 35°, the amplitude is less than 10^{-20}. Such a small value cannot possibly be detected in actual experiments. We also observe that the three curves slightly diverge at large angles (> 20°), where the efficiency tends to be smaller at longer wavelengths.

As mentioned in Fig. 5.6, there are two major contributions (the grating effect and plasmonic resonance) to the enhancement of the fiber coupling efficiency. Now, we employ a toy model [2, 205] to investigate the metallic grating effect on the enhancement of the fiber light-collecting ability.

As depicted in Fig. 5.9, the toy model describes the physical background in which the Gaussian-like fiber fundamental mode is excited by a plane wave k_0. At an angle of incidence θ, the plane wave exhibits a lateral (along the x-direction, indicated by the green arrow in the right corner) phase variation (namely, the oscillating factor), which is proportional to $\exp(ik_x x)$. Here, k_x is the x-component of the wavevector, i.e., $k_x = k_0 \sin\theta$. Hence, the defined coupling strength $C_b(\theta)$ is proportional to the following quantity:

$$C_b(\theta) \propto \cos\theta \cdot \left| \int_{-\infty}^{\infty} e^{-x^2/w^2} e^{ik_x x} dx \right|^2 \tag{5.4}$$

We further establish a relative bare-fiber coupling efficiency $\eta_b(\theta)$ by normalizing $C_b(\theta)$ to the perpendicular incidence value ($\theta = 0°$, $C_b(0)$), i.e.,

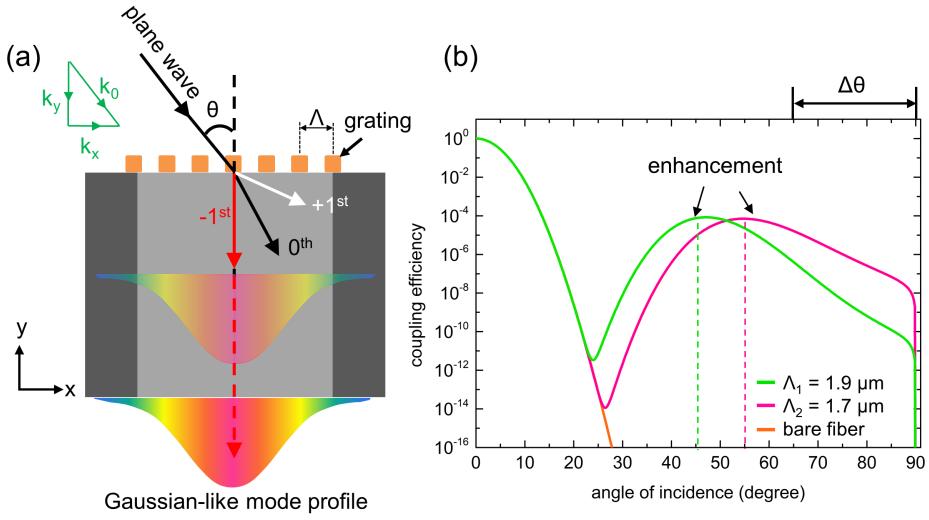

FIGURE 5.9
A toy model to evaluate the grating-mediated fiber coupling efficiency. (a) The toy model background. (b) Calculated coupling efficiency of a bare fiber (orange line, overlapped with two other curves) and fibers with nanostructures (green: pitch Λ_1 of 1.9 μm, magenta: pitch Λ_2 of 1.7 μm).

$\eta_b(\theta) = C_b(\theta)/C_b(0)$. Represented by the orange curve in Fig. 5.9 (b), the maximum fiber coupling efficiency of the bare fiber occurs under an incident angle θ of 0° (i.e., k_x=0), and this value decreases dramatically for $\theta > 0°$ due to the presence of oscillating factor $\exp(ik_x x)$.

However, in a configuration where a periodic grating (periodic constant Λ) is placed on the fiber facet, the lateral wavenumber is modified as $(k_x + N \cdot G)$, in which $G = 2\pi/\Lambda$ and N is any integer. Correspondingly, the grating-modified oscillating factor becomes $\exp(i(k_x + N \cdot G)x)$, which can be less than the original value (without a grating) for a negative N. Therefore, the coupling efficiency is additionally enhanced when the oscillating factor becomes unity ($e^0 = 1$), e.g., $k_x + N \cdot G = 0$. Here, considering only the case of N = -1, this results in the grating-assisted $C_g(\theta)$:

$$C_g(\theta) \propto cos\theta \cdot \left| \int_{-\infty}^{\infty} e^{-x^2/w^2} (a_0 e^{ik_x x} + a_{-1} e^{i(k_x - G)x}) dx \right|^2 \tag{5.5}$$

where a_0 and a_{-1} are the relative amplitudes of the diffraction orders ($a_0^2 + a_{-1}^2 = 1$). Again, the grating-configured fiber relative coupling efficiency defined as $\eta_g(\theta) = C_g(\theta)/C_g(0)$.

The relative grating-modified fiber-coupling efficiencies are presented in Fig. 5.9 (b) (green: Λ_1 = 1.9 μm, magenta: Λ_2 = 1.7 μm, a_0 = 0.99, a_{-1} =

0.01; the value of a_{-1} are chosen to be small to demonstrate that even a tiny improvement of a_{-1} could significantly enhance the light-gathering ability.). Overall, amplitude enhancement of the nanostructure-modified fiber can be observed within the incident angle range from 25° to 80°.

In particular, we find the additional enhancement (highlighted by the vertical dashed lines) located at around 55° for Λ_1 = 1.9 μm and 65° for Λ_2 = 1.7 μm. The angle position of additional enhancement corresponds to the periodical constants of the used gratings, which could be directly computed by $\theta = \arcsin(\lambda/\Lambda)$ [122]. Using this simplified formula, the predicted angles are 55° (Λ = 1.9 μm) and 66° (Λ = 1.7 μm), matching theoretical model calculations.

Furthermore, we calculate the integral coupling efficiency $C_{int}(\Delta\theta)$ of $\Delta\theta$ from 0° to 90° (defined as $\Delta\theta = 90° - \theta$ indicated in Fig.5.9 (b)), which is a key parameter to evaluate the probe working performance (computed as $C_{int}(\Delta\theta) = \int_{0°}^{\Delta\theta} \eta(\Delta\theta) d\Delta\theta$). Based on the result in Fig. 5.10, significant improvements in the grating-mediated light coupling efficiency (magenta and blue curves) are observed, especially at $\Delta\theta$ angles from 0° to 65°, where the bare fiber (orange curve) fails to detect any signal.

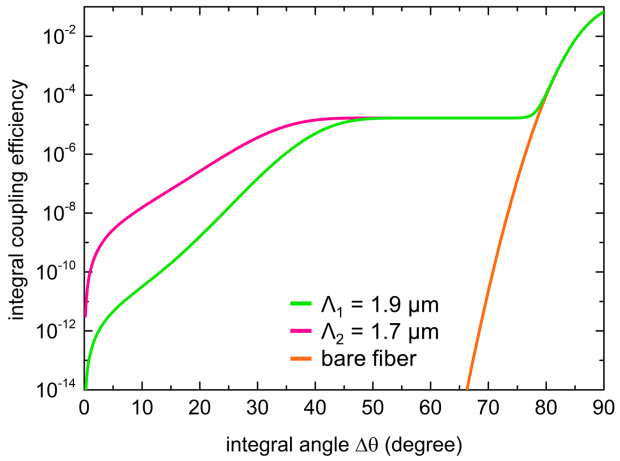

FIGURE 5.10
Integral coupling efficiency at large angle interval of $\Delta\theta$.

It should be noted that the experimental setup for fiber coupling is much more sophisticated than the analytical model. Instead of plane wave excitation, a focused Gaussian beam is utilized (generated by an aspherical lens) in the actual optical configuration. Therefore, the fiber coupling efficiency

could be further improved by an appropriate selection of lenses and optimization of the optical system. However, here, we focus on the fiber coupling enhancements enabled by plasmonic nanostructures. Under identical experimental configurations, the coupling efficiency of nanostructure-based fibers is improved by several orders of magnitude compared to bare fibers (experimental data presented in the next section), which cannot be achieved by merely adjusting the optical path.

Regarding the second major contribution to fiber coupling enhancements, numerical simulations (COMSOL Multiphysics) are conducted. To decrease simulation difficulties, nanodots distributed in a square-shaped unit cell (periodic constant: Λ) are adopted. This simplified model is schematically depicted in Fig. 5.11 (a) and (b), together with the model images in (c), (d), and (e).

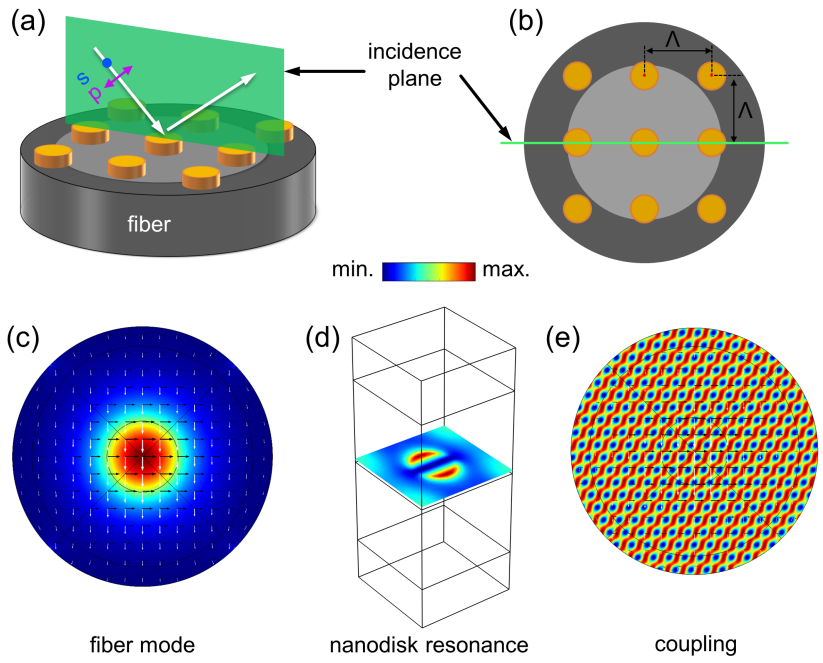

FIGURE 5.11
Numerical simulation model of nanodisk-based fiber coupling. Overview (a) and top view (b) of a sketch showing the simulation 3D geometry. (c) Simulated fiber model exhibiting the fundamental HE_11 mode profile. (d) Nanodisk resonance pattern in a square-shaped unit cell. (e) Coupling of the nanodisk resonance electromagnetic field to a fiber.

Here, the incidence plane (green background) is set to be parallel to the

grating (periodic constant Λ), and incident light beams with two types of polarization (p- and s-polarization, purple arrow and blue dot in (a)) are considered (p- and s-polarization are separately simulated). The fiber coupling efficiencies as a function of incident angle (0° to 80° in a step of 5°) and pitch (1600 nm to 2600 nm at a step of 100 nm) are numerically calculated and presented in the color maps of Fig. 5.12 (a) and (b).

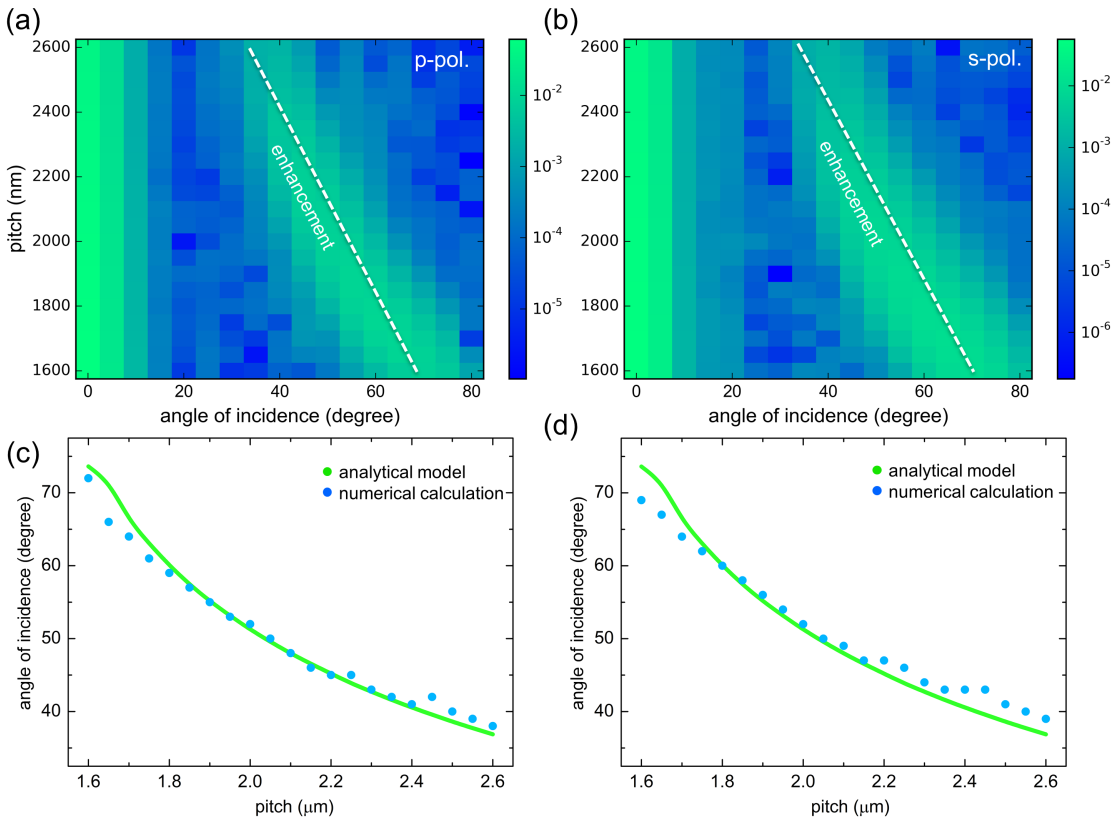

FIGURE 5.12
Simulated fiber coupling efficiency as a function of incident angle and pitch for p- and s-polarized input light. In (a) and (b), the two white dashed lines indicate the additional enhancement of the coupling efficiency, which is related to the periodic constant. (c) and (d) Correlation between the incident angle θ and the pitch Λ. The blue dots represent the additional enhancement values obtained from numerical calculations, and the green line is acquired based on the analytical model equation $\theta = \arcsin(\lambda/\Lambda)$.

Here, the fiber coupling efficiencies for the two polarizations show strong similarities. Overall, the maximum coupling efficiency occurs at the normal incident angle (0°) as predicted by the toy model, where the additional enhancements (indicated by the two white dashed lines) are both located at

nearly the same incident angles (from approximately 40° to 80°). The positions of these enhancements shift to a larger angle as the pitch is reduced.

The incident angles corresponding to the additional enhancement under various pitch configurations and polarizations are examined in Fig. 5.12 (c) and (d). Using the simplified grating equation $\theta = \arcsin(\lambda/\Lambda)$, the projected angle positions (green dots) match very well with the numerical calculations. Obviously, as the pitch increases, the secondary improvements gradually shift to smaller incident angles, which also agrees with the toy model calculations.

5.3.4 Experimental performance

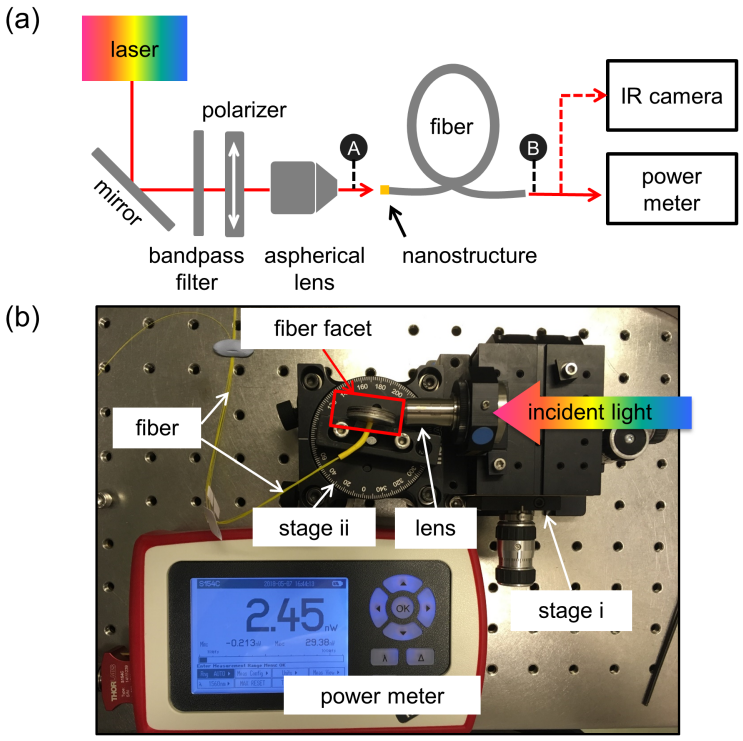

FIGURE 5.13
Schematic (a) and real experimental setup (b) for fiber coupling efficiency measurement. In (b), the angle of incidence is set at 80°, and the power meter reads a measured output value of 2.45 nW. The red frame highlights the nanodot-based fiber tip.

In the experimental setup (Fig. 5.13), we use a supercontinuum laser (NKT Photonics) and several bandpass filters (Thorlabs, 1310 nm, 1400 nm, and 1560 nm) plus an IR polarizer (Codixx) to obtain the needed incident light states. A focused Gaussian beam is generated by an aspherical lens

(Thorlabs C560TME-C) and further coupled to the nanostructured tip. The output power is analyzed by a power meter (Thorlabs PM100) and an IR camera (ABS GmbH). Fig. 5.13 (b) provides a real-time measurement of the fiber coupling efficiency. The nanostructured fiber tip is placed on a rotation stage (labeled 'stage ii' in Fig. 5.13 (b)), which can be used to adjust the incident angle from 0° to 90°. The seven-fiber bundle is bent to reduce the impact of the cladding mode. Although the facet is set almost parallel to the incident light (θ = 80°), the nanodisk-modified fiber tip can still collect a certain amount of light, showing 2.45 nW on the power meter screen (see the displayed value in Fig. 5.13 (b)).

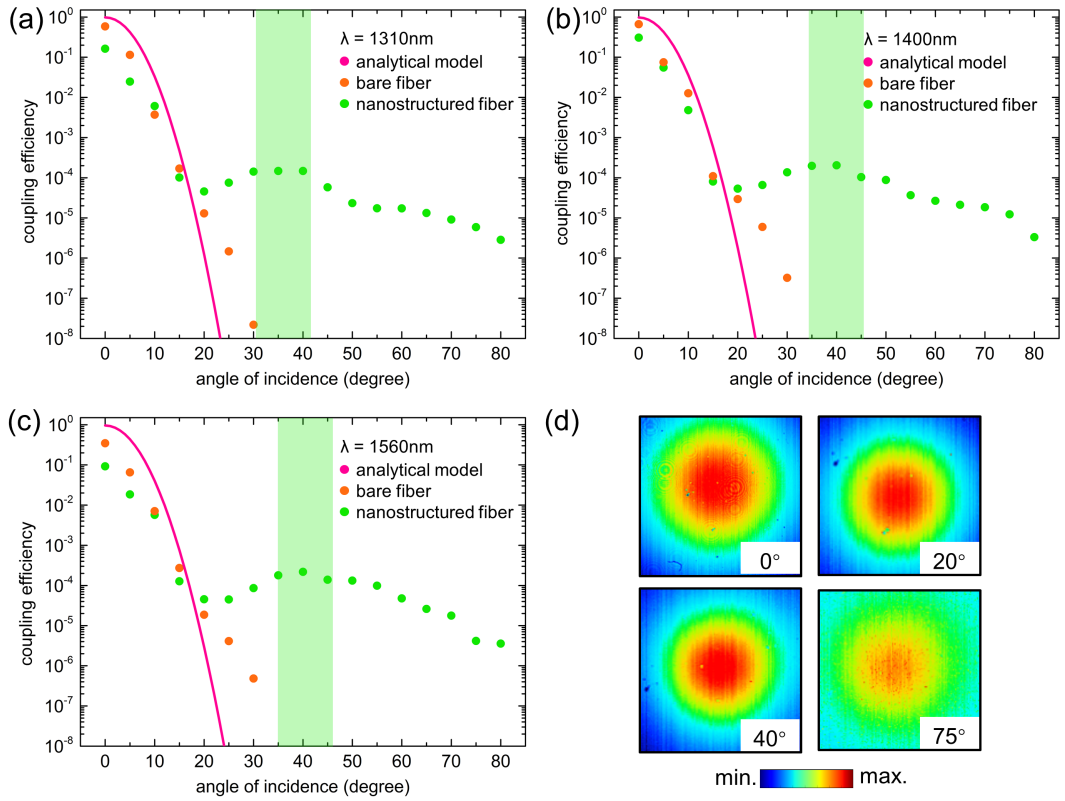

FIGURE 5.14
Measured coupling efficiency of the nanodisk-enhanced fiber tip at the wavelengths of 1310 nm (a), 1400 nm (b), and 1560 nm (c). The green backgrounds highlight the secondary amplitude enhancement. (d) Nanodot-based fiber mode images obtained from an unpatterned tip (measured at 1400 nm). All mode images at the four selected incident angles (0°, 20°, 40°, and 75°).

The coupling efficiency (green dots) of nanodisk-based fibers at wavelengths of 1310 nm, 1400 nm, and 1560 nm are shown in Fig. 5.14 (a), (b), and (c), respectively. During the measurements, the incidence plane is aligned

with the lattice axis with the periodic constant of Λ_1 (1.9 μm). For comparative studies, bare fiber tip (orange dots) and analytical mode (magenta line) calculations are also shown in the corresponding diagrams.

Overall, the bare fiber exhibits the best coupling efficiencies from 0° to 20°. The lower efficiency of the nanostructure-modified fiber can be attributed to the energy loss within the metallic array. According to the spectrum of Fig. 5.7 (b), the transmission loss of the gold nanodot array reaches 25% at normal incidence.

However, above 20°, the performance of the nanostructure-functionalized fiber (the amplitudes are all above 10^{-6} at the three wavelengths) remarkably surpasses that of the bare fiber. Particularly, when the incident angle is > 30°, the coupling efficiency of the bare fiber cannot be characterized due to the extremely small values (less than 10^{-8}, absolute measured value < 1 nW), while the nanodot-modified fiber can still effectively collect light even at an angle of 80°. These measurements strongly confirm that the fiber light-gathering ability is improved by several orders of magnitude due to the presence of the nanodot array.

It is of great interest to investigate the secondary amplitude improvement of the coupling efficiency (highlighted by the green background in Fig. 5.14 (b) to (d)) at approximately 30° to 45° in all nanostructured fiber measurements, which slightly shifts to larger angles with increasing wavelength. These local enhancements match the toy model and numerical simulation results, showing that a small value of the diffraction coefficient a_{-1} can substantially boost the fiber light-collecting performance.

The photographs in Fig. 5.14 (d) are the mode images of nanostructured fibers at incident angles of 0°, 20°, 40° and 75°. All images display a Gaussian beam profile corresponding to the fundamental HE_{11} mode of SMF-28. As the incident angle increases, the mode profiles become smaller and weaker, which is consistent with the measured data tendency.

Finally, we present the experimental results of the fiber coupling efficiency for various incident polarizations and array periodic constants. The measured data (incident wavelength of 1560 nm) are shown in Fig. 5.15 (a) and (b). Here, the coupling efficiencies of the bare fiber are also tested and shown by the green dots, with no light signal detected at $\theta > 30°$.

Generally, for the nanodisk-enhanced fiber, there is no major efficiency difference between the s- and p-polarizations provided that the incidence

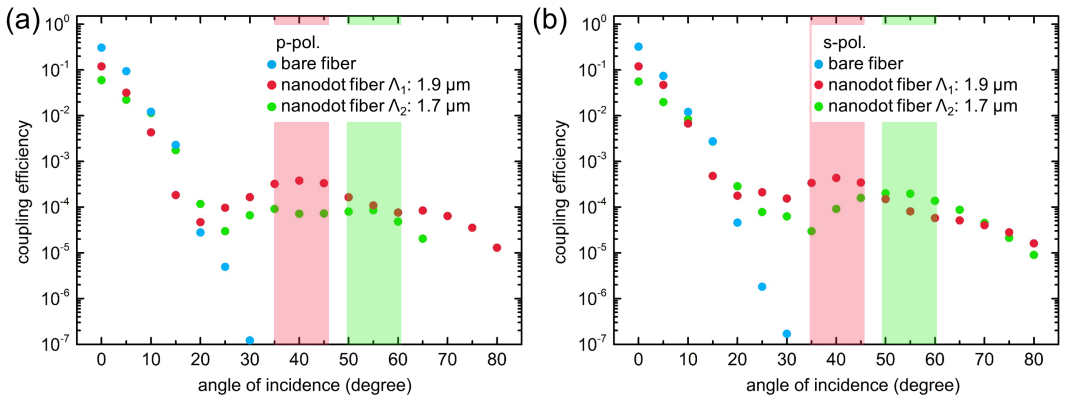

FIGURE 5.15
Fiber coupling efficiency at the wavelength of 1560 nm under p- and s-polarization. The red and green background colors highlight the additional enhancements for the corresponding experimental configurations.

plane is set along the same pitch direction, while the position of the additional enhancement (colored stripes) varies depending on the periodic constant. This pitch-induced efficiency difference is more distinct for s-polarized light in terms of the experimental data. As displayed in Fig. 5.15 (b), the red dots represent the fiber coupling along pitch Λ_1 (1.9 μm) and the green dots indicate measurements along pitch Λ_2 (1.7 μm). For the large pitch configuration, the secondary enhancement is located at approximately 40° (red background), while the small pitch enhancement shifts to approximately 55° (green background) with reduced amplitude. This experimental observation of pitch-induced efficiency variations is in accordance with the toy model and numerical calculations.

5.3.5 Further investigations to improve fiber NA

The simple nanodot array on fiber end face has proved that several orders improvement of light-coupling ability can be achieved owing to the plamonic resonance and grating-like structures. The next step should concentrate on the new design of nanostructures in order to further enhance light-collection performance. Probably starting from a single nano-particle (material is not limited to metallic, dielectic, graphene, etc.) could inspire these new designs. For example, assuming that merely one isolated gold particle is situated at the fiber core, deep investigations on its coupling efficiency (under wide-angle excitation) will be helpful to further design suitable nanostructures for real applications.

Even though the coupling efficiency of nanodots-enhanced fiber achieves a value on the order of 10^{-4} to 10^{-5}, it remains relative low to satisfy the urgent demands of many applications. As an example, in-vivo Raman imaging [206] commonly requires increasing coupling efficiency to levels such as 10^{-1} to 10^{-2}. The toy model suggests that such level improvement (especially at the incident angle from 40° to 80°) demands increasing the value of the diffraction efficiency a_{-1} in present case.

To reach such a high amplitude, the actively studied metalens may be a better candidate to be considered. Here, we summarize some of the recently demonstrated metalenses in Table 5.1.

TABLE 5.1
Potential structures to improve fiber light-collecting ability

Ref.	Material	Type	NA	Wavelength [nm]
[201]	Silicon	Dimer array	0.99	715
[202]	TiO_2	Nanopillars	0.94	500-650
[203]	TiO_2	Nanopillars	0.8	405, 532, 660
[207]	Silicon	Nanobricks	0.98(air), 1.48(n_{oil}=1.512)	532
[208]	Silicon	Nanoposts	0.97	1550

Based on these advancements, the fiber light-gathering capacity can be further boosted by applying an appropriate nanostructure, which will be an issue for further research.

5.4 Chapter summary

To verify the concept of a nanostructure-enhanced fiber, this chapter illustrates its optical characterization process and potential applications. We first examine the fundamental spectral response of a nanotrimer-modified SMF-28 fiber obtained using EBL. Comparative studies of a planar silica substrate and the optical fiber reveal the high spectral similarity of the two transmission contrasts, where a major dip is captured in both at approximately 1600 nm. This result proves that the property of the nanostructured fiber has been modified by the nanotrimer array, especially compared to the flat lineshape of a bare fiber.

We demonstrate two major applications of nanostructure-modified fibers, RI sensing and light collection. We employ a nanotrimer-enhanced fiber to detect surrounding index changes. The measured sensitivity reaches 390

nm/RIU, representing the highest value of the reported LSPR-based fiber sensors thus far [25].

In addition, a nanodisk-based fiber exhibits a several orders of magnitude improvement compared to the bare fiber in terms of the light-collecting efficiency at an incident angle from 30° to 80°. Further patterning with metalens-like nanostructures may enable real-world applications, such as random signal gathering, green photonics and endoscopy imaging.

Finally, we need to note that the concept of a nanostructure-enhanced fiber is not limited to either an SMF-28 fiber or metallic nanoantennas. In fact, this concept can apply to any type of fibers integrated with 2D or even 3D functional dielectric/metallic/hybrid structures. Therefore, a single-function standard fiber can be modified to be a versatile platform, be a short-cut tool for studying light-matter interaction and be used in real-world applications.

Chapter 6

Summary and outlook

6.1 Summary of the thesis

The study object of this thesis is nanostructure-enhanced fibers realized by electron beam lithography. This concept involves two principle research areas: plasmonics and fiber optics. The majority of the work is devoted to designing and characterizing subwavelength metallic structures. In particular, we study a closely distributed trimer array by numerical simulations and experimental characterizations. We observe a highly asymmetric lineshape with narrow transmission features situated at approximately 1600 nm. By inspecting simulated E-fields, we find that the formations of these features result from electric- and magnetic-based Fano resonances, in which a monomer-like mode interferes with a dimer-like mode. Furthermore, the trimer lattice exhibits a strong polarization dependence where a transmission dip can be changed into a peak at nearly the same wavelength by rotating the incident polarization from 0° to 90°. These advantages make the trimer array an ideal candidate for usage with SMF-28.

During experimental characterization of nanostructure-enhanced fibers, a main challenge (light-coupling to fibers) appears, which originates from the unique fiber substrate. In detail, this coupling problem is induced by the beam coupling from an objective/lens to bare fiber tips, which further leads to experimental condition mismatch between a reference fiber and a nanostructure-modified fiber. Owing to the coupling difficulty, the measured transmission spectrum cannot correctly represent the optical response, where the data error completely covers the true spectral features. Instead of transmission measurement, here, we propose to examine the spectral contrast (defined by two spectra obtained under two orthogonally polarized incident light beams) in order to reduce the measurement errors caused by the fiber coupling problem.

We also successfully demonstrate the fabrication of nanostructures on fiber facets. Another major challenge occurs since the fiber cannot match current EBL-based devices owing to its small cross-section and high aspect ratio. Therefore, we develop a flat metallic can-like holder to place fiber facets on its top surface. In this way, we can planarize the fiber surface. The fabricated well-defined nanostructures on the fiber end face strongly confirm the reliability and reproducibility of this manufacturing technique. This approach can also be applied to almost any type of e-beam lithography machine and any type of nanostructure that has been implemented with this infrastructure, opening up the entire field of nanotechnology for fiber optics.

Finally, we demonstrate that nanostructure-enhanced fibers can be employed as an RI sensor and a large-angle light signal detector. The former represents the state-of-the-art in terms of LSPR-based fiber RI sensitivity (approximately 390 nm/RIU), and the latter allows gathering light at incident angles up to 80°, where bare fibers fail to operate. Two application examples illustrate the enormous potential of nanostructure-functionalized fiber tips for real-world usage.

Through the entire thesis, we hope to provide an explicit research process from the perspectives of a fundamental understanding (plasmonics and fiber optics) and the implementation of metallic nanostructures towards the demonstration of practical usage of nanostructure-enhanced fibers. In conclusion, the studies of plasmonic-structure-modified optical fibers pave a new way to realize in-fiber optical devices.

6.2 Outlook of future work

In the last section of this thesis, perspectives on nanostructure-enhanced fibers are presented from the aspects of (1) nanostructure design, (2) nanofabrication on fibers and (3) potential applications. Here, we hope to provide a general blueprint of the project and welcome any feedback on this study.

- Nanostructure design and optimization

Design acceleration by deep learning

As summarized above, a major challenge of this project is to design nanostructures with the desired spectral response (asymmetric lineshape with high polarization sensitivity). To obtain an accurate far-field optical response, time-consuming numerical simulations based on the FEM are adopted in this

work. In these simulation models, a common working process is to solve the full set of Maxwell's equations at selected wavelengths. To match the true array arrangement, the excitation and boundary conditions need to be carefully considered. Further optimization of nanostructures repeats this procedure, and comparative experimental studies are also necessary.

Recently, several studies [174, 209] have revealed a novel plasmonic nanostructure design and characterization method using artificial intelligence (computer science). Specifically, deep neural networks can be utilized to predict and optimize the spectral behavior of metasurface-based nanoelements [174]. Therefore, deep learning could provide an alternative and time-efficient approach for designing nanostructures with a targeted optical response to satisfy application requirements.

Inverse-design of nanostructures/metasurface

As illustrated in chapter 3, the design of a nanostructure with the desired optical response (e.g., asymmetric spectral lineshape) is an iterative and time-consuming process. Normally, the workflow involves guessing a structure, solving Maxwell's equations, characterizing the optical properties and repeating these procedures until the structure meets the demands of real applications.

Recently, the first 'inverse-design' software for optical metamaterial design was released [210]. The inverse design lets users start by inputting the desired optical response, and the computer will take over the 'guesswork' with the help of an installed nanostructure library. Finally, the software will produce corresponding nanoantennas for fabrication. This inverse design process reduces the numerous efforts and time to enable urgent prototyping of nanostructure-inspired components.

- Fabrication techniques on fibers

Optical/laser printing

Optical printing can realize single nanoparticle manipulations with a focused Gaussian beam [211, 212]. Generally, the optical/laser printing process employs optical forces ($\propto \nabla|E|^2$) to trap and move nanoparticles. At the target position, this process can place and fix particles by van der Waals attraction forces. The latest demonstrations show that this approach can be used to assemble spherical gold nanoparticles [211], nanorods [213], and bipyramids [214]. There is no limitation on extending this method to nonmetallic nanoparticles. Compared with EBL, the major advantages of optical printing

are the low-cost instruments and the loose environmental requirements (e.g., no hard request of clean rooms).

Here, we suggest using optical printing for fiber-substrate nanoparticle assembly. Since there are fewer geometric limitations of the substrates, this method can be directly applied to the fiber facet.

- Potential applications

Mode-selective fibers for telecommunication

Optical fiber plays an extremely important role in the modern telecommunication industry. Over the past half century, fundamental studies and technological breakthroughs have increased the fiber data-transporting capacity approximately tenfold every four years [215].

However, the maximum data transmission capacity (approximately 100 Tbit/s) of SMFs in worldwide communication networks is estimated to reach the upper limit in the foreseeable future [215]. To solve this bottleneck, next generation techniques suggest using multimode fibers or few-mode fibers (FMFs) to realize mode-division multiplexing (MDM) or space-division multiplexing (SDM) [215, 216]. Generally, MDM refers to establishing several spatially distinguishable or mode-based data paths through a fiber to satisfy the exponential growth in capacity demand.

Here, we propose a mode-selective metasurface-modified fiber for MDM usage. The concept is to implement mode-converter metasurfaces [217] on the facet of MMFs/FMFs for data transport. This type of metasurface employs elliptical cross-section silicon nanopillars as resonance elements to manipulate the incident light phase. By carefully arranging the nanopillar distribution, the functionalized interface can convert a Gaussian-like incident beam to the desired fiber mode (e.g., LP_{11} mode) [217]. The latest studies [218, 219] on dielectric metasurfaces, in which the metasurface is fabricated on a silica substrate, demonstrate the high working efficiency (> 90%) and potential applications in free space communication. Apparently, the mode-selective fiber should support several modes, indicating that SMF-28 is not an ideal candidate.

Bioanalytics: Endoscopy-like imaging

Currently, optical fiber-based devices are increasingly being used for human health monitoring due to their numerous advantages, such as flexibility, adjustable length and small diameter [220]. The wide-field endoscopic imaging enabled by fibers is regarded as a promising application in biophotonics

since it is free of electronic interference and fiber small volume can reduce the surgery operation space in human bodies [206].

Here, we propose to place a metalens on SMFs or MMFs for remote imaging. For instance, Amir Arbabi *et al*. demonstrated a dielectric metalens with a maximum working efficiency of 97% [18]. Based on elliptical nanoposts, complete control of the light phase and polarization can be achieved. By patterning fibers with this type of metalens, fiber-based *in vivo* disease diagnosis should be achievable.

Bibliography

1. Agrawal, G. P. *Fiber-optic communication systems* (John Wiley & Sons, 2012).
2. Snyder, A. W. & Love, J. *Optical waveguide theory* (Springer Science & Business Media, 2012).
3. Gambling, W. The rise and rise of optical fibers. *IEEE Journal of Selected Topics in Quantum Electronics* **6,** 1084–1093 (2000).
4. NobelPrize.org. *The Nobel Prize in Physics 2009* Last accessed Mon. 4 Feb 2019. 2009. https://www.nobelprize.org/prizes/physics/2009/summary/.
5. Birks, T. A., Knight, J. C. & Russell, P. S. J. Endlessly single-mode photonic crystal fiber. *Optics Letters* **22,** 961–963 (1997).
6. Russell, P. Photonic crystal fibers. *Science* **299,** 358–362 (2003).
7. Schmidt, M. A., Alexander, A. & Fabien, S. Hybrid optical fibers- an Innovative platform for in-Fiber photonic devices. *Advanced Optical Materials* **4,** 13–36 (2016).
8. Doherty, B. *et al.* Nanoparticle functionalised small-core suspended-core fibre–a novel platform for efficient sensing. *Biomedical Optics Express* **8,** 790–799 (2017).
9. Chemnitz, M. *et al.* Hybrid soliton dynamics in liquid-core fibres. *Nature Communications* **8,** 42 (2017).
10. Noda, J., Okamoto, K. & Sasaki, Y. Polarization-maintaining fibers and their applications. *Journal of Lightwave Technology* **4,** 1071–1089 (1986).
11. Leite, I. T. *et al.* Three-dimensional holographic optical manipulation through a high-numerical-aperture soft-glass multimode fibre. *Nature Photonics* **12,** 33 (2018).
12. Buczyński, R. *et al.* Optical fibers with gradient index nanostructured core. *Optics Express* **23,** 25588–25596 (2015).
13. Novotny, L. & Hecht, B. *Principles of nano-optics* (Cambridge University Press, 2012).

14. Maier, S. A. *Plasmonics: fundamentals and applications* (Springer Science & Business Media, 2007).

15. Yu, N. *et al.* Light propagation with phase discontinuities: generalized laws of reflection and refraction. *Science* **334,** 333–337 (2011).

16. Zeisberger, M., Schneidewind, H., Huebner, U., Popp, J. & Schmidt, M. A. Nanoboomerang-based inverse metasurfaces — a promising path towards ultrathin photonic devices for transmission operation. *APL Photonics* **2,** 036102 (2017).

17. Meinzer, N., Barnes, W. L. & Hooper, I. R. Plasmonic meta-atoms and metasurfaces. *Nature Photonics* **8,** 889 (2014).

18. Arbabi, A., Horie, Y., Bagheri, M. & Faraon, A. Dielectric metasurfaces for complete control of phase and polarization with subwavelength spatial resolution and high transmission. *Nature Nanotechnology* **10,** 937–943 (2015).

19. Tittl, A. *et al.* Imaging-based molecular barcoding with pixelated dielectric metasurfaces. *Science* **360,** 1105–1109 (2018).

20. Wang, K. *et al.* Quantum metasurface for multiphoton interference and state reconstruction. *Science* **361,** 1104–1108 (2018).

21. Nazemosadat, E. *et al.* Dielectric broadband metasurfaces for fiber mode-multiplexed communications. *Advanced Optical Materials,* 1801679 (2019).

22. Inc., C. *Product Information of Corning SMF-28* Last accessed Mon. 4 Feb 2019. 2014. https://www.corning.com/media/worldwide/coc/documents/Fiber/PI1424_11-14.pdf.

23. Taminiau, T. H., Moerland, R. J., Segerink, F. B., Kuipers, L. & van Hulst, N. F. $\lambda/4$ resonance of an optical monopole antenna probed by single molecule fluorescence. *Nano Letters* **7,** 28–33 (2007).

24. Consales, M. *et al.* Lab-on-fiber technology: toward multifunctional optical nanoprobes. *ACS Nano* **6,** 3163–3170 (2012).

25. Wang, N., Zeisberger, M., Hübner, U. & Schmidt, M. A. Nanotrimer enhanced optical fiber tips implemented by electron beam lithography. *Optical Materials Express* **8,** 2246–2255 (2018).

26. Yang, J. *et al.* Photonic crystal fiber metalens. *Nanophotonics* **8,** 443–449 (2019).

27. Lin, Y., Guo, J. & Lindquist, R. G. Demonstration of an ultra-wideband optical fiber inline polarizer with metal nano-grid on the fiber tip. *Optics Express* **17,** 17849–17854 (2009).

28. Principe, M. *et al.* Optical fiber meta-tips. *Light: Science & Applications* **6,** e16226 (2017).

29. Jia, P., Yang, Z., Yang, J. & Ebendorff-Heidepriem, H. Quasiperiodic nanohole arrays on optical fibers as plasmonic sensors: Fabrication and sensitivity determination. *ACS Sensors* **1,** 1078–1083 (2016).

30. Prasciolu, M. *et al.* Design and fabrication of on-fiber diffractive elements for fiber-waveguide coupling by means of e-beam lithography. *Microelectronic Engineering* **67,** 169–174 (2003).

31. Xomalis, A. *et al.* Fibre-optic metadevice for all-optical signal modulation based on coherent absorption. *Nature Communications* **9,** 182 (2018).

32. Horák, M. *et al.* Comparative study of plasmonic antennas fabricated by electron beam and focused ion beam lithography. *Scientific Reports* **8,** 9640 (2018).

33. Bruchhaus, L. *et al.* Comparison of technologies for nano device prototyping with a special focus on ion beams: a review. *Applied Physics Reviews* **4,** 011302 (2017).

34. Tuniz, A., Chemnitz, M., Dellith, J., Weidlich, S. & Schmidt, M. A. Hybrid-mode-assisted long-distance excitation of short-range surface plasmons in a nanotip-enhanced step-index fiber. *Nano Letters* **17,** 631–637 (2017).

35. Publication, O. *OSA Spotlight on Optics* Last accessed Mon. 4 Feb 2019. 2019. https://www.osapublishing.org/spotlight/summary.cfm?id=395430.

36. Scaravilli, M. *et al.* Excitation of bloch surface waves on an optical fiber tip. *Advanced Optical Materials* **6,** 1800477 (2018).

37. Lin, Y., Zou, Y., Mo, Y., Guo, J. & Lindquist, R. G. E-beam patterned gold nanodot arrays on optical fiber tips for localized surface plasmon resonance biochemical sensing. *Sensors* **10,** 9397–9406 (2010).

38. Wei, J., Zeng, Z. & Lin, Y. Localized surface plasmon resonance (LSPR)-coupled fiber-optic nanoprobe for the detection of protein biomarkers. *Biosensors and Biodetection: Methods and Protocols Volume 1: Optical-Based Detectors*, 1–14 (2017).

39. Sanders, M., Lin, Y., Wei, J., Bono, T. & Lindquist, R. G. An enhanced LSPR fiber-optic nanoprobe for ultrasensitive detection of protein biomarkers. *Biosensors and Bioelectronics* **61,** 95–101 (2014).

40. Kaye, S. *et al.* Label-free detection of DNA hybridization with a compact LSPR-based fiber-optic sensor. *Analyst* **142,** 1974–1981 (2017).

41. Feng, S., Darmawi, S., Henning, T., Klar, P. J. & Zhang, X. A miniaturized sensor consisting of concentric metallic nanorings on the end facet of an optical fiber. *Small* **8,** 1937–1944 (2012).

42. Jia, P. & Yang, J. A plasmonic optical fiber patterned by template transfer as a high-performance flexible nanoprobe for real-time biosensing. *Nanoscale* **6,** 8836–8843 (2014).

43. Ricciardi, A. *et al.* Versatile optical fiber nanoprobes: from plasmonic biosensors to polarization-sensitive devices. *ACS Photonics* **1,** 69–78 (2013).

44. Lipomi, D. J. *et al.* Patterning the tips of optical fibers with metallic nanostructures using nanoskiving. *Nano Letters* **11,** 632–636 (2010).

45. Luk'yanchuk, B. *et al.* The Fano resonance in plasmonic nanostructures and metamaterials. *Nature Materials* **9,** 707 (2010).

46. Lin, Y., Zou, Y. & Lindquist, R. G. A reflection-based localized surface plasmon resonance fiber-optic probe for biochemical sensing. *Biomedical Optics Express* **2,** 478–484 (2011).

47. Zhu, X., Feng, L., Zhang, P., Yin, X. & Zhang, X. One-way invisible cloak using parity-time symmetric transformation optics. *Optics Letters* **38,** 2821–2824 (2013).

48. Valentine, J., Li, J., Zentgraf, T., Bartal, G. & Zhang, X. An optical cloak made of dielectrics. *Nature Materials* **8,** 568 (2009).

49. Lin, D., Fan, P., Hasman, E. & Brongersma, M. L. Dielectric gradient metasurface optical elements. *Science* **345,** 298–302 (2014).

50. Kennedy, L. C. *et al.* A new era for cancer treatment: gold-nanoparticle-mediated thermal therapies. *Small* **7,** 169–183 (2011).

51. Wang, L. *et al.* Grayscale transparent metasurface holograms. *Optica* **3,** 1504–1505 (2016).

52. Grigorenko, A., Polini, M. & Novoselov, K. Graphene plasmonics. *Nature Photonics* **6,** 749 (2012).

53. Ebbesen, T. W., Lezec, H. J., Ghaemi, H., Thio, T. & Wolff, P. Extraordinary optical transmission through sub-wavelength hole arrays. *Nature* **391,** 667 (1998).

54. Giannini, V., Fernández-Domínguez, A. I., Heck, S. C. & Maier, S. A. Plasmonic nanoantennas: fundamentals and their use in controlling the radiative properties of nanoemitters. *Chemical Reviews* **111,** 3888–3912 (2011).

55. Johnson, P. B. & Christy, R.-W. Optical constants of the noble metals. *Physical Review B* **6,** 4370 (1972).

56. Rakić, A. D., Djurišić, A. B., Elazar, J. M. & Majewski, M. L. Optical properties of metallic films for vertical-cavity optoelectronic devices. *Applied Optics* **37,** 5271–5283 (1998).

57. Encyclopedia, R. P. *Silica Fibers* Last accessed Mon. 4 Feb 2019. 2019. https://www.rp-photonics.com/silica_fibers.html.

58. Sellmeier, W. Zur Erkarung der abnormen Farbenfolge im Spectrum einiger. Substanzen. *Annalen der Physik und Chemie* **219,** 272–282 (1871).

59. RefractiveIndex.INFO. *Optical constants of Fused silica (fused quartz)* Last accessed Mon. 4 Feb 2019. 2019. https://refractiveindex.info/?shelf=glass&book=fused_silica&page=Malitson.

60. Kirchain, R. & Kimerling, L. A roadmap for nanophotonics. *Nature Photonics* **1,** 303 (2007).

61. Stockman, M. I. *et al.* Roadmap on plasmonics. *Journal of Optics* **20,** 043001 (2018).

62. Kauranen, M. & Zayats, A. V. Nonlinear plasmonics. *Nature Photonics* **6,** 737 (2012).

63. Pile, D. & Krenn, J. *Perspective on plasmonics* 2012.

64. Törmä, P. & Barnes, W. L. Strong coupling between surface plasmon polaritons and emitters: a review. *Reports on Progress in Physics* **78,** 013901 (2014).

65. Barnes, W. L., Dereux, A. & Ebbesen, T. W. Surface plasmon subwavelength optics. *Nature* **424,** 824 (2003).

66. Kawata, S., Inouye, Y. & Verma, P. Plasmonics for near-field nano-imaging and superlensing. *Nature Photonics* **3,** 388 (2009).

67. Oulton, R. F., Sorger, V. J., Genov, D., Pile, D. & Zhang, X. A hybrid plasmonic waveguide for subwavelength confinement and long-range propagation. *Nature Photonics* **2,** 496 (2008).

68. Stockman, M. I. Nanofocusing of optical energy in tapered plasmonic waveguides. *Physical Review Letters* **93,** 137404 (2004).

69. Schuller, J. A. *et al.* Plasmonics for extreme light concentration and manipulation. *Nature Materials* **9,** 193 (2010).

70. Pang, L., Hwang, G. M., Slutsky, B. & Fainman, Y. Spectral sensitivity of two-dimensional nanohole array surface plasmon polariton resonance sensor. *Applied Physics Letters* **91,** 123112 (2007).

71. Guo, X. *et al.* Direct coupling of plasmonic and photonic nanowires for hybrid nanophotonic components and circuits. *Nano Letters* **9,** 4515–4519 (2009).

72. Dai, W.-H., Lin, F.-C., Huang, C.-B. & Huang, J.-S. Mode conversion in high-definition plasmonic optical nanocircuits. *Nano Letters* **14,** 3881–3886 (2014).

73. Schneidewind, H., Zeisberger, M., Plidschun, M., Weidlich, S. & Schmidt, M. A. Photonic candle - focusing light using nano-bore optical fibers. *Optics Express* **26,** 31706–31716 (2018).

74. Lee, H. *et al.* Pressure-assisted melt-filling and optical characterization of Au nano-wires in microstructured fibers. *Optics Express* **19,** 12180–12189 (2011).

75. Tuniz, A. & Schmidt, M. A. Interfacing optical fibers with plasmonic nanoconcentrators. *Nanophotonics.*

76. Uebel, P., Bauerschmidt, S. T., Schmidt, M. A. & St. J. Russell, P. A gold-nanotip optical fiber for plasmon-enhanced near-field detection. *Applied Physics Letters* **103,** 021101 (2013).

77. Marini, A. *et al.* Ultrafast nonlinear dynamics of surface plasmon polaritons in gold nanowires due to the intrinsic nonlinearity of metals. *New Journal of Physics* **15,** 013033 (2013).

78. Mayer, K. M. & Hafner, J. H. Localized surface plasmon resonance sensors. *Chemical Reviews* **111,** 3828–3857 (2011).

79. Brongersma, M. L. & Kik, P. G. *Surface plasmon nanophotonics* (Springer, 2007).

80. Shalaev, V. M. & Kawata, S. *Nanophotonics with surface plasmons* (Elsevier, 2006).

81. Willets, K. A. & Van Duyne, R. P. Localized surface plasmon resonance spectroscopy and sensing. *Annual Review of Physical Chemistry* **58,** 267–297 (2007).

82. Mock, J., Barbic, M., Smith, D., Schultz, D. & Schultz, S. Shape effects in plasmon resonance of individual colloidal silver nanoparticles. *The Journal of Chemical Physics* **116,** 6755–6759 (2002).

83. Mie, G. Beiträge zur Optik trüber Medien, speziell kolloidaler Metallösungen. *Annalen der Physik* **330,** 377–445 (1908).

84. Kuwata, H., Tamaru, H., Esumi, K. & Miyano, K. Resonant light scattering from metal nanoparticles: Practical analysis beyond Rayleigh approximation. *Applied Physics Letters* **83,** 4625–4627 (2003).

85. Yu, R., Liz-Marzán, L. M. & de Abajo, F. J. G. Universal analytical modeling of plasmonic nanoparticles. *Chemical Society Reviews* **46,** 6710–6724 (2017).

86. Amendola, V., Pilot, R., Frasconi, M., Marago, O. M. & Iati, M. A. Surface plasmon resonance in gold nanoparticles: a review. *Journal of Physics: Condensed Matter* **29,** 203002 (2017).

87. Hulst, H. C. & van de Hulst, H. C. *Light scattering by small particles* (Courier Corporation, 1981).

88. Tan, S. J. *et al.* Plasmonic color palettes for photorealistic printing with aluminum nanostructures. *Nano Letters* **14,** 4023–4029 (2014).

89. Olson, J. *et al.* Vivid, full-color aluminum plasmonic pixels. *Proceedings of the National Academy of Sciences* **111,** 14348–14353 (2014).

90. Sun, Y. & Xia, Y. Gold and silver nanoparticles: a class of chromophores with colors tunable in the range from 400 to 750 nm. *Analyst* **128,** 686–691 (2003).

91. Duan, X. & Liu, N. Scanning plasmonic color display. *ACS Nano* **12,** 8817–8823 (2018).

92. Rechberger, W. *et al.* Optical properties of two interacting gold nanoparticles. *Optics Communications* **220,** 137–141 (2003).

93. Huang, W., Qian, W., Jain, P. K. & El-Sayed, M. A. The effect of plasmon field on the coherent lattice phonon oscillation in electron-beam fabricated gold nanoparticle pairs. *Nano Letters* **7,** 3227–3234 (2007).

94. Jain, P. K., Huang, W. & El-Sayed, M. A. On the universal scaling behavior of the distance decay of plasmon coupling in metal nanoparticle pairs: a plasmon ruler equation. *Nano Letters* **7,** 2080–2088 (2007).

95. Tabor, C., Murali, R., Mahmoud, M. & El-Sayed, M. A. On the use of plasmonic nanoparticle pairs as a plasmon ruler: the dependence of the near-field dipole plasmon coupling on nanoparticle size and shape. *The Journal of Physical Chemistry A* **113,** 1946–1953 (2008).

96. Liu, N., Hentschel, M., Weiss, T., Alivisatos, A. P. & Giessen, H. Three-dimensional plasmon rulers. *Science* **332,** 1407–1410 (2011).

97. Ben, X. & Park, H. S. Size dependence of the plasmon ruler equation for two-dimensional metal nanosphere arrays. *The Journal of Physical Chemistry C* **115,** 15915–15926 (2011).

98. Auguié, B. & Barnes, W. L. Collective resonances in gold nanoparticle arrays. *Physical Review Letters* **101,** 143902 (2008).

99. Rodriguez, S. R. K. *et al.* Coupling bright and dark plasmonic lattice resonances. *Physical Review X* **1,** 021019 (2011).

100. Kravets, V., Schedin, F. & Grigorenko, A. Extremely narrow plasmon resonances based on diffraction coupling of localized plasmons in arrays of metallic nanoparticles. *Physical Review Letters* **101,** 087403 (2008).

101. Guo, R., Hakala, T. K. & Törmä, P. Geometry dependence of surface lattice resonances in plasmonic nanoparticle arrays. *Physical Review B* **95,** 155423 (2017).

102. Humphrey, A. D. & Barnes, W. L. Plasmonic surface lattice resonances on arrays of different lattice symmetry. *Physical Review B* **90,** 075404 (2014).

103. Wang, D., Yang, A., Hryn, A. J., Schatz, G. C. & Odom, T. W. Superlattice plasmons in hierarchical Au nanoparticle arrays. *ACS Photonics* **2,** 1789–1794 (2015).

104. Kataja, M. *et al.* Surface lattice resonances and magneto-optical response in magnetic nanoparticle arrays. *Nature Communications* **6,** 7072 (2015).

105. Humphrey, A. & Barnes, W. Plasmonic surface lattice resonances in arrays of metallic nanoparticle dimers. *Journal of Optics* **18,** 035005 (2016).

106. Humphrey, A. D., Meinzer, N., Starkey, T. A. & Barnes, W. L. Surface lattice resonances in plasmonic arrays of asymmetric disc dimers. *ACS Photonics* **3,** 634–639 (2016).

107. Michaeli, L., Keren-Zur, S., Avayu, O., Suchowski, H. & Ellenbogen, T. Nonlinear surface lattice resonance in plasmonic nanoparticle arrays. *Physical Review Letters* **118,** 243904 (2017).

108. Li, Z., Butun, S. & Aydin, K. Ultranarrow band absorbers based on surface lattice resonances in nanostructured metal surfaces. *ACS Nano* **8,** 8242–8248 (2014).

109. Vecchi, G., Giannini, V. & Rivas, J. G. Shaping the fluorescent emission by lattice resonances in plasmonic crystals of nanoantennas. *Physical Review Letters* **102,** 146807 (2009).

110. Shi, L. *et al.* Spatial coherence properties of organic molecules coupled to plasmonic surface lattice resonances in the weak and strong coupling regimes. *Physical Review Letters* **112,** 153002 (2014).

111. Fano, U. Effects of configuration interaction on intensities and phase shifts. *Physical Review* **124,** 1866 (1961).

112. Limonov, M. F., Rybin, M. V., Poddubny, A. N. & Kivshar, Y. S. Fano resonances in photonics. *Nature Photonics* **11,** 543 (2017).

113. Miroshnichenko, A. E., Flach, S. & Kivshar, Y. S. Fano resonances in nanoscale structures. *Reviews of Modern Physics* **82,** 2257 (2010).

114. Francescato, Y., Giannini, V. & Maier, S. A. Plasmonic systems unveiled by Fano resonances. *ACS Nano* **6,** 1830–1838 (2012).

115. Gallinet, B. & Martin, O. J. Influence of electromagnetic interactions on the line shape of plasmonic Fano resonances. *ACS Nano* **5,** 8999–9008 (2011).

116. Giannini, V., Francescato, Y., Amrania, H., Phillips, C. C. & Maier, S. A. Fano resonances in nanoscale plasmonic systems: a parameter-free modeling approach. *Nano Letters* **11,** 2835–2840 (2011).

117. Lovera, A., Gallinet, B., Nordlander, P. & Martin, O. J. Mechanisms of Fano resonances in coupled plasmonic systems. *ACS Nano* **7,** 4527–4536 (2013).

118. Lassiter, J. B. *et al.* Designing and deconstructing the Fano lineshape in plasmonic nanoclusters. *Nano Letters* **12,** 1058–1062 (2012).

119. Ghatak, A. & Thyagarajan, K. *An introduction to fiber optics* (Cambridge university press, 1998).

120. Inc., N. *Fiber optic basics* Last accessed Mon. 4 Feb 2019. 2019. https://www.newport.com/t/fiber-optic-basics.

121. Krohn, D. A., MacDougall, T. & Mendez, A. *Fiber optic sensors: fundamentals and applications* (Spie Press Bellingham, WA, 2014).

122. Saleh, B. E., Teich, M. C. & Saleh, B. E. *Fundamentals of photonics* (Wiley New York, 1991).

123. Inc., T. *Multimode fiber tutorial* Last accessed Mon. 4 Feb 2019. 2019. https://www.thorlabs.com/newgrouppage9.cfm?objectgroup_id=10417.

124. Buck, J. A. *Fundamentals of optical fibers* (John Wiley & Sons, 2004).

125. Digonnet, M. J. *et al.* Rare-earth-doped fiber lasers and amplifiers (2001).

126. Desurvire, E. *Erbium-doped fiber amplifiers: principles and applications* (Wiley New York, 1994).

127. Doherty, B. *et al.* Plasmonic nanoparticle-functionalized exposed-core fiber—An optofluidic refractive index sensing platform. *Optics Letters* **42,** 4395–4398 (2017).

128. Saar, B. G., Johnston, R. S., Freudiger, C. W., Xie, X. S. & Seibel, E. J. Coherent Raman scanning fiber endoscopy. *Optics Letters* **36,** 2396–2398 (2011).

129. Kay, G. N. *Fiber optics in architectural lighting: methods, design, and applications* (McGraw-Hill New York, NY, 1999).

130. Schmidt, M. A., Lei, D. Y., Wondraczek, L., Nazabal, V. & Maier, S. A. Hybrid nanoparticle–microcavity-based plasmonic nanosensors with improved detection resolution and extended remote-sensing ability. *Nature Communications* **3,** 1108 (2012).

131. Faez, S. *et al.* Fast, label-free tracking of single viruses and weakly scattering nanoparticles in a nanofluidic optical fiber. *ACS Nano* **9,** 12349–12357 (2015).

132. Morton, S. M., Silverstein, D. W. & Jensen, L. Theoretical studies of plasmonics using electronic structure methods. *Chemical Reviews* **111,** 3962–3994 (2011).

133. Prodan, E., Radloff, C., Halas, N. J. & Nordlander, P. A hybridization model for the plasmon response of complex nanostructures. *Science* **302,** 419–422 (2003).

134. Wang, N., Zeisberger, M., Hübner, U., Giannini, V. & Schmidt, M. A. Symmetry-breaking induced magnetic Fano resonances in densely packed arrays of symmetric nanotrimers. *Scientific Reports* **9,** 2873 (2019).

135. Inc., C. *Create RF, Microwave, and Millimeter-Wave Designs with the RF Module* Last accessed Mon. 4 Feb 2019. 2019. www.comsol.com/rf-module.

136. Inc., L. *High-Performance Nanophotonic Simulation Software* Last accessed Mon. 4 Feb 2019. 2019. https://www.lumerical.com/.

137. GmbH, D. S. D. *CST MICROWAVE STUDIO 3D EM Simulation Software* Last accessed Mon. 15 April 2019. 2019. https://www.cst.com/products.

138. MeepFDTD. *Manual - MEEP Documentation* Last accessed Mon. 4 Feb 2019. 2019. https://meep.readthedocs.io/en/latest/.

139. Toolbox, M. *MNPBEM Toolbox* Last accessed Mon. 4 Feb 2019. 2019. http://physik.uni-graz.at/~uxh/mnpbem/html/mnpbem_product_page.html.

140. DDSCAT. *DDSCAT* Last accessed Mon. 4 Feb 2019. 2019. http://ddscat.wikidot.com/.

141. Zienkiewicz, O. C., Taylor, R. L., Zienkiewicz, O. C. & Taylor, R. L. *The finite element method* (McGraw-hill London, 1977).

142. Imura, K., Nagahara, T. & Okamoto, H. Near-field two-photon-induced photoluminescence from single gold nanorods and imaging of plasmon modes. *The Journal of Physical Chemistry B* **109,** 13214–13220 (2005).

143. Park, J. *et al.* Two-photon-induced photoluminescence imaging of tumors using near-infrared excited gold nanoshells. *Optics Express* **16,** 1590–1599 (2008).

144. Hohenester, U., Ditlbacher, H. & Krenn, J. R. Electron-energy-loss spectra of plasmonic nanoparticles. *Physical Review Letters* **103,** 106801 (2009).

145. Vesseur, E. J. R., de Waele, R., Kuttge, M. & Polman, A. Direct observation of plasmonic modes in Au nanowires using high-resolution cathodoluminescence spectroscopy. *Nano Letters* **7,** 2843–2846 (2007).

146. Poeggel, S. *et al.* Optical fibre pressure sensors in medical applications. *Sensors* **15,** 17115–17148 (2015).

147. Ecke, W., Latka, I., Willsch, R., Reutlinger, A. & Graue, R. Fibre optic sensor network for spacecraft health monitoring. *Measurement Science and Technology* **12,** 974 (2001).

148. Barták, J. *et al.* Analysis of viscosity data in As2Se3, Se and Se95Te5 chalcogenide melts using the pressure assisted melt filling technique. *Journal of Non-Crystalline Solids* **511,** 100–108 (2019).

149. Kostovski, G., Stoddart, P. R. & Mitchell, A. The optical fiber tip: an inherently light-Coupled microscopic platform for micro-and nanotechnologies. *Advanced Materials* **26,** 3798–3820 (2014).

150. Zoric, I., Zäch, M., Kasemo, B. & Langhammer, C. Gold, platinum, and aluminum nanodisk plasmons: material independence, subradiance, and damping mechanisms. *ACS Nano* **5,** 2535–2546 (2011).

151. Sinzinger, S. & Jahns, J. *Microoptics* (John Wiley & Sons, 2006).

152. Huebner, U. *et al. Multi-stencil character projection e-beam lithography: a fast and flexible way for high quality optical metamaterials* in *30th European Mask and Lithography Conference* **9231** (2014), 92310E.

153. Fang, Z. *et al.* Removing a wedge from a metallic nanodisk reveals a Fano resonance. *Nano Letters* **11,** 4475–4479 (2011).

154. Zhang, S. *et al.* Pronounced Fano resonance in single gold split nanodisks with 15 nm split gaps for intensive second harmonic generation. *ACS Nano* **10,** 11105–11114 (2016).

155. Verellen, N. *et al.* Fano resonances in individual coherent plasmonic nanocavities. *Nano Letters* **9,** 1663–1667 (2009).

156. Yan, J. *et al.* Directional Fano resonance in a silicon nanosphere dimer. *ACS Nano* **9,** 2968–2980 (2015).

157. Yan, C. & Martin, O. J. Periodicity-induced symmetry breaking in a fano lattice: hybridization and tight-binding regimes. *ACS Nano* **8,** 11860–11868 (2014).

158. Fan, J. A. *et al.* Fano-like interference in self-assembled plasmonic quadrumer clusters. *Nano Letters* **10,** 4680–4685 (2010).

159. Hentschel, M. *et al.* Transition from isolated to collective modes in plasmonic oligomers. *Nano Letters* **10,** 2721–2726 (2010).

160. Hentschel, M., Dregely, D., Vogelgesang, R., Giessen, H. & Liu, N. Plasmonic oligomers: the role of individual particles in collective behavior. *ACS Nano* **5,** 2042–2050 (2011).

161. Miroshnichenko, A. E. & Kivshar, Y. S. Fano resonances in all-dielectric oligomers. *Nano Letters* **12,** 6459–6463 (2012).

162. Fan, J. A. *et al.* Self-assembled plasmonic nanoparticle clusters. *Science* **328,** 1135–1138 (2010).

163. Sheikholeslami, S. N., García-Etxarri, A. & Dionne, J. A. Controlling the interplay of electric and magnetic modes via Fano-like plasmon resonances. *Nano Letters* **11,** 3927–3934 (2011).

164. Nazir, A. *et al.* Fano coil-type resonance for magnetic hot-spot generation. *Nano Letters* **14,** 3166–3171 (2014).

165. Panaro, S. *et al.* Plasmonic moon: a Fano-like approach for squeezing the magnetic field in the infrared. *Nano Letters* **15,** 6128–6134 (2015).

166. Yang, D.-J. *et al.* Magnetic Fano resonance-induced second-harmonic generation enhancement in plasmonic metamolecule rings. *Nanoscale* **9,** 6068–6075 (2017).

167. Alegret, J. *et al.* Plasmonic properties of silver trimers with trigonal symmetry fabricated by electron-beam lithography. *The Journal of Physical Chemistry C* **112,** 14313–14317 (2008).

168. Chuntonov, L. & Haran, G. Trimeric plasmonic molecules: the role of symmetry. *Nano Letters* **11,** 2440–2445 (2011).

169. Chuntonov, L. & Haran, G. Effect of symmetry breaking on the mode structure of trimeric plasmonic molecules. *The Journal of Physical Chemistry C* **115,** 19488–19495 (2011).

170. Abasahl, B., Santschi, C. & Martin, O. J. Quantitative extraction of equivalent lumped circuit elements for complex plasmonic nanostructures. *ACS Photonics* **1,** 403–407 (2014).

171. Artar, A., Yanik, A. A. & Altug, H. Directional double Fano resonances in plasmonic hetero-oligomers. *Nano Letters* **11,** 3694–3700 (2011).

172. Liu, Z. & Ye, J. Highly controllable double Fano resonances in plasmonic metasurfaces. *Nanoscale* **8,** 17665–17674 (2016).

173. Brandl, D. W., Mirin, N. A. & Nordlander, P. Plasmon modes of nanosphere trimers and quadrumers. *The Journal of Physical Chemistry B* **110,** 12302–12310 (2006).

174. Malkiel, I. *et al.* Plasmonic nanostructure design and characterization via Deep Learning. *Light: Science & Applications* **7,** 60 (2018).

175. Galeotti, F., Pisco, M. & Cusano, A. Self-assembly on optical fibers: a powerful nanofabrication tool for next generation "lab-on-fiber" optrodes. *Nanoscale* **10,** 22673–22700 (2018).

176. Wang, N., Zeisberger, M., Huebner, U. & Schmidt, M. A. Boosting light collection efficiency of optical fibers using metallic nanostructures. *ACS Photonics* (2019).

177. Sreekanth, K. V. *et al.* Extreme sensitivity biosensing platform based on hyperbolic metamaterials. *Nature Materials* **15,** 621 (2016).

178. Kravets, V. *et al.* Singular phase nano-optics in plasmonic metamaterials for label-free single-molecule detection. *Nature Materials* **12,** 304 (2013).

179. Kravets, V., Schedin, F., Kabashin, A. & Grigorenko, A. Sensitivity of collective plasmon modes of gold nanoresonators to local environment. *Optics Letters* **35,** 956–958 (2010).

180. Thackray, B. D. *et al.* Narrow collective plasmon resonances in nanostructure arrays observed at normal light incidence for simplified sensing in asymmetric air and water environments. *ACS Photonics* **1,** 1116–1126 (2014).

181. Danilov, A. *et al.* Ultra-narrow surface lattice resonances in plasmonic metamaterial arrays for biosensing applications. *Biosensors and Bioelectronics* **104,** 102–112 (2018).

182. Raether, H. in *Surface plasmons on smooth and rough surfaces and on gratings* 4–39 (Springer, 1988).

183. Stewart, M. E. *et al.* Nanostructured plasmonic sensors. *Chemical Reviews* **108,** 494–521 (2008).

184. Li, M., Cushing, S. K. & Wu, N. Plasmon-enhanced optical sensors: a review. *Analyst* **140,** 386–406 (2015).

185. Choi, I. & Choi, Y. Plasmonic nanosensors: Review and prospect. *IEEE Journal of Selected Topics in Quantum Electronics* **18,** 1110–1121 (2012).

186. Lin, V. K. *et al.* Dual wavelength sensing based on interacting gold nanodisk trimers. *Nanotechnology* **21,** 305501 (2010).

187. Zhan, Y., Lei, D. Y., Li, X. & Maier, S. A. Plasmonic Fano resonances in nanohole quadrumers for ultra-sensitive refractive index sensing. *Nanoscale* **6,** 4705–4715 (2014).

188. Lassiter, J. B. *et al.* Fano resonances in plasmonic nanoclusters: geometrical and chemical tunability. *Nano Letters* **10,** 3184–3189 (2010).

189. Gross, H., Singer, W., Totzeck, M., Blechinger, F. & Achtner, B. *Handbook of optical systems* (Wiley-Vch Weinheim, 2005).

190. Optics, S. *Objectives Special Optics* Last accessed Mon. 4 Feb 2019. 2019. https://specialoptics.com/products/microscope-objectives/pre-engineered-high-na-objectives/objectives/.

191. Robens, C. *et al.* High numerical aperture (NA= 0.92) objective lens for imaging and addressing of cold atoms. *Optics Letters* **42,** 1043–1046 (2017).

192. Choi, Y. *et al.* Scanner-free and wide-field endoscopic imaging by using a single multimode optical fiber. *Physical Review Letters* **109,** 203901 (2012).

193. Wadsworth, W. J. *et al.* Very high numerical aperture fibers. *IEEE Photonics Technology Letters* **16,** 843–845 (2004).

194. Jain, C. *et al.* Silver metaphosphate glass wires inside silica fibers—a new approach for hybrid optical fibers. *Optics Express* **24,** 3258–3267 (2016).

195. Gilsdorf, R. W. & Palais, J. C. Single-mode fiber coupling efficiency with graded-index rod lenses. *Applied Optics* **33,** 3440–3445 (1994).

196. Yuan, S. & Riza, N. A. General formula for coupling-loss characterization of single-mode fiber collimators by use of gradient-index rod lenses. *Applied Optics* **38,** 3214–3222 (1999).

197. Gomez-Reino, C., Perez, M. V., Bao, C. & Flores-Arias, M. T. Design of GRIN optical components for coupling and interconnects. *Laser & Photonics Reviews* **2,** 203–215 (2008).

198. Chen, X. *et al.* Dual-polarity plasmonic metalens for visible light. *Nature Communications* **3,** 1198 (2012).

199. Decker, M. *et al.* High-efficiency dielectric Huygens' surfaces. *Advanced Optical Materials* **3,** 813–820 (2015).

200. Yu, N. & Capasso, F. Flat optics with designer metasurfaces. *Nature Materials* **13,** 139 (2014).

201. Paniagua-Dominguez, R. *et al.* A metalens with a near-unity numerical aperture. *Nano Letters* **18,** 2124–2132 (2018).

202. Byrnes, S. J., Lenef, A., Aieta, F. & Capasso, F. Designing large, high-efficiency, high-numerical-aperture, transmissive meta-lenses for visible light. *Optics Express* **24,** 5110–5124 (2016).

203. Khorasaninejad, M. *et al.* Polarization-insensitive metalenses at visible wavelengths. *Nano Letters* **16,** 7229–7234 (2016).

204. Saruwatari, M. & Nawata, K. Semiconductor laser to single-mode fiber coupler. *Applied Optics* **18,** 1847–1856 (1979).

205. Kataoka, K. Estimation of coupling efficiency of optical fiber by far-field method. *Optical Review* **17,** 476–480 (2010).

206. Cordero, E., Latka, I., Matthäus, C., Schie, I. W. & Popp, J. In-vivo Raman spectroscopy: from basics to applications. *Journal of Biomedical Optics* **23,** 071210 (2018).

207. Liang, H. *et al.* Ultrahigh numerical aperture metalens at visible wavelengths. *Nano Letters* **18,** 4460–4466 (2018).

208. Arbabi, A., Horie, Y., Ball, A. J., Bagheri, M. & Faraon, A. Subwavelength-thick lenses with high numerical apertures and large efficiency based on high-contrast transmitarrays. *Nature Communications* **6,** 7069 (2015).

209. Malkiel, I. *et al. Deep learning for the design of nano-photonic structures* in *Computational Photography (ICCP), 2018 IEEE International Conference on* (2018), 1–14.

210. Laboratories, S. N. *Sandia National Laboratories News Releases Mirage software automates design of optical metamaterials* Last accessed Mon. 15 April 2019. 2019. https://share-ng.sandia.gov/news/resources/news_releases/optical_metamaterials/.

211. Urban, A. S., Lutich, A. A., Stefani, F. D. & Feldmann, J. Laser printing single gold nanoparticles. *Nano Letters* **10,** 4794–4798 (2010).

212. Gargiulo, J., Cerrota, S., Cortés, E., Violi, I. L. & Stefani, F. D. Connecting metallic nanoparticles by optical printing. *Nano Letters* **16,** 1224–1229 (2016).

213. Do, J., Fedoruk, M., Jäckel, F. & Feldmann, J. Two-color laser printing of individual gold nanorods. *Nano Letters* **13,** 4164–4168 (2013).

214. Guffey, M. J., Miller, R. L., Gray, S. K. & Scherer, N. F. Plasmon-driven selective deposition of au bipyramidal nanoparticles. *Nano Letters* **11,** 4058–4066 (2011).

215. Richardson, D., Fini, J. & Nelson, L. E. Space-division multiplexing in optical fibres. *Nature Photonics* **7,** 354 (2013).

216. Li, G., Bai, N., Zhao, N. & Xia, C. Space-division multiplexing: the next frontier in optical communication. *Advances in Optics and Photonics* **6,** 413–487 (2014).

217. Kruk, S. *et al.* Transparent dielectric metasurfaces for spatial mode multiplexing. *Laser & Photonics Reviews* **12,** 1800031 (2018).

218. Kruk, S. & Kivshar, Y. Functional meta-optics and nanophotonics governed by Mie resonances. *ACS Photonics* **4,** 2638–2649 (2017).

219. Kruk, S. *et al.* Invited Article: Broadband highly efficient dielectric metadevices for polarization control. *APL Photonics* **1,** 030801 (2016).

220. Li, J. *et al.* Perspective: Biomedical sensing and imaging with optical fibers—Innovation through convergence of science disciplines. *APL Photonics* **3,** 100902 (2018).

Acknowledgements

Here, I would like to express my very greatest appreciation to my supervisor **Prof. Dr. Markus A. Schmidt** for his patient guidance, enthusiastic encouragement and constructive suggestions during the planning and development of my PhD work. Thanks for offering this precious opportunity of pursuing a PhD degree in Jena where the story of modern optics starts.

I would like to thank **Dr. Matthias Zeisberger** for his constant assistance in numerical simulations and theoretical analysis in this work. I benefit a lot from your inspiring instructions and enjoy intensive discussions on this work. I wish to thank various people for their contributions to this project; **Dr. Uwe Hüebner**, **Mr. Albrecht Graf**, **Dr. Henrik Schneidewind** and **Dr. Ondrej Stranik**, for their valuable technical support on sample fabrication, SEM images and experimental setup configurations; **Dr. Vincenzo Giannini**, for his helpful discussion on the optical properties of nanostructures.

My grateful thanks are also extended to **Dr. Alessandro Tuniz**, **Dr. Mario Chemnitz** and **Dr. Chhavi Jain** for their kindly help in experimental characterizations and data analysis. Special thanks to my colleges **Dr. Jiangbo Zhao**, **Tilman Lüder**, **Shiqi Jiang** and **Bumjoon Jang** who help me on correction of this thesis. I would also like to extend my thanks to the group members of hybrid fiber in Leibniz-IPHT: **Guangrui Li, Brenda Doherty, Malte Plidschun, Kay Schaarschmidt, Torsten Wieduwilt, Ramona Scheibinger, Mona Nissen, Dr. Xue Qi.**

At last, I wish to thank my family for their support and encouragement throughout my study. And thank you my dearest grandpa. We always love you.

Publications

Peer-reviewed journals

1. **Ning, Wang**, Matthias Zeisberger, Uwe Hübner, and Markus A. Schmidt. "Nanotrimer enhanced optical fiber tips implemented by electron beam lithography." Optical Materials Express 8, no. 8 (2018): 2246-2255.

   highlight in OSA 'Spotlight on Optics'

2. **Ning, Wang**, Matthias Zeisberger, Uwe Huebner, Vincenzo Giannini, and Markus A. Schmidt. "Symmetry-breaking induced magnetic Fano resonances in densely packed arrays of symmetric nanotrimers." Scientific Reports 9, no. 1 (2019): 2873.

3. **Ning, Wang**, Matthias Zeisberger, Uwe Huebner, and Markus A. Schmidt. "Boosting light collection efficiency of optical fibers using metallic nanostructures." ACS Photonics (2019).

Conference proceedings

1. **Ning, Wang**, Matthias Zeisberger, Uwe Hübner, and Markus Schmidt. "Nanostructured optical fiber tips implemented by e-beam lithography." Photonics West, SPIE. San Francisco, US. (2019)

2. **Ning, Wang**, Matthias Zeisberger, Uwe Hübner, and Markus Schmidt. "Boosting large-angle coupling efficiencies via nanostructures on optical fiber end faces implemented by e-beam lithography." Optics and Optoelectronics, SPIE. Prague, Czech Republic. (2019)

Poster contributions

1. **Ning, Wang** *et al*.. "Functional plasmonic fiber tip" International symposium 20 years nano-optics, Erlangen, Germany. (2017)

2. **Ning, Wang** *et al*.. "Simulation and realization of a fiber-based plasmonic trapping structure" Doctoral Conference on Optics DoKDoK, Oppurg, Germany. (2016)

   1^{st} of best poster award

Ehrenwörtliche Erklärung

Ich erkläre hiermit ehrenwörtlich, dass ich die vorliegende Arbeit selbständig, ohne unzulässige Hilfe Dritter und ohne Benutzung anderer als der angegebenen Hilfsmittel und Literatur angefertigt habe. Die aus anderen Quellen direkt oder indirekt übernommenen Daten und Konzepte sind unter Angabe der Quelle gekennzeichnet.

Bei der Auswahl und Auswertung folgenden Materials haben mir die nachstehend aufgeführten Personen in der jeweils beschriebenen Weise unentgeltlich geholfen:

1. Alle SEM-Bilder stammen von Dr. Uwe Hüebner und Dr. Henrik Schneidewind.

Weitere Personen waren an der inhaltlich-materiellen Erstellung der vorliegenden Arbeit nicht beteiligt. Insbesondere habe ich hierfür nicht die entgeltliche Hilfe von Vermittlungs- bzw. Beratungsdiensten (Promotionsberater oder andere Personen) in Anspruch genommen. Niemand hat von mir unmittelbar oder mittelbar geldwerte Leistungen für Arbeiten erhalten, die im Zusammenhang mit dem Inhalt der vorgelegten Dissertation stehen.

Die Arbeit wurde bisher weder im In- noch im Ausland in gleicher oder ähnlicher Form einer anderen Prüfungsbehörde vorgelegt.

Die geltende Promotionsordnung der Physikalisch-Astronomischen Fakultät ist mir bekannt.

Ich versichere ehrenwörtlich, dass ich nach bestem Wissen die reine Wahrheit gesagt und nichts verschwiegen habe.

_____ _____

Ort, Datum Unterschrift d. Verfassers